

**SYNTHESIS, CHARACTERIZATION AND APPLICATIONS OF RARE-
EARTH-ELEMENT-DOPED NANOPARTICLES**

A Dissertation

by

YUNYUN CHEN

Submitted to the Office of Graduate and Professional Studies of
Texas A&M University
in partial fulfillment of the requirements for the degree of

DOCTOR OF PHILOSOPHY

Chair of Committee,	Hong Liang
Committee Members,	Terry Creasy
	Philip Hemmer
	Alexei Sokolov
Head of Department,	Ibrahim Karaman

December 2017

Major Subject: Materials Science and Engineering

Copyright 2017 Yunyun Chen

ABSTRACT

With the excellent optical performance, the rare-earth-element-doped (RE-doped) nanomaterials have been widely applied in biological system and optical engineering. The understanding about effects of rare earth elements on optical properties needs to be further achieved. In the present research, a new approach has been developed to control the morphology and modify the optical performance of engineered RE-doped nanomaterials.

Experimental approaches contain synthesis, characterization, and optical and tomographic imaging investigation of nanomaterials: morphology-controlled yttrium oxide doped with erbium and ytterbium ($\text{Y}_2\text{O}_3:\text{Er}^{3+}, \text{Yb}^{3+}$), hydrogen-treated aluminum yttrium oxide ($\text{Y}_3\text{Al}_5\text{O}_{12}$ or YAG) doped with cerium ($\text{YAG}:\text{Ce}^{3+}$), and oleic acid coated sodium yttrium fluoride ($\text{OA-NaYF}_4:\text{Er}^{3+}, \text{Yb}^{3+}$).

The morphology of $\text{Y}_2\text{O}_3:\text{Er}^{3+}, \text{Yb}^{3+}$ were controlled by introducing metal ions during facile hydrothermal synthesis. It was found that the negatively charged aluminum complex ions enabled the evolution of nanotubes through rolling from nanosheets. The positively charged calcium complex ions prohibited the rolling of nanosheets. For hydrogen-treated $\text{YAG}:\text{Ce}^{3+}$, the hydrogenation has been firstly used to induce the defects into the host lattice of YAG, which leads to a red-shift in the emission spectrum of $\text{YAG}:\text{Ce}$. This red-shift can make an improvement in warm white LED (light emitting diode). For OA-coated $\text{NaYF}_4:\text{Er}^{3+}, \text{Yb}^{3+}$, they were firstly applied in lubricant. As

mineral oil is a type of nonpolar oil, OA-coated $\text{NaYF}_4:\text{Er}^{3+}, \text{Yb}^{3+}$ NPs would be a potential excellent additives.

In fundamental investigation, three approaches and mechanisms in modifying optical performance of RE-doped nanoparticles (NPs) were studied. They are using alternative host lattice, alternative dopants and introducing defects.

Optical and tomographic imaging was used to study the effects of NPs on bio-imaging, white LED and lubricating grease. As RE-doped NPs were widely used, once engineered NPs are translocated to the food chains, they could accumulate in organisms and even cause toxicity and biomagnification. In order to investigate the effects of engineered NPs on environment, synchrotron dual-energy X-ray micro-tomography was used to study the uptake pathway, accumulation, distribution and concentration mapping of the engineered NPs in an essential component of ecosystems, the plants.

DEDICATION

To my beloved family, with whom my life is the most beautiful one!

To my advisor for making me persistent

To all those I have met along the way for making me strong

ACKNOWLEDGEMENTS

Undertaking the Ph.D. study and research has been a meaningful experience for me. Thanks to the support and assistance from many people, I can face and overcome the challenge in this period. First of all, I would like to gratefully thank my advisor, Dr. Hong Liang, for her support, guidance, and assistance in my research and most importantly, the advice in my daily life. She helped me to think independently and creatively.

I would also like to thank the support from my committee members, Dr. Terry Creasy, Dr. Dilworth Parkinson, Dr. Philip Hemmer, and Dr. Alexei Sokolov for their valuable advice and comments on this research.

I would also like to thank the assistance and guidance from Dr. Dilworth Parkinson and Dr. Carlos Sanchez on the Beamline experiments performed at Lawrence Berkeley National Laboratories (LBNL). Thanks for the one-year ALS Doctoral Fellowships, many of my research works were performed in this period.

I would like to thank the assistance and guidance from Mr. Masfer Alkahtani, Mr. Fahad Ghannam, Dr. Philip Hemmer on making and using optical microscopy. I'd like to thank Dr. Andreas Holzenburg and Dr. Li Liu for the valuable comments and advice throughout the course study related with research.

I am also grateful to the support from the Microscopy Image Center (MIC), and the Materials Studio software from Chemical Department. I would like to give a special thanks to Dr. Alex Fang for the teaching assistant position. I wish to acknowledge Jet-Lube for

providing the reference compound. Partial support by the Texas A&M strategic seed grant program and the Turbomachine Research Laboratory is acknowledged. Part of the open access publishing fee for this manuscript has been provided by the Texas A&M University Online Access to Knowledge Fund (OAKFund), supported by the University Libraries and the Office of the Vice President for Research.

I want to thank all the members in Surface Science Group as well for their assistance and suggestions in my research. Assistance provided by Dr. Subrata Kundu, Dr. Xingliang He, Dr. Hyunho Chio, and Mr. Alexander Sinyukov in my graduate research are also deeply appreciated.

Thanks for my friends and the department faculty and staff as well for making my time at Texas A&M University a great experience.

Finally, I really want to thank my parents for all of their love, supports, and endless patience.

CONTRIBUTORS AND FUNDING SOURCES

Contributors

This work was supervised by a dissertation committee consisting of Professor Hong Liang of the Department of Materials Science and Engineering, Professor Terry Creasy of the Department of Materials Science and Engineering, Professor Philip Hemmer of the Department of Electrical & Computer Engineering, Professor Alexei Sokolov of the Department of Physics & Astronomy, and Dr. Dilworth Parkinson of Advanced Light Source, Lawrence Berkeley National Lab.

Part 2, student/collaborator contributions

The feeding of insects and culture of plants for Chapter 5 was provided by Dr. Jorge M González. The confocal laser scanning microscope setup in Chapter 3 were conducted by Mr. Masfer Alkahtani.

All other work conducted for the dissertation was completed by the student independently.

Funding Sources

Graduate study was supported by an ALS doctoral fellowship from Advanced Light Source.

NOMENCLATURE

NP	Nanoparticle
DC	Down-conversion
DS	Down-shift
UCNPs	Upconversion nanoparticles
NIR	Near infrared
UV	Ultra-violet
EDS	Energy-dispersive X-ray spectroscopy
TEM	Transmission electron microscope/microscopy
XRD	X-ray diffraction
LED	Light emitting diode
WLED	White light emitting diode
RE	Rare earth
Ln	Lanthanide
Ac	Actinide
KES	K-edge subtraction technique
μ -XCT	Micro X-ray computed tomography

TABLE OF CONTENTS

	Page
ABSTRACT	ii
DEDICATION	iv
ACKNOWLEDGEMENTS	v
CONTRIBUTORS AND FUNDING SOURCES.....	vii
NOMENCLATURE.....	viii
TABLE OF CONTENTS	ix
LIST OF FIGURES.....	xii
LIST OF TABLES	xviii
CHAPTER I INTRODUCTION	1
1.1. Rare earth elements	1
1.1.1. Down-conversion and down-shifting photoluminescence	2
1.1.2. Up-conversion luminescence	3
1.1.3. Principal luminescence processes of RE-doped NPs	7
1.1.3.1. Mechanisms of down-shifting process.....	9
1.1.3.2. Mechanisms of down-conversion process.....	10
1.1.3.3. Mechanisms of up-conversion process	12
1.2. Imaging techniques	13
1.2.1. Optical confocal microscopy.....	15
1.2.2. Tomography	17
1.3. Effects of lanthanide-doped NPs.....	19
1.3.1. Environment	19
1.3.2. Optical device.....	20
1.3.3. Nanoparticles as additives in lubricants	23
1.4. Summary	24
CHAPTER II MOTIVATION AND OBJECTIVES	25
2.1. Objectives.....	25
2.1.1. Development of RE-doped NPs	25
2.1.2. Control of optical performance through modification of RE-doped NPs	26
2.1.3. Identification of biological and engineering applications	26

2.2.	Dissertation structures	27
CHAPTER III MATERIALS AND METHODS		28
3.1.	Materials	28
3.2.	Synthesis of nanomaterials	29
3.2.1.	Preparation of $Y_2O_3:Er^{3+}, Yb^{3+}$	29
3.2.2.	YAG:Ce ³⁺ and YAG:Er ³⁺ , Yb ³⁺ Nanoparticles	31
3.2.3.	OA-coated NaYF ₄ nanoparticles	32
3.3.	Methods of characterization	33
3.3.1.	Crystal structure and morphology	33
3.3.2.	Confocal microscopy experiments	34
3.3.3.	Synchrotron X-ray micro-tomography experiments	35
3.4.	Characteristics and properties of nanoparticles	36
3.4.1.	$Y_2O_3:Er^{3+}, Yb^{3+}$ nanoparticles	36
3.4.2.	YAG:Ce ³⁺ nanoparticles	42
3.4.3.	NaYF ₄ :Er ³⁺ , Yb ³⁺ nanoparticles	46
3.5.	Summary	48
CHAPTER IV MODIFICATION OF OPTICAL PERFORMANCE THROUGH SYNTHESIS		50
4.1.	Alternative dopants	50
4.2.	Alternative host lattices	56
4.3.	Introducing defects	59
4.3.1.	Upconversion performance of $Y_2O_3:Er, Yb$ by introducing metal ions... ..	59
4.3.2.	Down-shifting performance of YAG:Ce ³⁺ by hydrogenation	61
4.4.	Summary	65
CHAPTER V <i>IN SITU</i> DETECTING NANOPARTICLES IN BIOLOGICAL SYSTEM		67
5.1.	Probing of yttria NPs in fire ants (<i>Solenopsis xyloni</i>)	67
5.1.1.	Two-dimensional confocal optical imaging	68
5.1.2.	Visual Light Tomography	70
5.1.3.	Synchrotron Micro-tomography with Dual-energy K-edge subtraction	72
5.1.4.	Comparison of three imaging techniques	74
5.2.	Mealworms (<i>Tenebrio Molitor</i>)	76
5.3.	Probing of yttria NPs in cabbage	82
5.3.1.	Cabbage culture and exposure to nanoparticles	84
5.3.2.	Identifying nanoparticles in cabbage	85
5.3.3.	Three-dimensional distribution of nanoparticles in cabbage	90
5.3.4.	Quantification of Nanoparticles	93
5.3.5.	Limitations in KES	98

5.4. Summary	98
CHAPTER VI PROBING OF NANOPARTICLES IN ENGINEERING SYSTEM	100
6.1. Grease.....	100
6.1.1. Special fixture designing.....	101
6.1.2. Identification of thickeners and additives	102
6.1.3. Localization and distribution of particle additives	106
6.1.4. Limitations of luminescence imaging in dispersion study	108
6.2. White light emitting diode application of YAG:Ce	108
6.3. Summary	111
CHAPTER VII CONCLUSIONS AND FUTURE RECOMMENDATIONS	113
7.1. Conclusions	113
7.2. Future recommendations	114
REFERENCES	116

LIST OF FIGURES

	Page
Figure 1. The rare earth elements (Green) and lanthanides (red) in periodic table....	2
Figure 2. The energy level of trivalent Ln ions. Reprinted with permission from reference [27].....	5
Figure 3. Schematics of energy conversion process of RE doped materials.....	7
Figure 4. The typical energy transfer of DS process in Ln ions.....	10
Figure 5. The typical energy transfer of DC process in Ln ions. (Purple: absorption; Blue: energy transfer; Red: emission; Gray: cross relaxation).....	11
Figure 6. The typical energy transfer of UC process in Ln ions. (Solid red: absorption; Dash red: non-resonant ground state absorption; Blue: energy transfer; Purple: emission; Gray: cross relaxation)	13
Figure 7. Schematic of a typical confocal spectrometer.	15
Figure 8. Aberration of using optical lens.	16
Figure 9. Improvement in emission spectra by using broad band spectrometer	16
Figure 10. Schematic diagram showing the condition of the X-ray straddling K-edge.....	18
Figure 11. Graph of mass attenuation coefficient for carbo and yttrium. The value is derived from National Institute of Standards and Technology database (NIST X-ray Attenuation Databases).	19
Figure 12. Schematic diagram of biomagnificaiton in a food chain.	20
Figure 13. Schematic structure of white LED.....	21
Figure 14. CIE1931 x and y chromaticity coordinate diagram.	22
Figure 15. Components and their occupation of grease.	24
Figure 16. Research flow chart.	27
Figure 17. Schematic diagram of the non-stirred pressure vessel.....	30

Figure 18. Schematic diagram of thermalysis system.....	33
Figure 19. Schematic drawing of a confocal laser scanning microscope setup consisting of a 4f imaging system, a photon counter, and a spectrometer.....	34
Figure 20. Schematic diagram of beamline 8.3.2 constructing 3D visualization.....	36
Figure 21. The TEM images of samples B1 and B2.	38
Figure 22. The TEM images of samples (a) B3 and (b) A3. (c) High resolution TEM image of A3. (d) The XRD pattern of sample A3.....	39
Figure 23. The TEM images of samples (a) B4 and (b) A4. (c) High resolution TEM image of A4. (d) The XRD pattern of sample A4.....	40
Figure 24. Schematic illustration for the formation of alternative shapes in samples B1-B4.....	41
Figure 25. The rolling-up process for the formation of nanotubes from nanosheets.....	42
Figure 26. The color change of YAG:6%Ce ³⁺ before and after hydrogenation.....	44
Figure 27. XRD patterns of as-synthesized YAG:Ce ³⁺	44
Figure 28. TEM images of YAG:6%Ce ³⁺ with hydrogenation (a) low magnification, (b) high magnification.	45
Figure 29. EDS spectrum of YAG:6%Ce.....	45
Figure 30. Dispersion of NPs in nonpolar organic solvents. From left to right, the three samples are mineral oil, 1wt% NaYF ₄ :Er ³⁺ ,Yb ³⁺ in mineral oil, and 1wt% NaYF ₄ :Er ³⁺ ,Yb ³⁺ in hexane.....	46
Figure 31. TEM images of as-synthesized NaYF ₄ NPs with thermolysis method.....	48
Figure 32. The process of generating hollow structure in NPs.	48
Figure 33. The XRD pattern of YAG:Ce and YAG:Er,Yb NPs.....	51
Figure 34. Emission spectra of YAG:Er,Yb NPs excited by 473 nm and 980 nm.....	52
Figure 35. Energy diagram of Ce ³⁺ in YAG:Ce.....	53

Figure 36. Energy level diagrams of Er^{3+} and Yb^{3+} ions, and proposed upconversion mechanisms ^{27,151,152}	54
Figure 37. Emission spectrum of $\text{Y}_2\text{O}_3:\text{Er},\text{Yb}$ in order to observe the stark sub-levels.....	55
Figure 38. Emission spectra of $\text{Y}_2\text{O}_3:\text{Er}^{3+},\text{Yb}^{3+}$ (upper), and $\text{YAG}:\text{Er}^{3+},\text{Yb}^{3+}$ (lower).	57
Figure 39. The crystal structures and the non-centrosymmetric doping sites of (a) Y_2O_3 and (b) YAG for RE ions. The crystallographic information file was obtained from Inorganic Crystal Structure Database.	59
Figure 40. Upconversion emission spectra of $\text{Y}_2\text{O}_3:\text{Er},\text{Yb}$ under the excitation of a 980nm diode laser.....	60
Figure 41. (a) The crystal model of YAG with interstitial H atom. The band structure and density of states of (b) YAG and (c) YAG with interstitial atom.....	62
Figure 42. Photoluminescence spectra of (a) $\text{YAG}:\text{2\%Ce}^{3+}$ and (b) $\text{YAG}:\text{6\%Ce}^{3+}$ with and without hydrogen treatment.....	63
Figure 43. Gaussian curve fittings for emission spectra of (a) $\text{YAG}:\text{2\%Ce}$, (b) $\text{YAG}:\text{2\%Ce}+\text{H}_2$, (c) $\text{YAG}:\text{2\%Ce}+\text{48hH}_2$, (d) $\text{YAG}:\text{6\%Ce}$, (e) $\text{YAG}:\text{6\%Ce}+\text{H}_2$, and (f) $\text{YAG}:\text{6\%Ce}+\text{H}_2$ samples.....	64
Figure 44. Nephelauxetic effect on Ce^{3+}	65
Figure 45. Three potential methods to modify the optical performance of RE-doped NPs and their mechanisms.....	66
Figure 46. X-Y scanning of ant by photon counter.....	69
Figure 47. Emission spectra of fluorescence spots in ant	70
Figure 48. Centered projective image of ant sample excited by 532 nm.	71
Figure 49. 3D visualization of ant excited by 532 nm laser and (b) 980 nm NIR laser.....	72
Figure 50. The slice obtained by scanning at (a) 17.3 keV and (b) 16.7 keV. (c) The subtracted slice to identify and localize the $\text{Y}_2\text{O}_3:\text{Er}^{3+},\text{Yb}^{3+}$ NPs.....	73
Figure 51. Three dimensional X-ray imaging of UCNPs inside fire ant. The box size of (c) is 1.15 x 1.09 x 3.08 mm	74

Figure 52. The translocation of NPs within mealworms with extended feeding time. 3D Visualization of samples, using the (above/below/difference) data. The most concentrated distribution of NPs inside the mealworms is labeled with red circles. Regions of apparently high NP concentration that are not circled are on the outside surface of the mealworm, spread by their grooming actions.	79
Figure 53. The localization of NPs inside the digestive system of the mealworms. (a), (e), and (i) show 3D visualizations and indicate the locations of three slices which are displayed to the right of those panels. (a) head segment of 1 h fed mealworm sample, (e) thorax segment of 12 h fed mealworm sample, (i) abdomen segment of 24 h fed mealworm sample. The dark (nearly black) regions within the colored circles are identified as NPs; other dark areas result from the shift of biological tissue between the two X-ray scans. Colored circles correspond to: Black: Buccal cavity; Red: Pharynx; Purple: Oesophagus; Yellow: Crop; Green: on Surface; Blue: Midgut; White: Encapsulated NPs inside Coelom; Orange: Anterior Intestine.....	80
Figure 54. The distribution of NPs within mealworms organs. The accumulated NPs inside the (a) 1 h, (b) 12 h and (c) 24 h fed mealworm.....	81
Figure 55. The surface views of accumulated NPs at different parts in mealworms. Each color represents a different organs corresponding to Figure 53.....	81
Figure 56. Hydroponic system for cabbage exposure to yttria NPs.....	85
Figure 57. Transverse reconstructed slices at the junction between primary root and lateral root scanned at (a) 17.2 keV, (b) 16.5 keV, and (c) subtracted slice. (d–e) The slices for leave section	86
Figure 58. The process of image segmentation. (a). Reconstructed image obtained 17.2 keV. (b). Reconstructed image at 16.5 keV. (c). The subtracted slice from (a) and (b). (d). Subtracted slice with an image registration function. (e). Colors label the intensity of pixel value of (d). (f–i) Image segmentation based on the threshold of (a, b). Detailed data of images (f–i) is listed in Table 9.....	88
Figure 59. Histograms of image pixel value (absorption coefficient) for root.	89
Figure 60. The 3D visualization for a wide view of root built by (a) 17.2 keV transverse reconstructed slice datasets and (b) 16.5 keV datasets. (c) Distribution of yttria NPs (red) in root. The grey visualization was	

built by 17.2 keV; the red one was built by the subtracted datasets. The bounding box size is $6.77 \times 5.10 \times 19.40$ mm	91
Figure 61. The micro-scale of root segmentation localized at yttria NPs aggregated regions. (a) The selected yellow region in 17.2 keV visualization. (b) The top transverse slice of yellow frame region. (c) Magnified view of yellow frame. The vascular tissue (VT) and ground tissue (GT) are shown in (b). The red regions in (c) show the distribution of yttria NPs. The yellow frame size is $0.58 \times 0.58 \times 0.13$ mm	93
Figure 62. (a) The full volume visualization of plant root. (b) Concentration map of yttria NPs in root (on the voxel level)	96
Figure 63. The 3D visualization of shoot section for cabbage built by (a) 17.2 keV transverse reconstructed slice datasets and (b) 16.5 keV datasets. (c) Distribution of yttria NPs in shoot. The bounding box size is $7.65 \times 7.29 \times 19.40$ mm	97
Figure 64. The rotating holder for shearing grease. (a) Dimetric view and (b) Section view of rotating holder.	102
Figure 65. Graph of mass attenuation coefficient for carbon, calcium and iron. The value is derived from National Institute of Standards and Technology database (NIST X-ray Attenuation Databases).	103
Figure 66. (a) The pixel value distribution of reconstructed datasets. The 3D visualization of grease without Fe_3O_4 additives (b) and with Fe_3O_4 additives (c). The height of both 3D models is 3.892 mm.	104
Figure 67. The 2D transverse slices of greases (a) without and (b) with Fe_3O_4 additives. The 3D visualization of samples (c) without and (d) with Fe_3O_4 additives. The slice with red frame in (c-d) is transverse 2D slice. The transverse slice size of (a-d) is 8.4000×8.400 mm.	105
Figure 68. (a) The distribution of Fe_3O_4 additive shown in red regions. (b) The enlarge view of single calcium complex thickener (grey) and Fe_3O_4 additives (red). The box size is $98.89 \times 98.89 \times 98.89$ μm	107
Figure 69. Distribution Map and emission spectra of coated (a) YAG:6%Ce+H ₂ and (b) YAG:6%Ce.	110
Figure 70. CIE color coordinates of YAG:Ce powder coated on the blue chips with different ratio of powder to epoxy resin. The blue markers represent the sample YAG:6%Ce and black markers are for	

YAG:6%Ce+H₂. Diamond: pure powder; Circle and triangle: coated powder on blues chips corresponding to Figure 69. 110

Figure 71. (a) White luminescent spectra of YAG:6%Ce+H₂ powder coated on blue chip with different operating voltages (circle marker in Figure 69). (b) CIE coordinates of WLED at different operating voltages. 111

LIST OF TABLES

	Page
Table 1. The summary of nanoparticles, synthesis and schematic of heterostructures	6
Table 2. Principle emission transitions of Ln-doped materis.....	8
Table 3. Comparison of current commonly used imaging techniques.....	14
Table 4. The symbols of the samples before and after calcining.	31
Table 5. Comparison the energy transition of $^4S_{3/2}$ sublevels for $Y_2O_3:Er, Yb$ at room temperature.	55
Table 6. Table of two Gaussian curve peak centers and their difference.....	64
Table 7. The advantages and disadvantages of three techniques.	75
Table 8. The uptake of different ENPs by plants	82
Table 9. The characterizations for the sub-Figure 58.....	89

CHAPTER I

INTRODUCTION*

This chapter provides basic information about the background related to this research. This research is focusing on the lanthanide elements doped nanomaterials and their application in biological and engineering system. This chapter includes three sections: the first section gives an introduction of rare earth (RE) elements; the second section describes the imaging techniques which will be employed in present research; the last section shows the applications of RE-doped NPs in biological and engineering systems.

1.1. Rare earth elements

The rare earth elements are fifteen lanthanide elements with the chemically similar scandium and yttrium elements, shown in Figure 1.¹ The lanthanide (Ln) electron configuration is $[\text{Xe}]4f^x5d^{0-1}6s^2$. The Ln ions will lose the electrons on 6s and 5d shell. They have distinct unfilled 4f electron configuration and be effectively screened by the outer electron shells 5f and 5d. Rare-earth (RE) ions obtain unique optical behavior once doped into host materials.² The photoluminescence performance of RE-doped NPs can be considered as down-conversion, down-shifting and upconversion.^{3,4}

*Part of this chapter reproduced with permission from “Applications of quantum dots with upconverting luminescence in bioimaging” by Yunyun Chen, et al., *J. Photochem. Photobiol. Biology.*, **2014**, 135, 23-32, <https://doi.org/10.1016/j.jphotobiol.2014.04.003> (Copyright © 2014 Elsevier B.V.).

1																	2
H																	He
3	4											5	6	7	8	9	10
Li	Be											B	C	N	O	F	Ne
11	12											13	14	15	16	17	18
Na	Mg											Al	Si	P	S	Cl	Ar
19	20	21	22	23	24	25	26	27	28	29	30	31	32	33	34	35	36
K	Ca	Sc	Ti	V	Cr	Mn	Fe	Co	Ni	Cu	Zn	Ga	Ge	As	Se	Br	Kr
37	38	39	40	41	42	43	44	45	46	47	48	49	50	51	52	53	54
Rb	Sr	Y	Zr	Nb	Mo	Tc	Ru	Rh	Pd	Ag	Cd	In	Sn	Sb	Te	I	Xe
55	56	Ln	72	73	74	75	76	77	78	79	80	81	82	83	84	85	86
Cs	Ba		Hf	Ta	W	Re	Os	Ir	Pt	Au	Hg	Tl	Pb	Bi	Po	At	Rn
87	88	Ac	104	105	106	107	108	109	110	111	112	113	114	115	116	117	118
Fr	Ra		Rf	Db	Sg	Bh	Hs	Mt	Ds	Rg	Cn	Uut	Fl	Uup	Lv	Uus	Uuo
Ln	57	58	59	60	61	62	63	64	65	66	67	68	69	70	71		
	La	Ce	Pr	Nd	Pm	Sm	Eu	Gd	Tb	Dy	Ho	Er	Tm	Yb	Lu		
Ac	89	90	91	92	93	94	95	96	97	98	99	100	101	102	103		
	Ac	Th	Pa	U	Np	Pu	Am	Cm	Bk	Cf	Es	Fm	Md	No	Lr		

Figure 1. The rare earth elements (Green) and lanthanides (red) in periodic table

1.1.1. Down-conversion and down-shifting photoluminescence

Both down-conversion (DC) and down-shifting (DS) luminescence refer to a process of Stokes shift, which absorb high photon energy and emit the low photon energy. The DC luminescence is a process that involves absorption of one high energy photon followed by emitting two or more low energy photons, which is also known as quantum cutting.^{5,6} Quantum cutting was firstly reported by Piper *et al.*⁷ and Sommerdijk *et al.*⁸ for Pr³⁺ doped materials. The DS luminescence is a process of absorption one high energy photon process continued by converting into one lower energy photon.⁹ The DS is similar to DC, but the quantum efficiency is much lower than DC. The DC and DS luminescence of RE-doped materials has been widely applied in

light cell imaging as contrast agents, emitting diode (LED) and solar cell.¹⁰⁻¹⁵ Most common used exogenous contrast agents, such as fluorescence proteins, organic dyes and quantum dots (QDs), have down-conversion luminescence.¹⁶ The 4f-5d transitions absorption are of Ln³⁺ ions, such as Ce³⁺ and Eu³⁺ are the most commonly used for down-conversion luminescence. These agents are generally excited by ultra-violet (UV) light, which has several limitations. First, it is harmful to the cells and tissues under a longtime exposure under UV laser. Second, some biological structure, like protein, can be excited by UV wavelength, which will generate autofluorescence and results in the background noise for the bioimaging of the agents. Third, the penetration depth of UV laser is not deep in the tissue, which is only around 1 mm.¹⁷ The agents, deep in the tissue or body, may even not be excited with UV. In addition, the blinking phenomenon of a single QD crystal will give rise to losing the signal of QDs when using the single particle tracking and labeling in living cells.¹⁸ To solve these pitfalls, making use of the (upconversion luminescence) UCL is a potential solution, which will be discussed in section 1.1.2. The most commonly used rare earth elements for white LED are cerium, europium, or europium co-doped with other RE elements.¹⁹⁻²²

1.1.2. Up-conversion luminescence

Upconversion luminescence (UCL) is a phenomenon of anti-Stokes shift. It is a non-linear optical process in which the sequential absorption of two or more low-energy near infrared (NIR) photons leads to emit high-energy in visible wavelength.

The upconversion nanoparticles (UCNPs), particularly lanthanide (Ln)-doped nanocrystals, have been widely reported by employing the UCL phenomenon due to the

specific electron configuration of Ln elements.²³⁻²⁶ The UCL is based on the electron dipole 4f-4f electron transition of Ln ions, which is forbidden according to the Laporte's selection rule. Figure 2 shows the energy level of trivalent Ln ions.²⁷ This Dieke diagram plays a critical role in investigating the absorption spectra of 4f-4f and energy transfer among Ln ions. It shows the Ln ions can be excited by a certain wavelength in NIR wavelength, like $^4I_{11/2}$ energy state of Er^{3+} . The absorption energy is around 10000 cm^{-1} (1000 nm). However, if the Ln ions occupy the noncentrosymmetric sites, the magnetic dipole and electric quadrupole will allow the 4f-4f transition. Furthermore, with the protection of 5f and 5d electron shells, the crystal field and the external applied electric or magnetic field will not affect the 4f-4f transition, and the spectra of 4f-4f transition will be sharp.

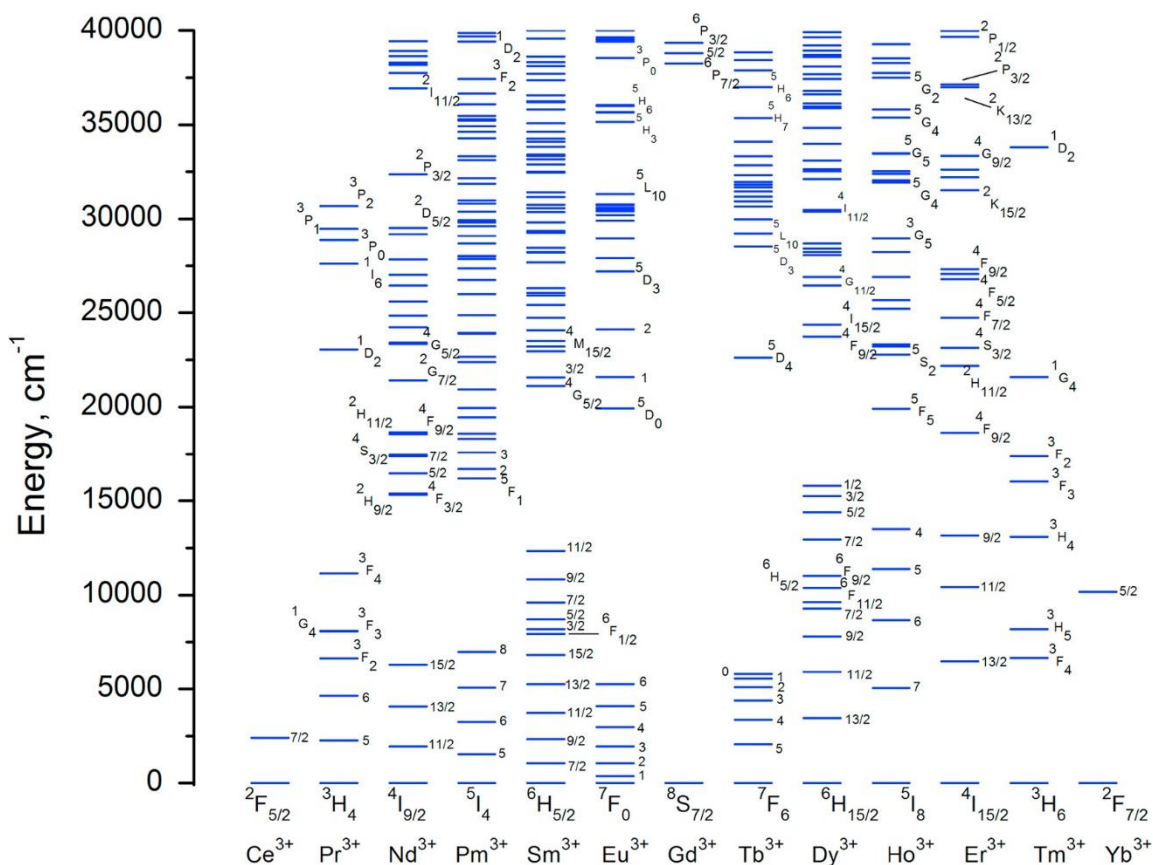
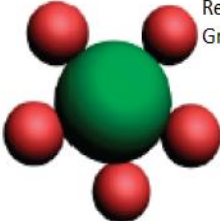
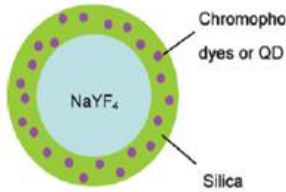
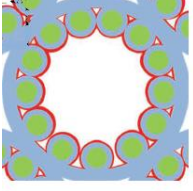


Figure 2. The energy level of trivalent Ln ions. Reprinted with permission from reference [27].

Recently, the upconversion nanoparticles have attracted great attention in biological imaging, labeling, and therapy. With the NIR excitation, the UCNPs can avoid the long exposure under UV light and be beneficial to bio-imaging with zero-autofluorescence and absence of blinking. Furthermore, based on the NIR window in biological tissue, the wavelength from 650 nm to 1350 nm has the maximum penetration depth in the tissue.²⁸ Qian Liu *et al.* achieved a high contrast UCL imaging with a 2 cm penetration depth of a black body mouse *in vivo*.²⁹ In order to achieve UCL performance, the QDs are modified with lanthanide elements, such as making hetero-structures of QDs and UCNPs or doped QDs with lanthanide elements. The hetero-structures are the

combination of QDs and UCNPs in a system, which use QDs as energy acceptors and UCNPs as energy donors. The fluorescence emission band of UCNPs overlaps the absorption band of QDs; resulting UCNPs transfer their emission energy to QDs via a fluorescence resonance energy transfer (FRET) or energy re-absorption. The way to transfer energy from UCNPs to QDs greatly depends on the distance between UCNPs and QDs. If the distance is less than 100 Å, the preferred procedure is FRET, which transfers energy in the form of phonons or lattice vibrations. Otherwise, the alternative is re-absorption, which transfers energy as photons. The heterostructure can be core-shell structured^{30,31} or the QDs *in situ* growth on the UCNPs³², as Table 1 shows.

Table 1. The summary of nanoparticles, synthesis and schematic of heterostructures

Nanoparticles	Synthesis	Schematic of Heterostructure	Ref
CdSe/NaYF ₄ :Yb,Er	NaYF ₄ :Yb,Er : Thermal decomposition Heterostructure: Grown on UCNPs	 Red: QDs Green: UCNPs	32
QDs/SiO ₂ /NaYF ₄ :Yb,Er/Tm	NaYF ₄ :Yb,Er/Tm: Thermal decomposition Heterostructure: Microemulsion	 Chromophores: dyes or QD NaYF ₄ Silica	30
CdSe/SiO ₂ /β-NaYF ₄ :Yb,Er	NaYF ₄ :Yb,Er: Thermal decomposition Heterostructure: Sensitization	 UC Nanophosphors TiO ₂ CdSe	31

1.1.3. Principal luminescence processes of RE-doped NPs

The three typical luminescence processes for RE doped materials includes: down-shifting (DS), down-conversion (DC) and upconversion (UC), shown in Figure 3.³³ Table 2 shows the photoluminescence performance of lanthanide ions in energy state transition.

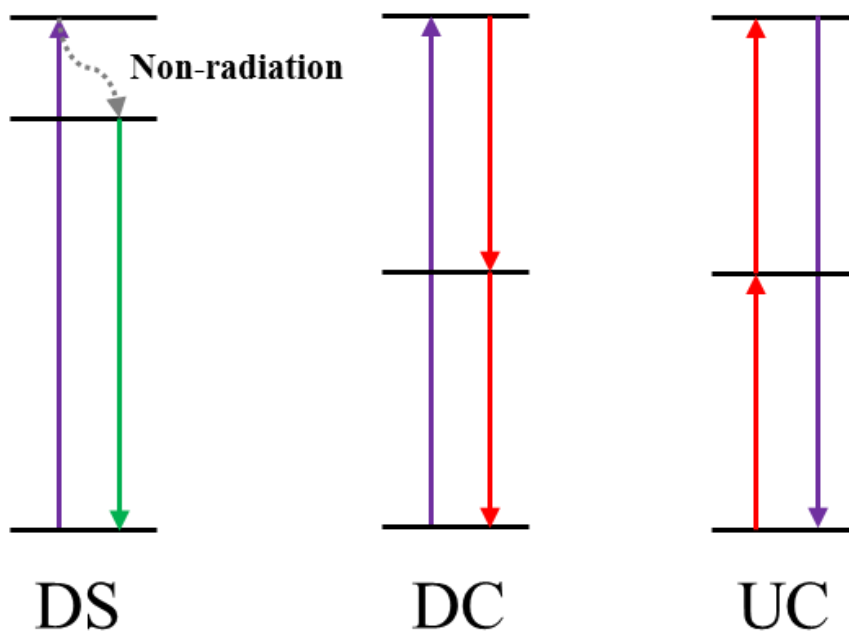


Figure 3. Schematics of energy conversion process of RE doped materials.

Table 2. Principle emission transitions of Ln-doped materis

Ln	Ground state	Excited state	Final state	Emission wavelength	Remarks	Ref.	
Ce	$^2F_{5/2}$	$^2B_{1g}$	$^2F_{5/2}$	540 nm	QS	34,35	
		$^2A_{1g}$	$^2F_{5/2}$	540 nm	QS		
Pr	3H_4	3P_0	3H_4	490 nm	DC&UC	36,37	
			3H_5	528 nm	DC&UC		
			3H_6	611 nm	DC&UC		
			3F_2	643 nm	DC&UC		
			3P_1	3H_4	490 nm		DC
			3H_6	611 nm	DC		
			1D_2	1G_4	1.30-1.67 μm		QS
			1D_2	1G_4	1.30-1.67 μm		QS
Nd	$^4I_{9/2}$	$^4F_{3/2}$	$^4I_{9/2}$	905 nm	QS&UC	38,39	
			$^4I_{11/2}$	1067 nm	QS&UC		
			$^4I_{13/2}$	1340 nm	QS&UC		
			$^4F_{5/2}$	$^4I_{9/2}$	797 nm		QS
			$^4F_{7/2}$	$^4I_{9/2}$	745 nm		QS
Sm	$^6H_{5/2}$	$^4G_{5/2}$	$^6H_{5/2}$	568 nm	QS	40,41	
			$^6H_{7/2}$	601 nm	QS		
			$^6H_{9/2}$	648 nm	QS		
			$^6H_{11/2}$	708 nm	QS		
Eu	7F_0	5D_0	7F_0	578 nm	QS&UC	42,43	
			7F_1	592 nm	QS&UC		
			7F_2	614 nm	QS&UC		
			7F_3	653 nm	QS&UC		
			7F_4	702 nm	QS&UC		
Tb	7F_6	5D_4	7F_6	491 nm	QS&DC&UC	44,45	
			7F_5	549 nm	QS&DC&UC		
			7F_4	590 nm	QS&DC&UC		
			7F_3	622 nm	QS&DC&UC		
Dy	$^6H_{15/2}$	$^4F_{9/2}$	$^6H_{15/2}$	487 nm	DS&DC	46,47	
			$^6H_{13/2}$	575 nm	DS&DC		
			$^6H_{11/2}$	667 nm	DS&DC		

Table 2. Continued

Ln	Ground state	Excited state	Final state	Emission wavelength	Remarks	Ref.
			${}^6\text{H}_{9/2}+{}^6\text{F}_{11/2}$	759 nm	DS&DC	
Ho	${}^5\text{I}_8$	${}^5\text{S}_2+{}^5\text{F}_4$	${}^5\text{I}_8$	547 nm	UC&DC	48-51
			${}^5\text{I}_6$	1015 nm	UC&DC	
		${}^5\text{F}_5$	${}^5\text{I}_8$	660 nm	UC&DC	
			${}^5\text{I}_7$	750 nm	UC&DC	
		${}^5\text{I}_6$	${}^5\text{I}_8$	1180 nm	DC	
Er	${}^4\text{I}_{15/2}$	${}^2\text{H}_{9/2}$	${}^4\text{I}_{15/2}$	410 nm	UC&DC	52,53
		${}^2\text{H}_{11/2}$	${}^4\text{I}_{15/2}$	520 nm	UC&DC	
		${}^4\text{S}_{3/2}$	${}^4\text{I}_{15/2}$	550 nm	UC&DC	
		${}^4\text{F}_{9/2}$	${}^4\text{I}_{15/2}$	650 nm	UC&DC	
		${}^4\text{I}_{9/2}$	${}^4\text{I}_{15/2}$	800 nm	UC&DC	
Tm	${}^3\text{H}_6$	${}^1\text{G}_4$	${}^3\text{H}_6$	478 nm	UC&DC	54-56
			${}^3\text{F}_4$	650 nm	UC&DC	
			${}^3\text{H}_5$	777 nm	UC&DC	
		${}^1\text{D}_2$	${}^3\text{F}_4$	450 nm	UC&DC	
			${}^3\text{F}_2$	788 nm	UC&DC	
		${}^3\text{H}_4$	${}^3\text{H}_5$	801 nm	UC&DC	
Yb	${}^2\text{F}_{7/2}$	${}^2\text{F}_{5/2}$	${}^2\text{F}_{7/2}$	980 nm	DC	57

1.1.3.1. Mechanisms of down-shifting process

Based on the dopants and host lattice, the down-shifting, down-conversion and upconversion has alternative mechanisms of energy transfer. For DS process in Ln-doped NPs, the dopants can be single dopant or co-dopants. Meanwhile, the energy band of host lattice affects the energy transfer as well. The typical DS process in Ln ions shows in Figure 4. Figure 4a shows a single dopant condition, such as the 4f-5f transition in Ce^{3+} doped NPs.⁵⁸ However, if the excitation energy is no efficient to exit the single

dopant ions, the usage of co-dopants are a solution, as Figure 4b shows. One dopant is worked as sensitizer, which can be excited and sequentially transfer the emission energy to the other dopant. The energy acceptor of this dopant is called activator. Shinde *et al.* used Ce^{3+} as sensitizer and Dy^{3+} as activator.⁵⁹ The DS process shown in Figure 4c can be observed in the Ln-doped semiconductors. The excitation energy transferred from semiconductor host to lanthanide dopant is attributed to the absorption transition of valence band to conduction band in semiconductors. Pan *et al.* reported such energy transfer in Er-doped ZnO NPs.⁶⁰

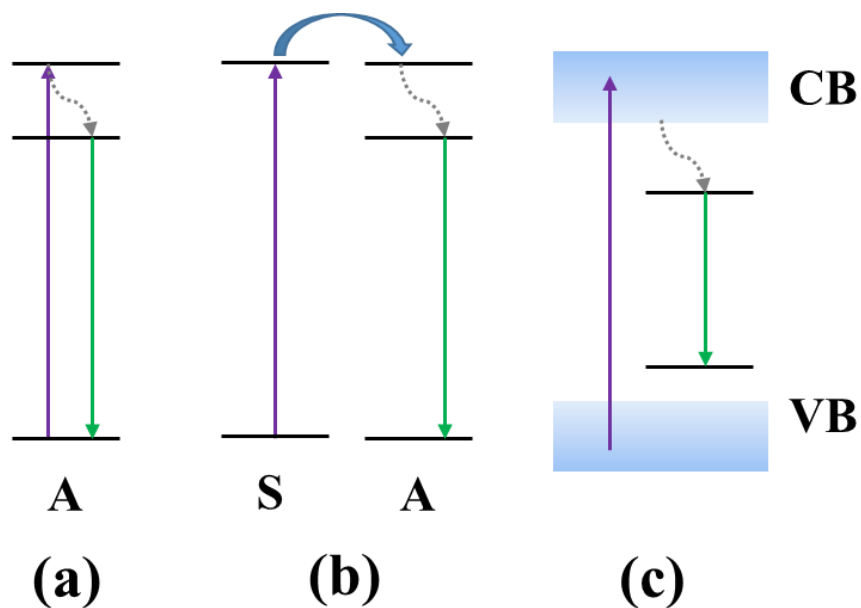


Figure 4. The typical energy transfer of DS process in Ln ions.

1.1.3.2. Mechanisms of down-conversion process

Furthermore, the energy transfer of UC processes did not specialized until 1966 by Auzel.⁶¹ According to the upconversion process of Ln-doped NPs, Wegh *et al.*

outlined the concept of downconversion in LiGdF₄:Eu NPs.⁶² The typical downconversion process in Ln ions was shown in Figure 5. Figure 5a shows a single dopant condition, whereas Figure 5b-c shows the co-dopant conditions. In Figure 5b case, the emission energy is transferred from the excitation state of Ion A to the excitation state of ion B. In Figure 5b, the cross relaxation occurs between the excitation state of Ion A and the ground state of Ion B. As Figure 5c shows, both energy transfer and cross relaxation occur. Partial emission energy of Ion A is transferred to the excitation state of Ion B, and partial emission energy of Ion A is transferred as cross relaxation. The mechanism of down-conversion was reported and summarized by Wegh *et al.*⁶³ In these four cases of DC in Ln-doped materials, the lanthanide ions absorb one high energy photon and emit two low energy photons.

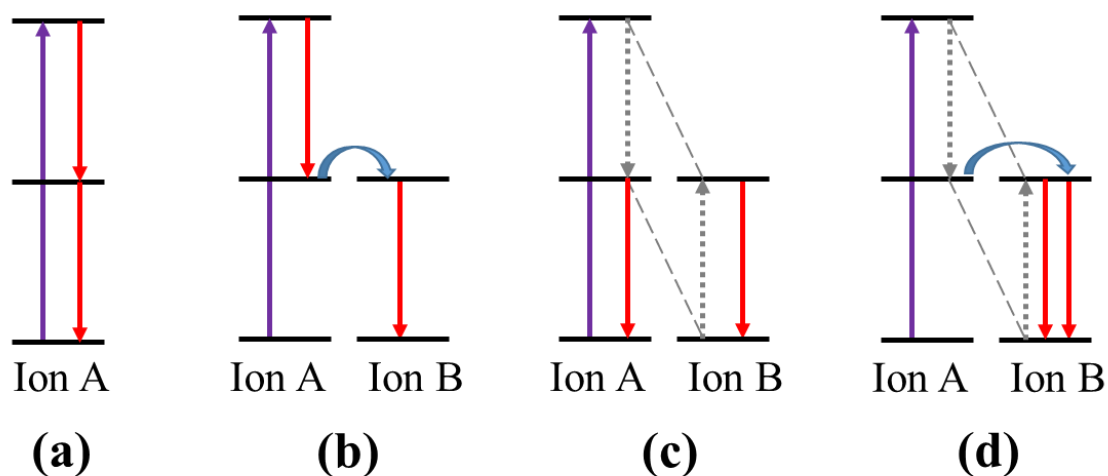


Figure 5. The typical energy transfer of DC process in Ln ions. (Purple: absorption; Blue: energy transfer; Red: emission; Gray: cross relaxation)

1.1.3.3. Mechanisms of up-conversion process

The typical UC processes mechanism in Ln ions shows in Figure 6, they are: excited-state absorption (ESA), energy transfer upconversion (ETU), cooperative sensitization upconversion (CSU), and photon avalanche (PA).⁶⁴⁻⁶⁸

Excited-state absorption (ESA) is a single Ln ion A excited from ground state to excited state via a successive absorption of two or more low energy photons, shown in Figure 6a. Energy transfer upconversion (ETU) involves two Ln ion dopants. Ion A works as a sensitizer and Ion B is activator. The energy is successively transferred from Ion A to Ion B in order to excite the Ion B to its upper emitting state, as Figure 6b shows. Unlike ESA and ETU, who have an intermediate excitation state of activator, cooperative sensitization upconversion (CSU) can be without intermediate state. As Figure 6c shows, two sensitizers of Ion A absorb pump photons and simultaneously transfer the energy to the emitting state of neighboring activator Ion B, followed by UC emission to the ground state of Ion B. Photon avalanche (PA) in Figure 6d was firstly reported by Chivian et al. in Pr^{3+} -based infrared quantum counters.⁶⁹ In order to achieve PA process, the excitation energy should be greater than a threshold value. The intermediate state of Ion B is populated firstly by a non-resonant weak ground state absorption process, followed by an ESA process to populate the upper emitting state. A cross-relaxation transfer occurs between the upper emitting state of Ion B and the ground state of Ion A, leading to both ions populate intermediate state. Last, with energy transfer from Ion A to Ion B, the emitting state of Ion B is populated and produces upconversion

emission. In these four cases of UC in Ln-doped materials, the lanthanide ions absorb two or more low energy photons and emit one high energy photons.

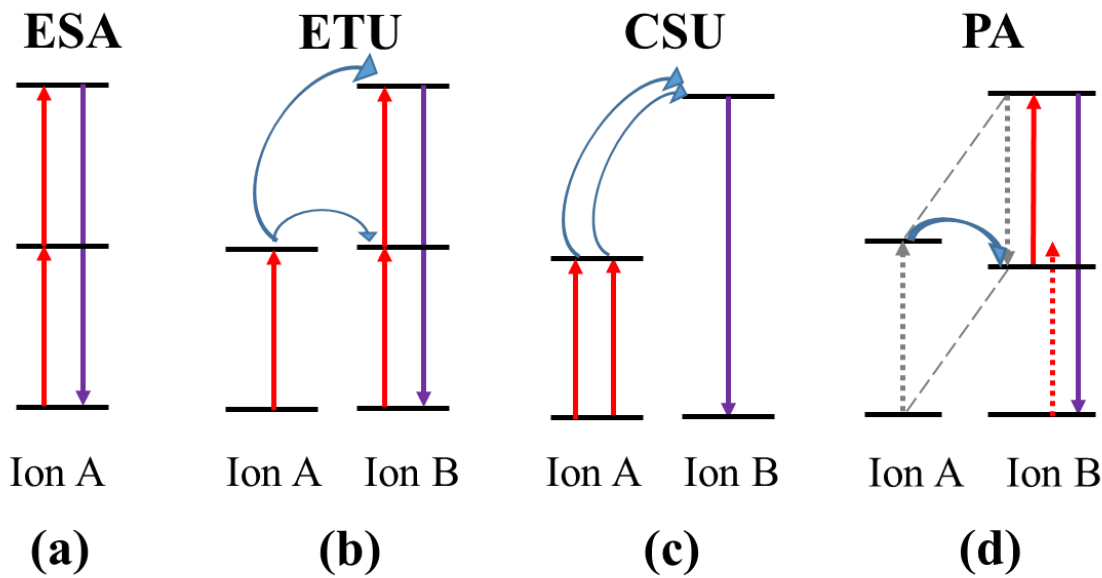


Figure 6. The typical energy transfer of UC process in Ln ions. (Solid red: absorption; Dash red: non-resonant ground state absorption; Blue: energy transfer; Purple: emission; Gray: cross relaxation)

1.2. Imaging techniques

Detection of ENPs in organisms and the environment is a challenge. Current modalities that have been used for detection include electron microscopy,⁷⁰ optical,⁷¹ magnetic resonance imaging (MRI),⁷² positron emission tomography (PET),⁷³ ultrasound,⁷⁴ and X-ray computed tomography (CT)⁷⁵. Optical imaging has been reported for studies of molecular structure.^{76,77} Techniques such as MRI and PET can provide whole-body information, but because have limitations on their resolution and contrast that make it difficult to detect many ENPs.⁷⁸ Ultrasound has low image contrast and also has

limited contrast for ENPs.⁷⁹ X-ray CT has been used to detect ENPs in tissue with high resolution and deep penetration;⁸⁰ dual energy scanning can take this capability one step further, allowing confirmation of the chemical identity of different species.^{81,82} The comparison of current commonly used imaging techniques was list in Table 3.

Table 3. Comparison of current commonly used imaging techniques.

Techniques	Resolutions	Prons	Cons	Applications	Ref.
Electron microscopy	Nanoscale	High resolution; Scanning fast;	Limitation in penetration	Observation of molecular structure	70
Optical imaging	Microscale	Cheap; In vivo; Less harmful; Scanning fast; Easy operation;	Limitation in penetration	Both molecular and whole body imaging	71
MRI	Microscale	High penetration; High contrast; In vivo	Expensive; Longer time,	Visualization in 3D to observe cross section	72
PET	1-2 mm	High contrast; High penetration; In vivo;	Expensive; Longer time;	Visualization in 3D to observe cross section	73
Ultrasound	Microscale	In vivo; Less harmful	Low contrast	Vascular imaging	74
CT	Microscale	High penetration;	Expensive; Longer time	Visualization in 3D to observe cross section	75

The most outstanding advantage of the Ln-doped NPs is their excellent optical performance, therefore, Ln-doped NPs is good to be used as imaging contrast agent. Meanwhile, the lanthanide elements have higher atomic numbers Z and K-edge energy values than organism tissues, resulting in a good application in X-ray tomography as contrast agents.⁸³

1.2.1. Optical confocal microscopy

Optical confocal microscopy is most commonly used optical imaging technique to test luminescent materials. Optical imaging with luminescent probes is a widely used strategy to detect bio-chemicals and biomolecules with in vivo and ex vivo. Figure 7 shows a typical home-made confocal microscope, which contains both imaging and spectrum detecting parts. When the mirror is positioned vertically, the optical path goes straightly to the image CCD (charge coupled device). Subsequently, when the mirror is positioned horizontally, the optical path is reflected by the mirror to the spectrum CCD to obtain emission spectra of samples.

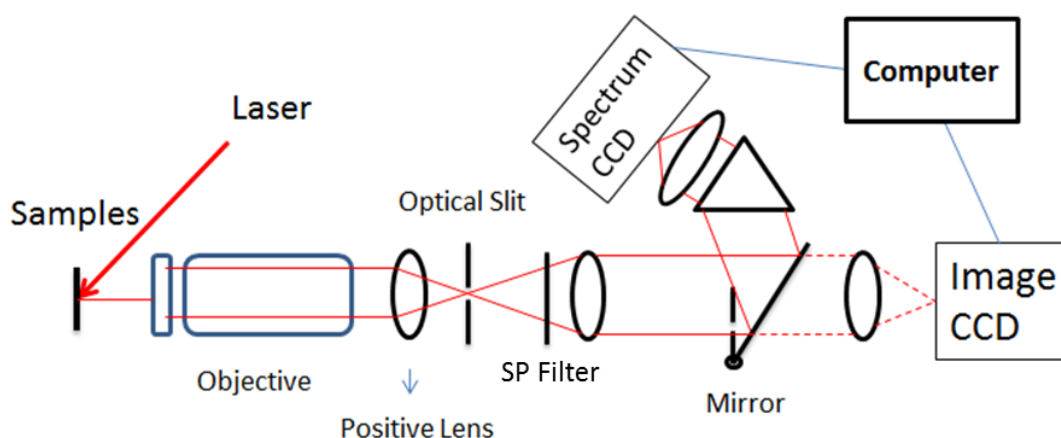


Figure 7. Schematic of a typical confocal spectrometer.

However, using lens in the optical system could cause chromatic aberration and spherical aberration, shown in Figure 8. As different color has different refraction index, the focal plane are different. This is called chromatic aberration. Spherical aberration commonly appears at the edge of lens, which leads to the light focusing at different point. To avoid these phenomena, a couple of mirrors can be used. Therefore, the

scanning range is increasing as well. Figure 9 shows the emission spectra of same samples tested by using lens and mirrors in the optical system.

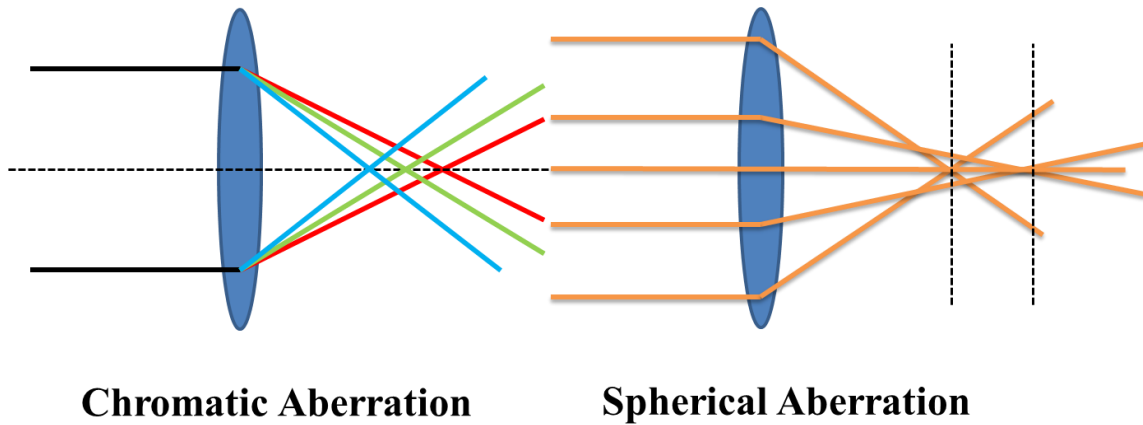


Figure 8. Aberration of using optical lens.

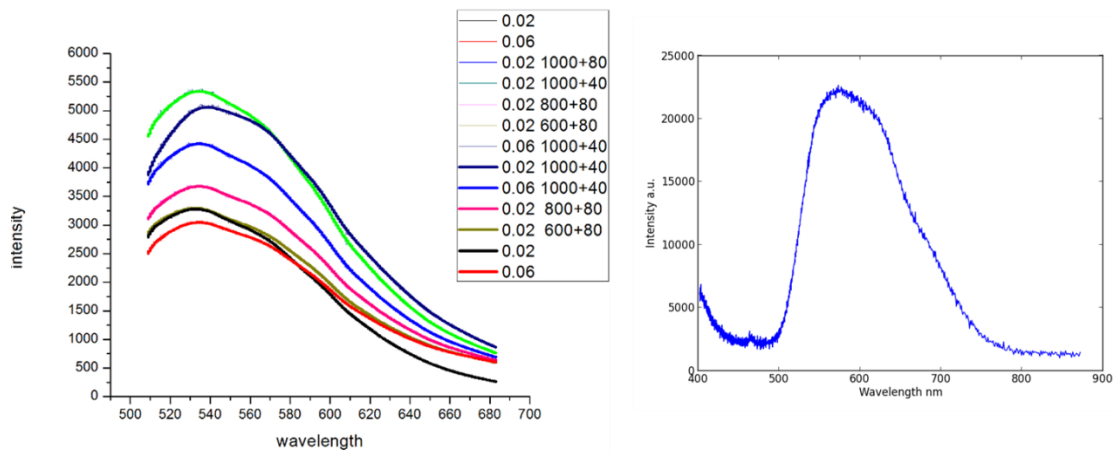


Figure 9. Improvement in emission spectra by using broad band spectrometer

1.2.2. Tomography

The X-ray computed tomography (CT) has commonly been used for medical imaging and diagnostics, as a non-destructive method to “cut” a patient into sections to reveal interior details⁸⁴. By combining numerous X-ray images taken of an object along a central axis at various angles, a cross sectional image of that object can be produced. Using an advanced software, these individual cross sections can be combined to construct a three-dimensional (3D) image of the entire object. Depending on the configuration, a synchrotron-based micro X-ray CT (μ -XCT) offers high resolution two-dimensional (2D) and 3D images at the micron scale^{85,86}. In addition, the μ -XCT scan can be utilized for a wide range of materials by adjusting the energy of the monochromatic X-ray^{86,87}. Although it is most common in medical applications, it has become a new method for detecting defects in industrial and electronic components in recent years. The high resolution of CT is capable of imaging cracks within industrial components, and defects within microelectromechanical systems (MEMS) and integrated circuits.

K-edge is the binding energy of K-shell electron for an atom. Once the photon energy of incident X-ray is greater than K-edge energy, the K-shell electron will be struck by X-ray and ejected from the original orbital (Figure 10a). Comparing emission with incident, X-ray energy is attenuated, which are absorbed by K-shell electron and scattered by samples. Once X-ray energy is smaller than K-edge, the attenuated energy of X-ray is reduced dramatically, as the K-shell electron stays at original orbital and does not absorb as much as the former condition (Figure 10b). Therefore, if we choose two

photon energies of X-ray close to K-edge of target element, we can obtain a sharp increase of mass attenuation coefficient. This sharp increase will be applied in identifying the target Y_2O_3 NPs within the body of samples (Figure 11).

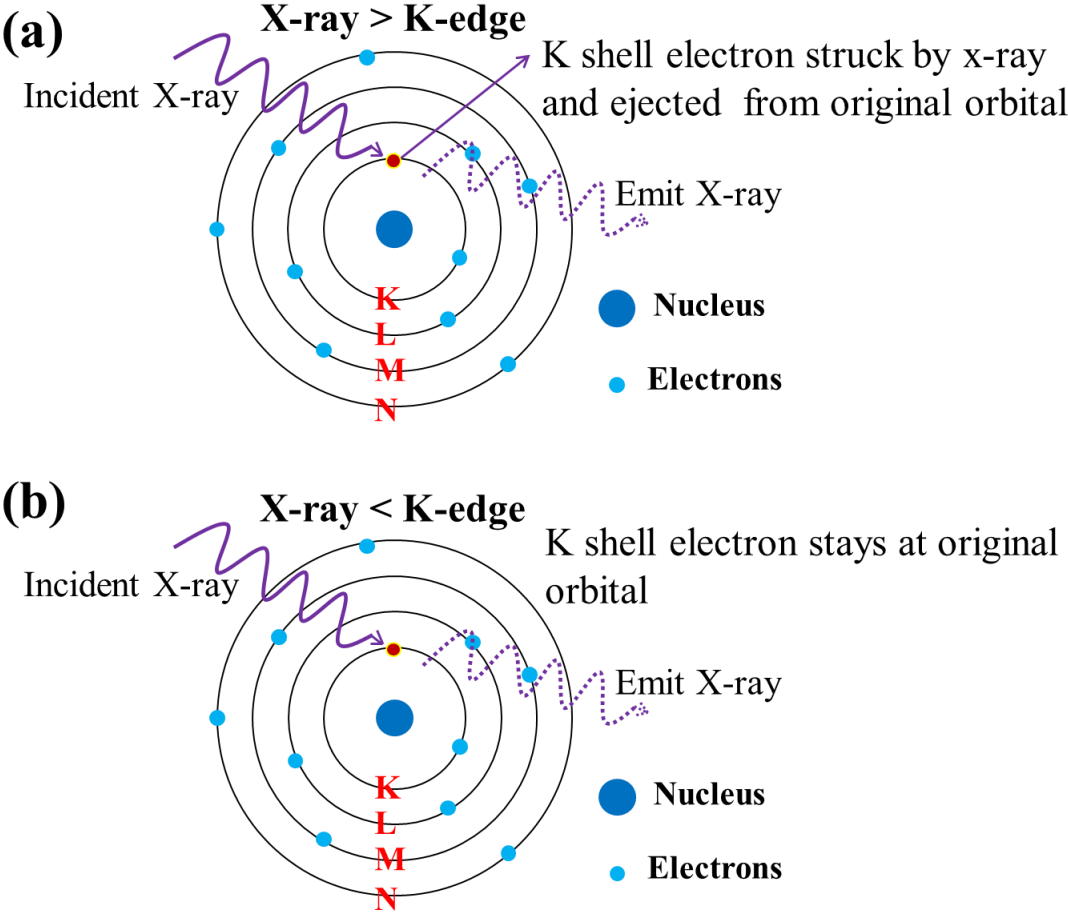


Figure 10. Schematic diagram showing the condition of the X-ray straddling K-edge.

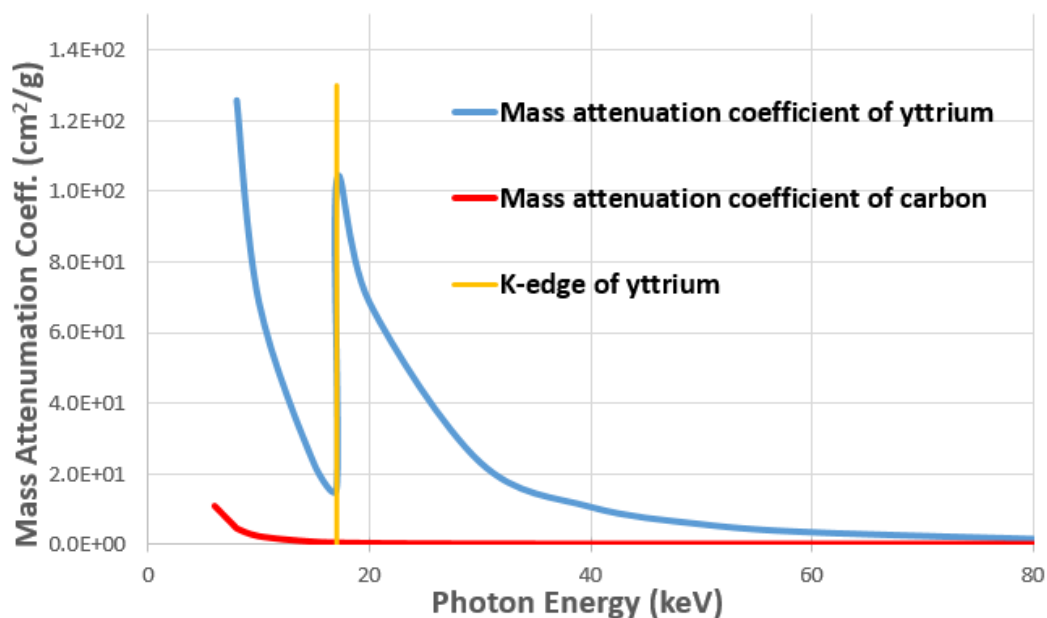


Figure 11. Graph of mass attenuation coefficient for carbon and yttrium. The value is derived from National Institute of Standards and Technology database (NIST X-ray Attenuation Databases).

1.3. Effects of lanthanide-doped NPs

1.3.1. Environment

Due to the widely usage of NPs, the probability of NPs exposure to environment is relatively high. Plants, as producers producing energy for other species, play a significant role in uptake and transfer NPs into food chain. Once the NPs accessed the water source by wastewater drain, the soil and plants would be exposed to the NPs. Once ENPs are uptaken by plants and translocated to the food chains, they could accumulate in organisms and even cause toxicity and biomagnification.^{88,89} The biomagnification, also named as bio-amplification, is an increasing concentration of certain toxic chemical accumulated in the tissue through the food chain. The higher level in a food chain, the higher toxicity, as Figure 12 shows. Therefore, once the Ln-doped NPs came into the

nature, such as waste water or soil, how would they transfer in the food chain will be a question. In order to observe the flow of NPs inside the body, the optical microscopy and X-ray tomography is a great approach to observe and analyze the pathway or distribution of NPs in the biological tissue.

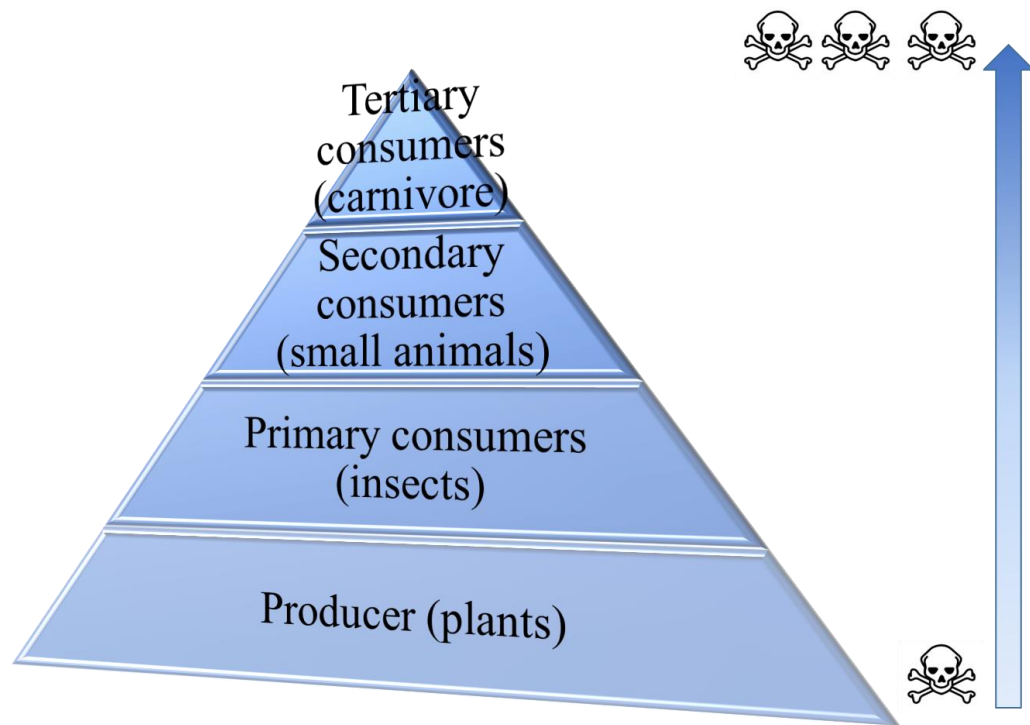


Figure 12. Schematic diagram of biomagnification in a food chain.

1.3.2. Optical device

Considering the excellent optical properties of Ln-doped NPs, one most common application of Ln-doped NPs is light emitting diode (LED). In addition, combining necessary colors, it is possible to obtain white LED. Coating Ln-doped

materials on a certain color chip is a commonly used method to make white LED, as Figure 13 shows.

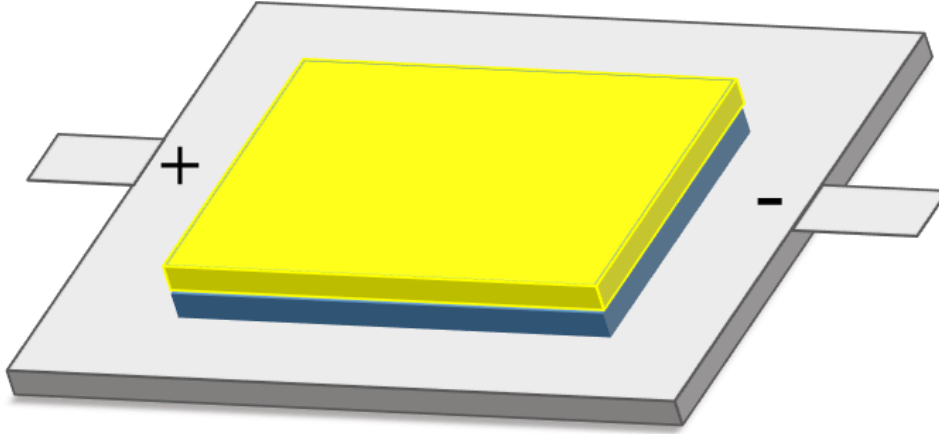


Figure 13. Schematic structure of white LED.

The CIE (Commission Internationale de l'Eclairage) 1931 chromaticity coordinates (x,y) can be calculated based on the emission spectra of specimen.⁹⁰⁻⁹³ The CIE1931 x and y chromaticity coordinates are expressed as equations (1-2):

$$x = \frac{X}{X + Y + Z} \quad (1)$$

$$y = \frac{Y}{X + Y + Z} \quad (2)$$

where X, Y and Z are defined as equations (3-5):

$$X = \int_a^b P(\lambda) \bar{x}(\lambda) d\lambda \quad (3)$$

$$Y = \int_a^b P(\lambda) \bar{y}(\lambda) d\lambda \quad (4)$$

$$Z = \int_a^b P(\lambda)\bar{z}(\lambda)d\lambda \quad (5)$$

where (a,b) is the range of emission spectrum and λ is the wavelength corresponding to the monochromatic light. $P(\lambda)$ is a spectral power distribution, which is related to the intensity of emission spectrum. The \bar{x} , \bar{y} , and \bar{z} are there color matching functions.

Based on the emission spectrum data, the CIE coordinates (x,y) can be calculated and marked in CIE diagram (Figure 14). Therefore, the luminescent color of specimen can be shown in CIE diagram.

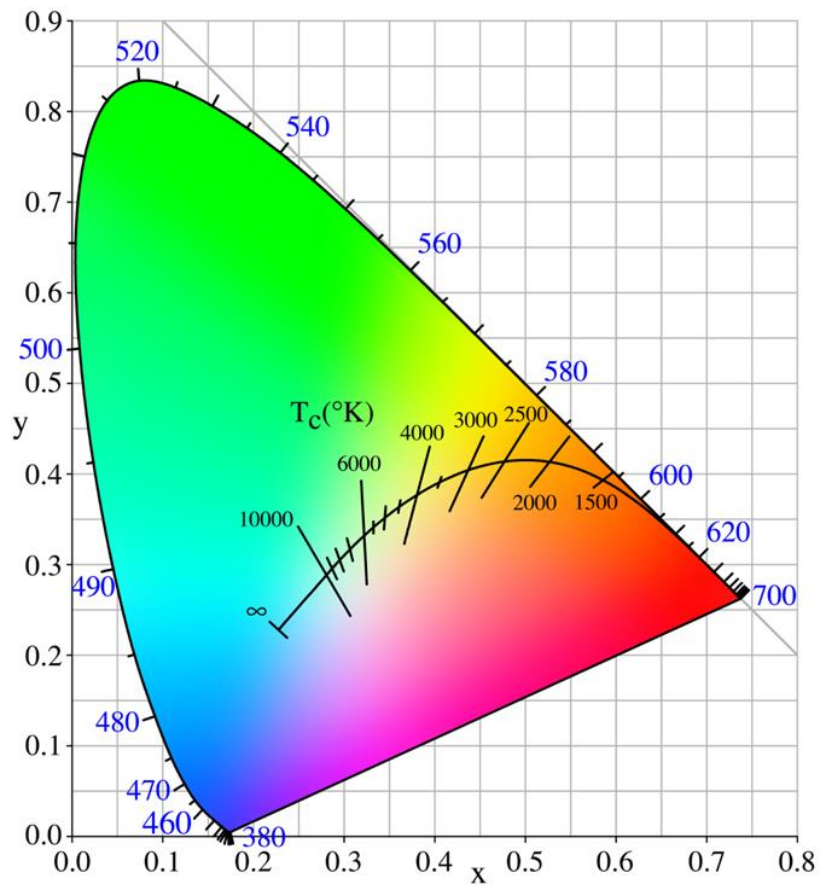


Figure 14. CIE1931 x and y chromaticity coordinate diagram.

1.3.3. Nanoparticles as additives in lubricants

Lubricants play important roles in daily activities such as driving, walking, and cooking. In mechanical systems, the friction and wear lead to the waste of energy and large drops on efficiency.⁹⁴ In order to reduce the friction and save energy, the lubricants are demanded. In today's worldwide market, lubricants are manufactured 40 million metric tons per year.⁹⁵ In recent years, engineered NPs have attracted great attention in lubricating additives due to the potential in energy saving. The additives The rare earth elements applied in oil lubricants have been widely studied, especially La and Ce.⁹⁶ The current understanding of mechanisms of lubrication, particularly in mechanical systems, has been limited by the lack of capability in direct observation. Basically, the grease consists three components (Figure 15). The base oil can be ester, silicon and so on, which occupy 70%. The thickeners are kinds of soap, which can produce solid or semisolid, occupying 20%. The left are additives, which can improve the properties, such as anti-wear. Currently, Atomic force microscopy and scanning electron microscopy are two most commonly used techniques to observe grease, as both have a high resolution.⁹⁷ Though both techniques can provide detail information of grease's surface, they cannot distinguish the three components and their distribution in three dimensional. The K-edge tomography was used to identify the thickeners/additives and study their distribution in 3D visualization. We found that this method can be employed for understanding the behavior of thickener and additive in a grease under a shear stress.

Grease

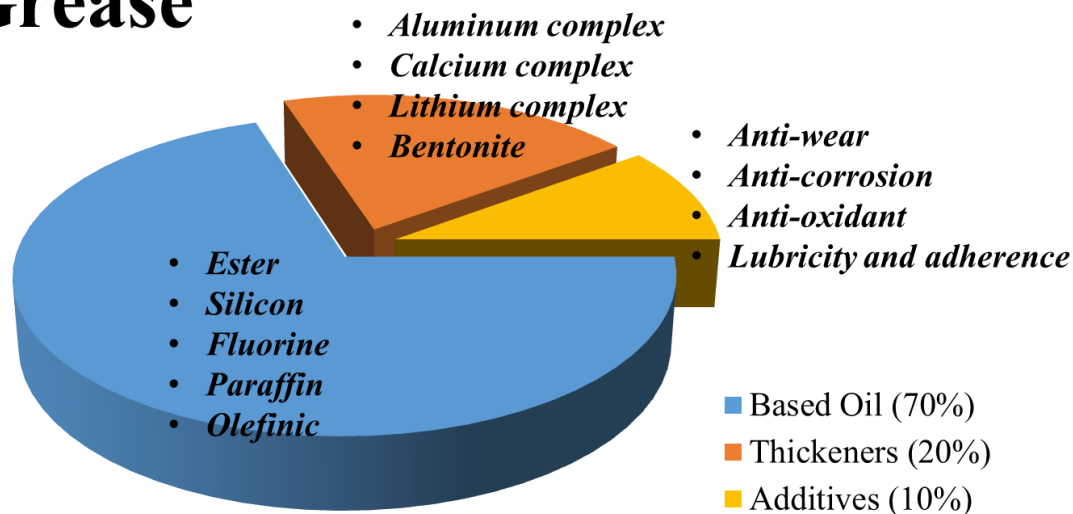


Figure 15. Components and their occupation of grease.

1.4. Summary

A basic background of lanthanide elements, imaging techniques and applications of lanthanide doped nanoparticles are introduced.

In this chapter, three luminescence conditions of Ln-doped NPs are presented. They are down-shifting, down-conversion and upconversion. Optical microscopy and X-ray tomography imaging techniques are introduced. Using Ln-doped NPs with imaging techniques, we can study and analyze the effects of Ln-doped NPs on environment, optical and oil lubricants.

CHAPTER II

MOTIVATION AND OBJECTIVES

Rare earth (RE) elements have excellent optical properties due to their specific 4f electron configuration. As discussed in Chapter I, RE-based nanomaterials have been intensely applied in bio-imaging, luminescence and lubricant. As RE-doped NPs were widely used, once engineered NPs are translocated to the food chains, they could accumulate in organisms and even cause toxicity and biomagnification. However, the systematic study in modifying optical performance of RE-doped NPs is still lacking. Moreover, in order to study the effects of NPs on environment, the contents and concentration of NPs in organisms were analyzed using an inductively coupled plasma mass spectrometry (ICP-MS); but this method cannot display the exact location of NPs in organisms simultaneously. Therefore, better approaches to study the optical performance and analyze the RE-doped NPs inside organisms are necessary.

2.1. Objectives

There are three major objectives of this research which are addressed in the following Figure 16.

2.1.1. Development of RE-doped NPs

The morphology and size of NPs have a great effect on the absorption of NPs by environment, such as plants and insects; and have an effect on the lubricating condition as well. Therefore, controlling the morphology is a critical factor. A novel approach to

control the morphology will be proposed in this research. Furthermore, because the well-dispersion of additives in oil can lead to a reduction in friction coefficient, we want to coat NPs with hydrophobic ligand so that the coated NPs can disperse uniformly in the mineral oil.

2.1.2. Control of optical performance through modification of RE-doped NPs

Considering the application of RE-doped NPs in bioimaging and luminescence, modifying their optical performance is necessary. Three approaches to control the optical performance will be reported in current work.

2.1.3. Identification of biological and engineering applications

As RE-doped NPs have excellent optical properties, they have been widely used in bio-imaging and optical device. We will apply NPs in biological system, such as ants, beetles, and plants, and engineering system, such as white LED and grease. In order to observe the NPs inside the specimen, optical confocal microscopy and tomography will be utilized.

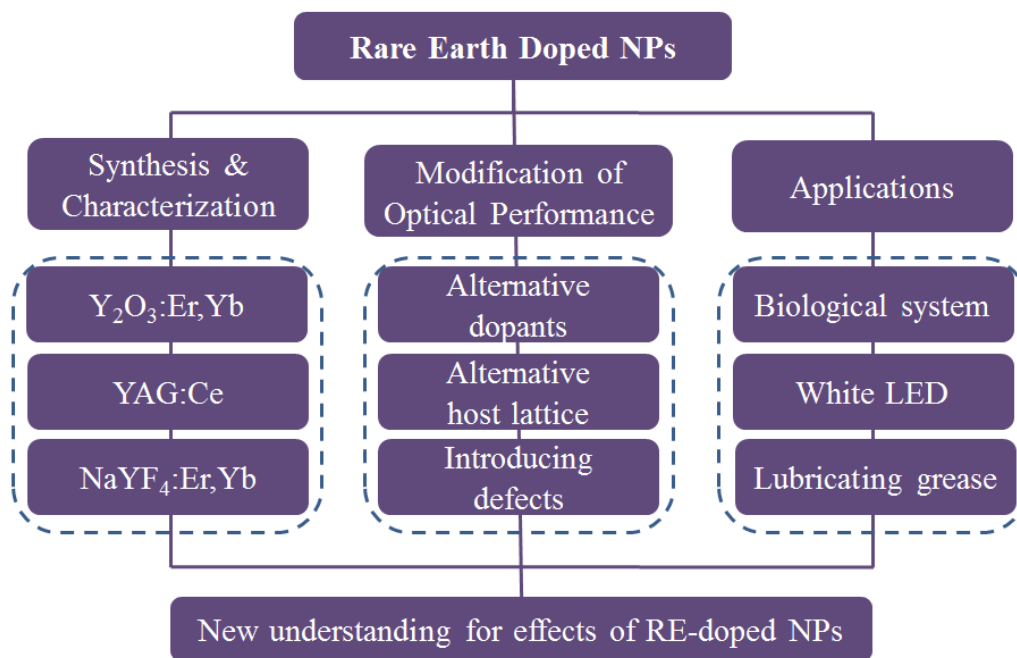


Figure 16. Research flow chart.

2.2. Dissertation structures

The Chapter I will give an introduction of RE elements and their applications. The motivations and objectives will be presented in Chapter II. Synthesizing and characterizing RE-doped NPs will be presented in Chapter III. Detailed discussion of modifying optical performance of RE-doped NPs will be presented in Chapter IV. The applications of NPs in biological and engineering system will be presented in Chapters V, and VI. Conclusions and future recommendations will be given in Chapter VII.

CHAPTER III

MATERIALS AND METHODS*

This chapter describes procedures and methods applied in the present research, shown in six sections. The first and second sections discuss about chemical agents and synthesis of three rare-earth-doped nanoparticles. They are erbium-ytterbium-doped yttrium oxide ($Y_2O_3:Er^{3+}, Yb^{3+}$) using hydrothermal method; aluminum yttrium oxide ($Y_3Al_5O_{12}$ or YAG) as host lattice doped with cerium ($YAG:Ce^{3+}$) or co-doped with erbium and ytterbium ($YAG:Er^{3+}, Yb^{3+}$) using modified polyol process; and erbium-ytterbium-doped oleic-acid-coated sodium yttrium fluoride ($OA-NaYF_4:Er^{3+}, Yb^{3+}$) using a typical thermalysis method. The technical details are given in the third section. The last section contains characterization of as-synthesized nanoparticles.

3.1. Materials

All chemicals in this study were purchased from Sigma-Aldrich (USA) and used without further purification. They are yttrium oxide (Y_2O_3) powder, erbium nitrate pentahydrate [$Er(NO_3)_3 \cdot 5H_2O$], ytterbium nitrate pentahydrate [$Yb(NO_3)_3 \cdot 5H_2O$], potassium hydroxide (KOH), nitric acid (HNO_3 , ACS reagent), aluminum oxide (Al_2O_3), and magnesium oxide (MgO) to synthesize the $Y_2O_3:Er^{3+}, Yb^{3+}$ nanoparticles. In order to

*Part of this chapter reproduced with permission from “*In situ* Investigation of the Growth of a Tribofilm Consisting NaYF₄ Fluorescent Nanoparticles” by Wei Dai and Yunyun Chen, et al., *Tribology Transactions*, Accepted (Copyright © 2017,).

synthesize yttrium aluminum oxide (YAG) nanoparticles, yttrium nitrate hexahydrate $[Y(NO_3)_3 \cdot 6H_2O]$, cerium nitrate hexahydrate $[Ce(NO_3)_3 \cdot 6H_2O]$, aluminum nitrate nonahydrate $[Al(NO_3)_3 \cdot 9H_2O]$, citric acid, polyvinylpyrrolidone (PVP) are used. For the host lattice of $NaYF_4$, oleic acid (OA), 1-Octadecene, sodium hydroxide (NaOH) and ammonium fluoride (NH_4F) are employed.

3.2. Synthesis of nanomaterials

3.2.1. Preparation of $Y_2O_3:Er^{3+}, Yb^{3+}$

In a typical procedure, 1.359 g Y_2O_3 powders were firstly dissolved into 250 mL HNO_3 solution (2.8 wt%) at $60^\circ C$ to obtain a transparent yttrium nitrate solution.⁹⁸ Then, a KOH solution (15 wt%) was added to the transparent yttrium nitrate solution to adjust the pH value at 10.5. When the pH value reached 7.0, some white floccules were appeared. The volume of resulting solution was 900 mL, and this turbid solution was transferred to a 2L non-stirred pressure vessel (Figure 17, general purpose, 4622Q, Parr Instrument), followed by sealing and heating up to $200^\circ C$ for 12 h. Once the reaction vessel cooling down to the room temperature, the precipitation were collected by the centrifugation, then washed by DI water three times and dried at room temperature. This as-synthesized precursor was denoted as B1.

Rare earth elements erbium (Er) and ytterbium (Yb) were selected to study their upconversion luminescent performance. The 1.34 g Y_2O_3 powders were firstly used to form the transparent yttrium nitrate solution, followed by adding 27 mg $Er(NO_3)_3 \cdot 5H_2O$ and 3 mg $Yb(NO_3)_3 \cdot 5H_2O$. The other steps were as same as that of B1. The Er^{3+} and

Yb^{3+} ions co-doped precursor was labeled as B2. Aluminum (Al) and magnesium (Mg) elements were utilized to examine the morphology controlling. For the first step, the 1.34 g Y_2O_3 powders with 2 mg Al_2O_3 or 1 mg MgO power were dissolved in 250 mL HNO_3 solution, and the remaining procedures were the same as B2. The precursor added with Al element was named as B3, and with Mg element as B4. The final products were obtained by calcining the precursors B1-B4 at 1000 °C for 3 hours in air. The calcinated samples were labeled as A1-A4. The samples and their symbols were listed in the Table 4.

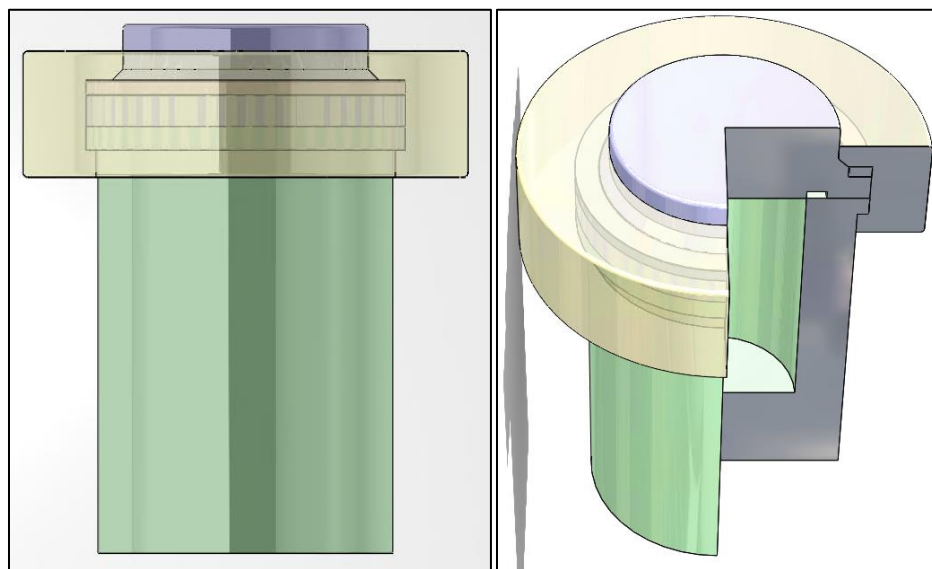


Figure 17. Schematic diagram of the non-stirred pressure vessel.

Table 4. The symbols of the samples before and after calcining.

Precursors	Symbol	Calcining at 1000°C	Symbol
$Y_4O(OH)_9NO_3$	B1	Y_2O_3	A1
$Y_4O(OH)_9NO_3:Er^{3+}, Yb^{3+}$	B2	$Y_2O_3:Er^{3+}, Yb^{3+}$	A2
$Y_4O(OH)_9NO_3:Er^{3+}, Yb^{3+}+Al$	B3	$Y_2O_3:Er^{3+}, Yb^{3+}+Al$	A3
$Y_4O(OH)_9NO_3:Er^{3+}, Yb^{3+}+Mg$	B4	$Y_2O_3:Er^{3+}, Yb^{3+}+Mg$	A4

3.2.2. YAG:Ce³⁺ and YAG:Er³⁺,Yb³⁺ Nanoparticles

A modified polyol process was employed to synthesize YAG:Ce³⁺ NPs⁹⁹. Two doping concentration of cerium were synthesized. For 6 mol% doping (YAG:6%Ce³⁺), 2.252 g Y(NO₃)₃·6H₂O, 3.751 g Al(NO₃)₃·9H₂O and 0.0521 g Ce(NO₃)₃·6H₂O were mixed in 20 mL DI water, followed by adding 3 g PVP and 10 g citric acid and stirring for 1h. For 2 mol% doping (YAG:6%Ce³⁺), 2.283 g Y(NO₃)₃·6H₂O, 3.751 g Al(NO₃)₃·9H₂O and 0.017 g Ce(NO₃)₃·6H₂O were used. The mixture was sequentially heated up to 80 °C in the heating mantle and kept stirring for 3h. The transparent solution was continually heat at 160 °C for 12h, and the solution was solidified into yellow-brown color. The yellow-brown products were grinded and calcined at 1000 °C for 1h. The as-synthesized YAG:Ce Nanoparticles were in yellow color and were hydrogenation in a gas flow of 80 sccm H₂ gas at 1000 °C for 1h, and flow of 40 sccm for 48h. Flow speeds were measured by a mass-flow controller (1179A, MKS Instruments). The final products are dark yellow powder.

In order to synthesizing YAG:Er³⁺,Yb³⁺ NPs, the molar ratio of 89:10:1 for Y:Yb:Er is used. The 2.045 g Y(NO₃)₃·6H₂O, 3.751 g Al(NO₃)₃·9H₂O, 0.269 g Yb(NO₃)₃·6H₂O and 0.027 g Er(NO₃)₃·6H₂O were mixed in 20 mL DI water, and the follow steps were as same as those of synthesizing YAG:Ce³⁺ NPs.

3.2.3. OA-coated NaYF₄ nanoparticles

Oleic acid mediated NaYF₄ NPs are commonly hydrophobic, synthesized by a typical thermolysis method¹⁰⁰. For the preparation of NaYF₄ NPs, 0.1 g NaOH and 0.148 g NH₄F were mixed in 10 mL methanol solution. Another solution was 0.89 mmol Y(NO₃)₃·6H₂O, 0.1 mmol Yb(NO₃)₃·5H₂O and 0.01 mmol Er(NO₃)₃·5H₂O mixed in 15 ml 1-Octadecene and 6 mL oleic acid (OA) solution. The second solution was prepared in a three-neck round-bottom flask and heated at 160 °C and stirred for 30 mins. The first solution was then slowly added in the flask (to avoid intense boiling) and kept 160 °C heating for 30 mins under the protection gas of Ar. Once no bubbles were generated, the mixture was heated up to 300 °C for 1 hour. After cooling down to temperature, the mixture was removed from the Ar atmosphere and mixed with ethanol, followed by centrifuging at 7000 rpm. The as-synthesized precipitation was mixed with ethanol and centrifuged repeatedly for 2 times. The final precipitation was dried at 40 °C for 36 h. The synthesizing system was shown in Figure 18.

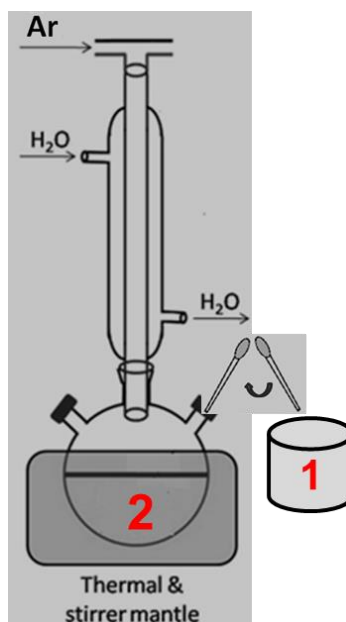


Figure 18. Schematic diagram of thermalysis system.

3.3. Methods of characterization

3.3.1. Crystal structure and morphology

The crystal structures were measured by using X-ray diffraction (XRD). The XRD diffractometer is a Bruker-AXS D8 advanced Bragg-Brentano with Cu Ka radiation ($\lambda=1.5418 \text{ \AA}$) operated at 40 mA and 40 kV. The size and morphology of the samples were measured by using a transmission electron microscope (TEM, JEOL 1200 EX) with an accelerating voltage of 100 keV. The high resolution TEM images were carried out by using JEOL JEM-2010 with an accelerating voltage of 200 keV. The Energy-dispersive X-ray spectroscopy (EDS, Oxford Instruments ATW type) detector with TEM platform was applied for chemical analysis.

3.3.2. Confocal microscopy experiments

The other home-made confocal laser scanning microscope with higher resolution was conducted to measure the samples to obtain emission spectra and optical imaging in both two-dimensional and three-dimensional (Figure 19). The 980 nm near infrared and 473 nm blue lasers were applied to scan the samples. The upconversion luminescence images were obtained with 10x lens and a starlight camera (Trius camera model SX-674).

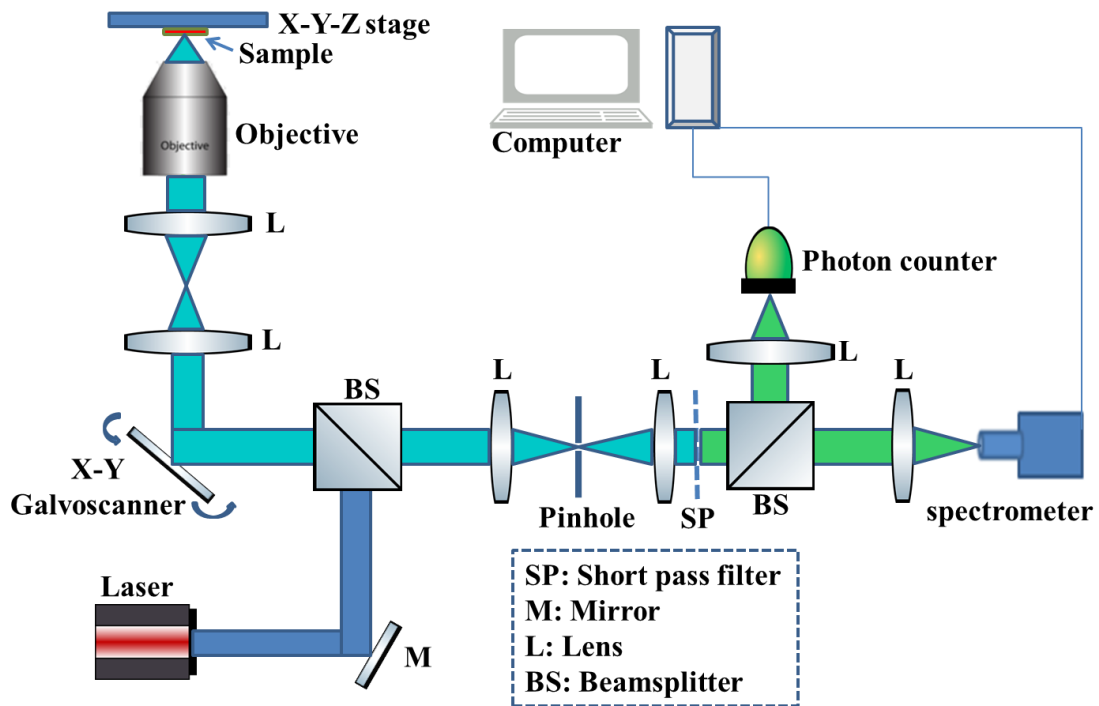


Figure 19. Schematic drawing of a confocal laser scanning microscope setup consisting of a 4f imaging system, a photon counter, and a spectrometer.

3.3.3. Synchrotron X-ray micro-tomography experiments

The synchrotron X-ray micro-tomography experiments were conducted at Advanced Light Source (ALS) beamline 8.3.2, Lawrence Berkeley National Lab (Figure 20). The Imaging energies of 17.3 keV and 16.7 keV were selected, straddling the Yttrium K-edge energy. Using a LuAG scintillator, pco.Edge scientific CMOS camera and 2x optical lens yielded a pixel size of 0.00329 mm. The exposure time for scanning specimens was 200ms. Radiographs were acquired, with 512 projections over 180° rotation. The cross-section image datasets were reconstructed by using a Fourier method implemented in the commercial Octopus package. The K-edge subtracted datasets are obtained by subtraction of the 16.7 keV reconstructed 32-bit images from the 17.3 keV images. The three-dimensional (3D) visualization of the distribution of NPs in the mealworms was performed with the Avizo software package (FEI).

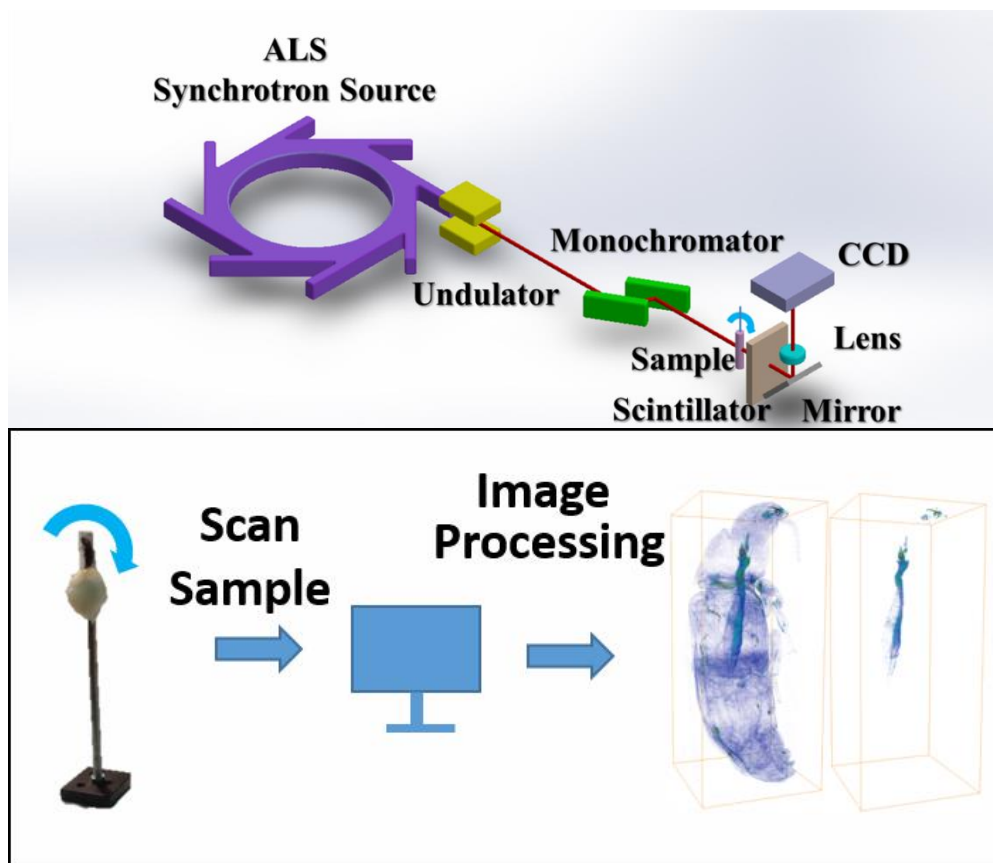


Figure 20. Schematic diagram of beamline 8.3.2 constructing 3D visualization.

3.4. Characteristics and properties of nanoparticles

3.4.1. $\text{Y}_2\text{O}_3:\text{Er}^{3+}, \text{Yb}^{3+}$ nanoparticles

Morphology- and size- specific synthesis of engineered nanomaterials has attracted great interests due to their unique properties and behaviors in mechanical, optical, electronic, and biomedical applications¹⁰¹⁻¹⁰⁶. Hydrothermal synthesis is one of the commonly used synthesizing methods to prepare crystalline materials and fabricate functional materials with various sizes and morphologies¹⁰⁷⁻¹¹¹. Yttrium oxide (Y_2O_3) is one of the common rare earth oxides and typically used as host lattice for rare earth elements doping¹¹²⁻¹¹⁴. Yttrium oxide (Y_2O_3 , yttria) ENPs have been broadly used in

optics, electrics and biological applications due to their favorable thermal stability and mechanical and chemical durability.¹¹⁵⁻¹¹⁷ Y_2O_3 can be obtained from the calcinations of precursors. The precursor, synthesized by the hydrothermal method, has commonly two structures, $Y(OH)_3$ ^{118,119} and $Y_4O(OH)_9NO_3$.^{120,121}

In order to control the morphology of Y_2O_3 by using hydrothermal method, the most commonly used methods are changing reaction temperature and pH values.¹²² Besides changing reaction condition, introducing alternative organic agents during the hydrothermal treatment is another widely used techniques.^{118,119,123} For example, Ethylene glycol monoisopropyl ether (EGME) can control the shape of Y_2O_3 in nanosheets or nanorods.¹¹⁸ For the sake of controlling the morphology of Y_2O_3 and its precursor, utilizing organic reagents have been intensively studied; however few reports have investigated the effects of metal ions on the shape-controlled for. Based on the literature review, using the metal ions instead of organic agents, the morphology of zinc oxide (ZnO) was controlled with hydrothermal method.¹²⁴⁻¹²⁷ Therefore, we proposed a novel method to control the morphology of Y_2O_3 and its precursor by introducing the metal ions during the reaction.⁹⁸

The transmission electron microscopy (TEM) was carried out to study the morphology and size of as-synthesized NPs. Figure 21 shows the TEM images of samples B1 and B2. It is clear to see without dopants, the shape of processors is nanotubes. With Er and Yb elements doping into the host lattice, the shape of precursors includes both nanosheets and nanotubes. The lengths of nanotubes are from 200nm and up to several

micrometers, and the diameters of them are from 20 to 50 nm. The mean size of the nanosheets was around 250nm.

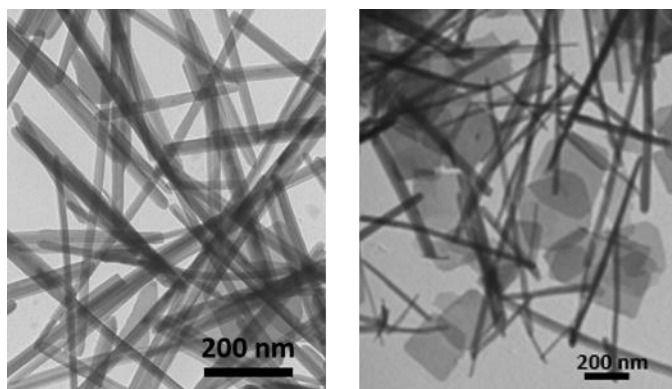


Figure 21. The TEM images of samples B1 and B2.

By introducing the Al^{3+} metal ions during the synthesis, the shapes of precursors B3 are both nanotubes and nanosheets as well (Figure 22a). After calcination, the mean diameter of nanotubes in sample A3 is 31.3 ± 8.6 nm, and the mean length is 206.3 ± 77.3 nm (Figure 22b). The average size of irregular nanoparticles is 64.9 ± 16.9 nm. The insets show the enlarged view of nanotube and nanosheets. Figure 22c shows the high resolution TEM images of sample A3. The clearly observed lattice fringes indicate the highly crystallinity of the nanotube and nanosheet. The lattice spacing of 0.53nm and 0.75 nm is corresponding to the d spacing of the (200) plane and (110) plane of the cubic lattice Y_2O_3 . The XRD pattern of as-synthesized NPs was finely indexed to a cubic phase of yttria (JCPDS card no. 83-0927), shown in Figure 22d. The as-calcined yttria NPs did not have further surface modification, therefore, the NPs were not water-soluble.

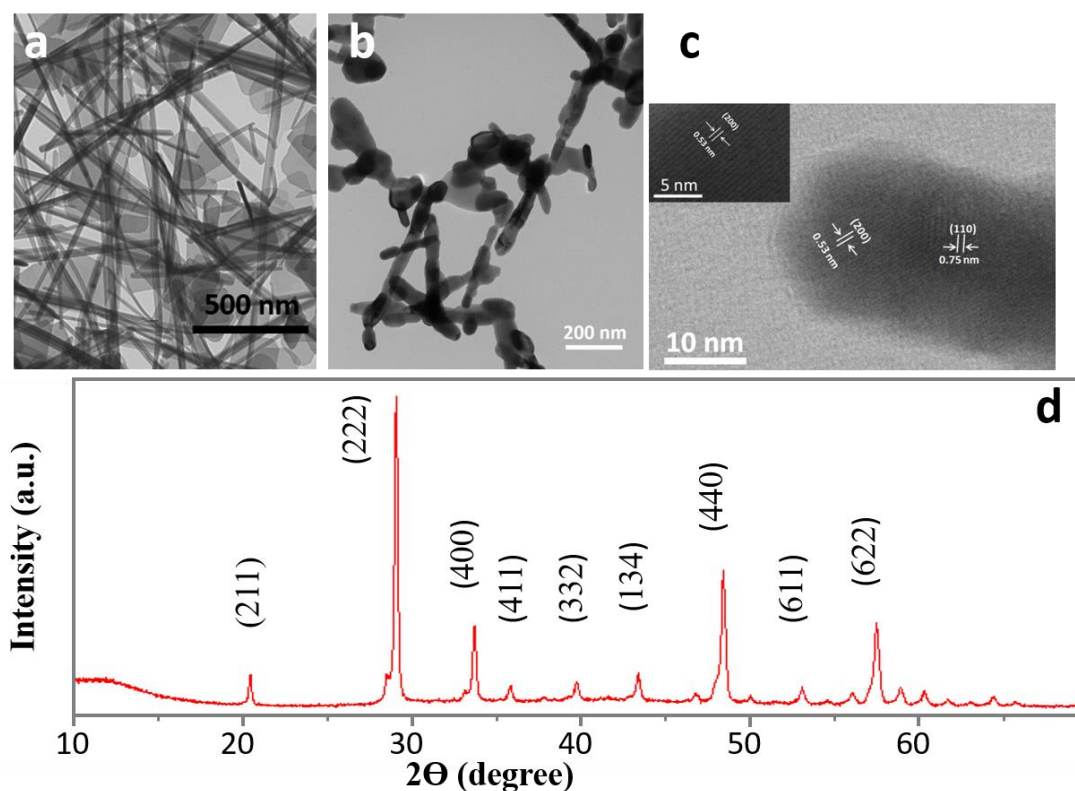


Figure 22. The TEM images of samples (a) B3 and (b) A3. (c) High resolution TEM image of A3. (d) The XRD pattern of sample A3.

By introducing the Mg^{2+} metal ions during the synthesis, the shapes of precursors B4 are mainly nanosheets (Figure 23a). After calcination of precursors B4, the as-calcined A4 are shrinkage. The size of A4 NPs is around 50 to 100 nm with rectangle-like two-dimensional shape (Figure 23b). Also, high magnification TEM images of the nanoparticles are shown in (Figure 23c). The lattice spacing of 0.75nm is corresponding to the d spacing of the (110) plane of the cubic lattice Y_2O_3 . The X-ray diffraction (XRD) pattern of as-calcined NPs was finely indexed to a cubic phase of yttria (Figure 23d, JCPDS card no. 83-0927).

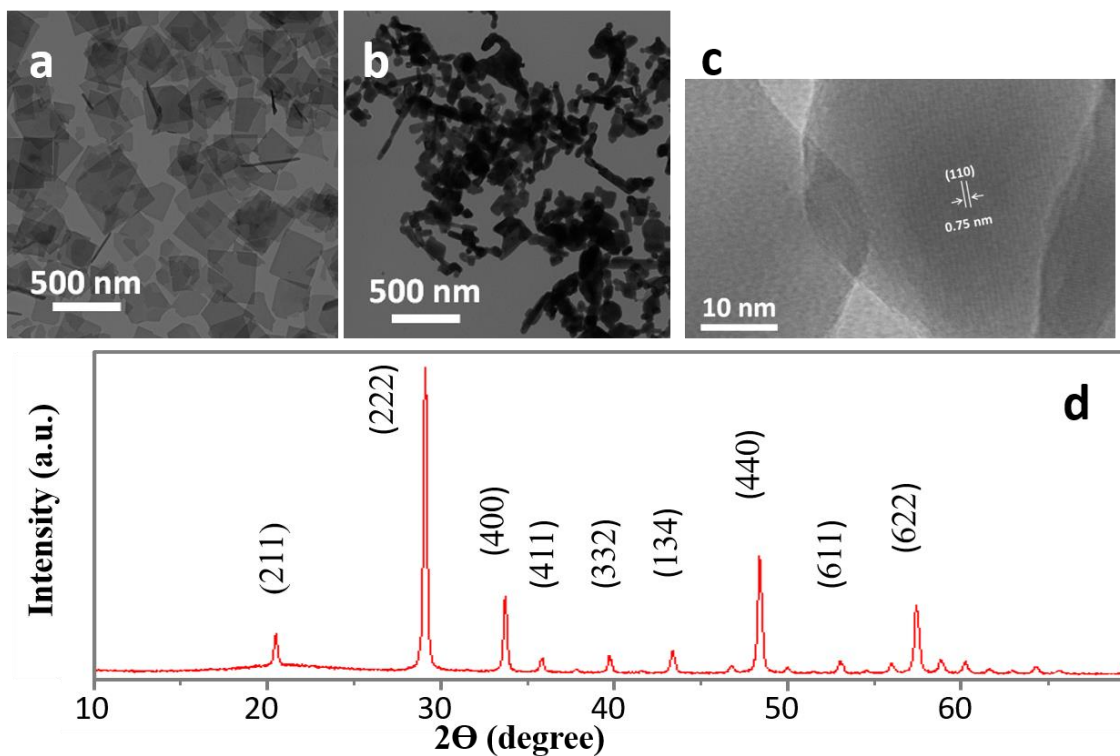


Figure 23. The TEM images of samples (a) B4 and (b) A4. (c) High resolution TEM image of A4. (d) The XRD pattern of sample A4.

Here we found that by introducing the metal ions, the morphology of Y_2O_3 and its precursor can be controlled. The shape-controlled synthesizing process of B1-B4 is clearly and schematically shown in Figure 24. The mechanism of shape-controlling process could be attributed to the different charges of alternative metal ions complexes. With alternative charging of metal ion complexes, the rolling-up process can be promoted or forbidden. Amounts of nanotubes rolled-up by nanosheets were studied.¹²⁸⁻¹³² With organic agents as an intersection to bond sheets, such as carbon nanotube, thereby the organics worked to control the morphology of the sample. In our study, the alternative charged metal ion complexes worked as an intersection to bond sheets. Once

the charge of metal ion complexes was opposite to free ions of K^+ in the solution, they would be attracted and get rid of the sheets. This would result in the rolling up. The rolling-up process for the formation of nanotubes from nanosheets shows in Figure 25. For instance, the Al ions can form negatively charged aluminate ($[Al(OH)_4]^-$) and neutral charged $Al(OH)_3$ at pH value 10.5, according to the speciation plot for Al as a function of pH.¹³³ The negatively charged $[Al(OH)_4]^-$ ions were attracted by the positively charged free K^+ ions. On the contrary, the magnesium complex ions were positively and neutral charged at pH 10.5,¹³⁴ the intersection for bonding nanosheets was prohibited, thereby the morphology of B4 was nanosheets and a few nanotubes.

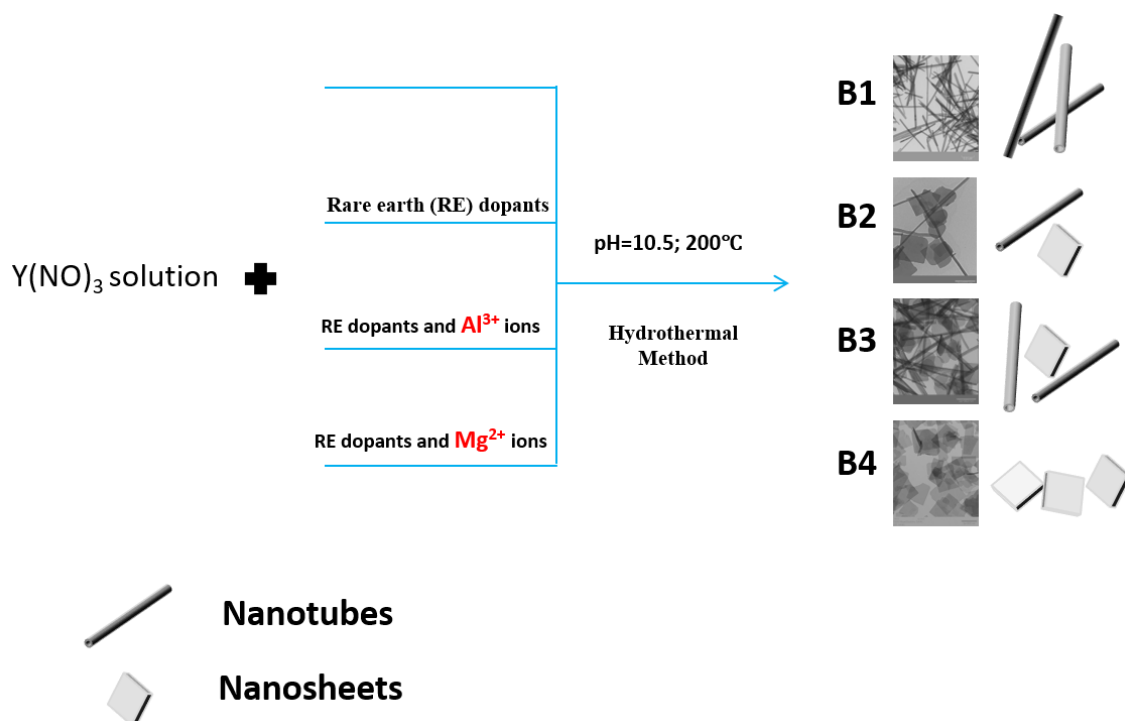


Figure 24. Schematic illustration for the formation of alternative shapes in samples B1-B4.

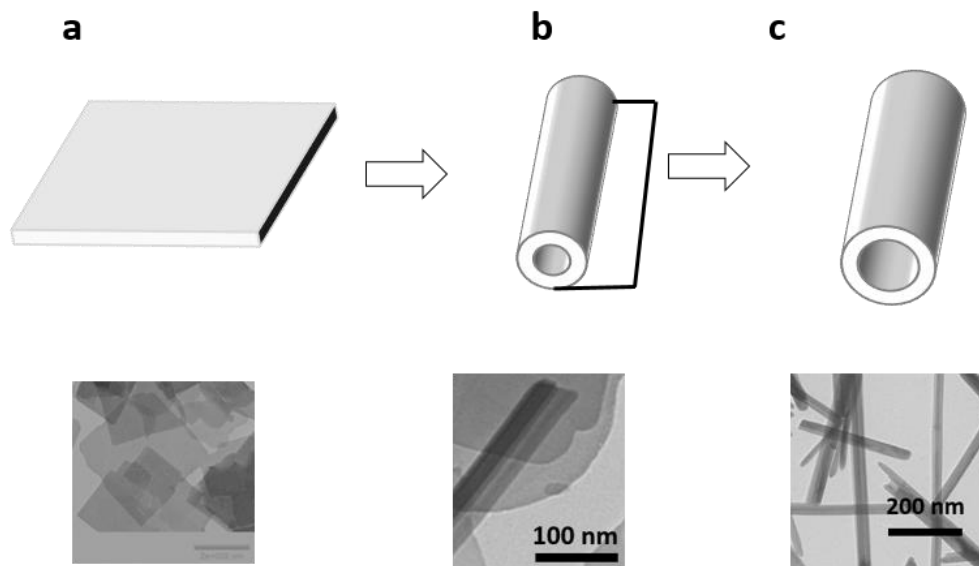


Figure 25. The rolling-up process for the formation of nanotubes from nanosheets

3.4.2. YAG:Ce³⁺ nanoparticles

Yttrium aluminum garnet Y₃Al₅O₁₂ (YAG) is a widely used solid state optical material. When doped with rare earth elements, YAG exhibits excellent luminescent properties and chemical stability.¹³⁵ Such type of materials has many applications such as lasers, refractive coatings, and mercury vapour lamps, among others.^{99,136,137} Rare earth elements are currently designated as nationally critical needed materials due to lack of supply. Understanding effects of rare earth elements on YAG would not only develop new knowledge in optical materials and bandgap engineering, but also enable to develop new materials potentially replace rare earth elements. This research focuses on trivalent cerium doped YAG (YAG:Ce³⁺).

After hydrogenation, the color of YAG:6%Ce³⁺ NPs changed from bright yellow to dark yellow (Figure 26). For the crystal structure of samples, The XRD patterns of

products were shown in Figure 27. Figure 27a represents the as-synthesized NPs before calcination. The nanoparticles were captured by the citric acid and capping agent PVP, therefore no crystalline peak was observed. Figure 27b is the NPs after calcination which is doped with 2 mol% Cerium. The peaks are formed by the phase of cubic yttrium aluminum oxide (orange line, JCPDS card no. 79-1892). During the calcination, the citric acid and PVP were decomposed; and NPs were crystalized. Figure 27c&d are the YAG:2%Ce³⁺ with hydrogen treatment for 1h and 48h, respectively. Figure 27e shows XRD pattenen of 6 mol% doped YAG, and its peaks are finely index as well. Figure 27f&g show the YAG:6%Ce³⁺ with hydrogen treatment for 1h and 48h. A new peak were observed, which was marked. Figure 28 shows the TEM images of YAG:Ce³⁺ NPs with hydrogenation. The NPs are random shape with average size of 60 nm. Figure 28b is the high resolution TEM image of NPs at atomic level. The lattice spacing of 0.49 nm is corresponding to the *d* spacing of the (211) plane of the cubic lattice YAG. Figure 29 is the EDS spectrum of NPs. Based on the results of EDS, the NPs consist of Ce, Y, Al, and O elements.

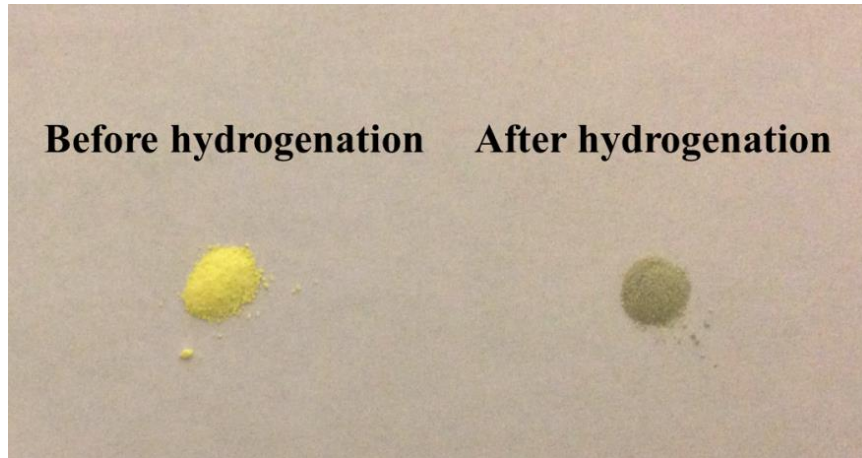


Figure 26. The color change of YAG:6%Ce³⁺ before and after hydrogenation

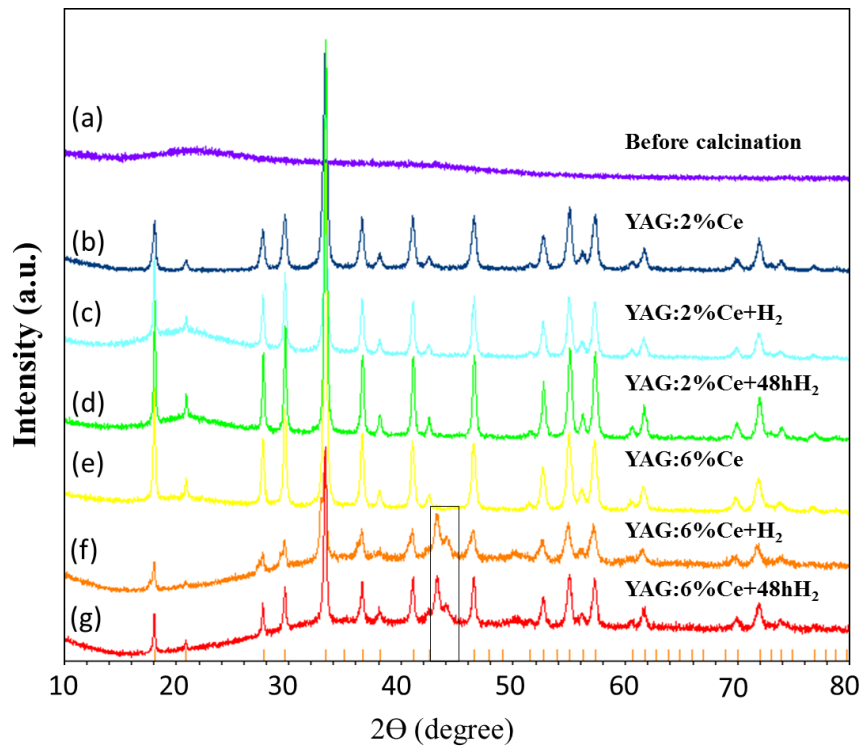


Figure 27. XRD patterns of as-synthesized YAG:Ce³⁺

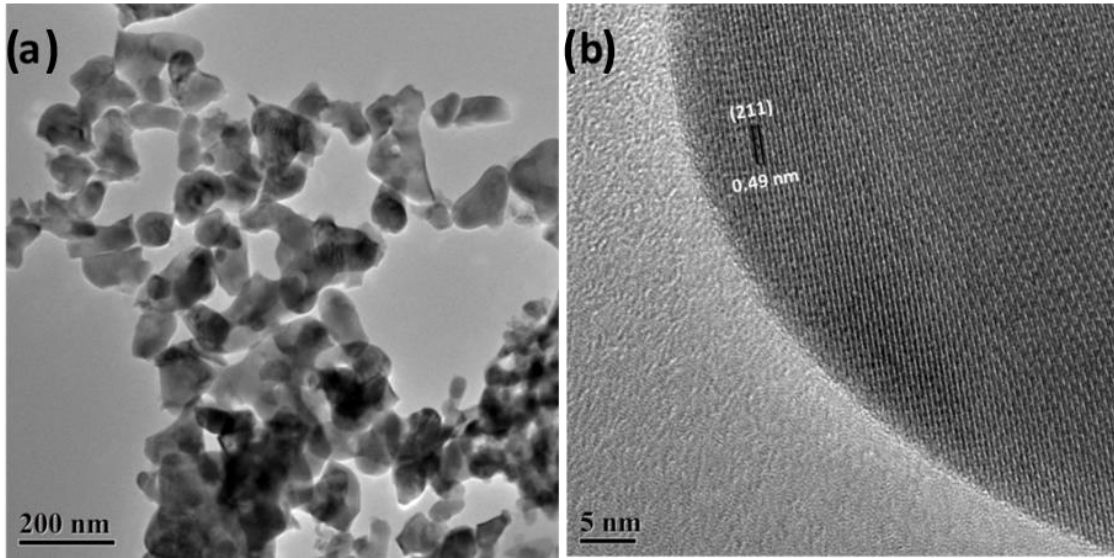


Figure 28. TEM images of YAG:6%Ce³⁺ with hydrogenation (a) low magnification, (b) high magnification.

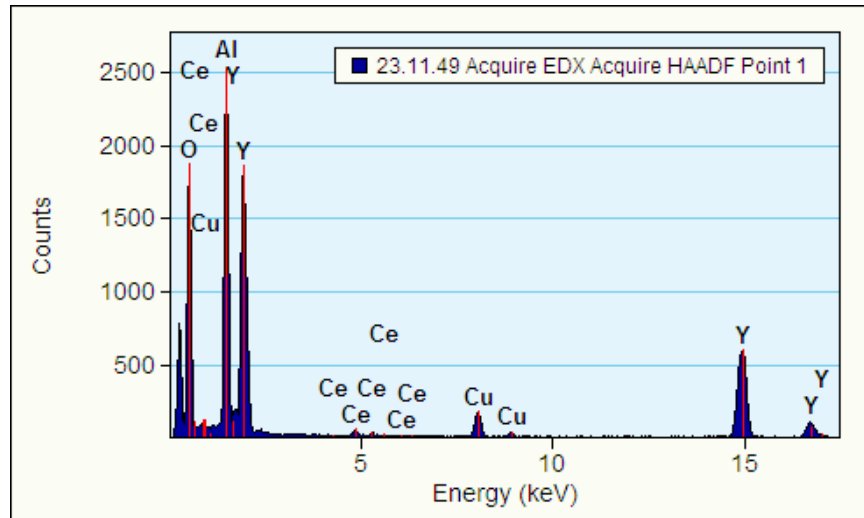


Figure 29. EDS spectrum of YAG:6%Ce

3.4.3. NaYF₄:Er³⁺,Yb³⁺ nanoparticles

The NaYF₄ is one of the most widely used host lattices, as the fluoride-based UCNPs has relatively low cutoff phonon energy¹³⁸. The NaYF₄:Er³⁺,Yb³⁺ NPs has been intense studied in biological application, such as bioimaging¹³⁹, biosensor¹⁴⁰, drug delivery¹⁴¹ and therapy¹⁴². The most commonly used synthesizing methods are hydrothermal and thermolysis methods¹⁰⁰. For the typical thermolysis method, the OA (oleic acid) is one of the most commonly used surfactants. The OA-coated NaYF₄:Er³⁺,Yb³⁺ NPs can be dispersed well in nonpolar organic solvent, such as hexane and cyclohexane¹⁴³. As mineral oil is a type of nonpolar oil, OA-coated NaYF₄:Er³⁺,Yb³⁺ NPs would be a potential excellent additives. Figure 30 shows the well dispersion of OA-coated NaYF₄:Er³⁺,Yb³⁺ in nonpolar organic solvent, the hexane and mineral oil.

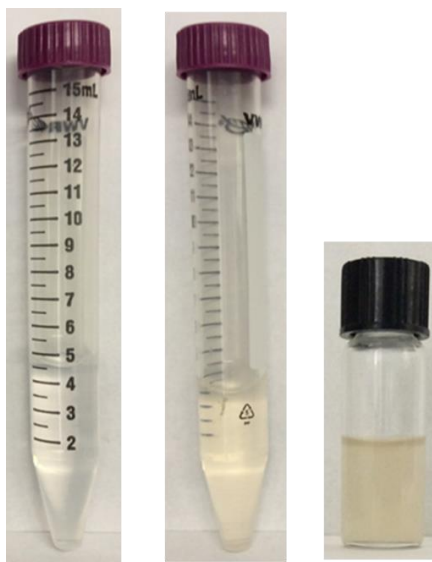


Figure 30. Dispersion of NPs in nonpolar organic solvents. From left to right, the three samples are mineral oil, 1 wt% NaYF₄:Er³⁺,Yb³⁺ in mineral oil, and 1 wt% NaYF₄:Er³⁺,Yb³⁺ in hexane

The high resolution TEM image was obtained by using a transmission electron microscope (JEOL JEM-2100) with an accelerating voltage of 200 keV (Figure 31). The NaYF₄ NPs were sonicated in ethanol solution for the preparation of TEM study. As OA-mediated NPs were hydrophobic, the NPs were aggregated in ethanol (Figure 31a). The size of NaYF₄ NPs was around 10 nm (Figure 31b). At relatively low magnification, there is no clear hollow structure in NaYF₄ NPs (Figure 31a&b). However, at high magnification, the hollow structures were appeared (Figure 31 1c&d). This can be caused by the high density of electron beam at high magnification. Feng *et al.* observed and reported a similar hollow structure of NaYF₄ NPs as well ¹⁴⁴. During the synthesizing, the central region of NPs formed micelle structures with the organic agents, the oleic acid (OA). With longer time and high density exited by electron beam, the organic micelles were decomposed and generated small voids surrounding themselves. Finally, a fixed hollow structure was generated in the center. The process of generating hollow structure shows in Figure 32. The lattice spacing of 0.258 nm is corresponding to the d spacing of the (200) plane of the hexagonal lattice of NaYF₄ NPs.

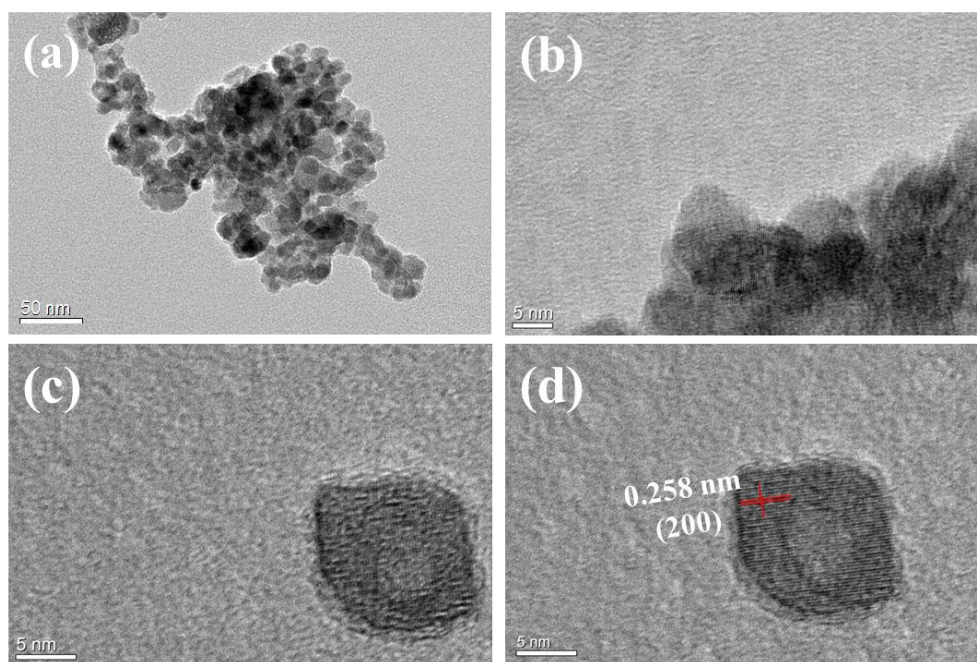


Figure 31. TEM images of as-synthesized NaYF₄ NPs with thermolysis method



Figure 32. The process of generating hollow structure in NPs.

3.5. Summary

In this chapter, synthesis and characterization of three rare earth doped nanomaterials are discussed. They are yttrium oxide (Y₂O₃), yttrium aluminum oxide (YAG), and sodium yttrium fluoride (NaYF₄) nanoparticles. The doped rare earth element is cerium (Ce) to obtain down-conversion performance, or erbium (Er) and ytterbium (Yb) co-dopant to achieve up-conversion optical property.

Effects of metal ions on the shape-controlled-hydrothermal synthesis

$\text{Y}_2\text{O}_3:\text{Er}^{3+}, \text{Yb}^{3+}$ are discussed first. During the reactions, alternative charged metal complex ions are introduced to control the morphology of NPs into nanotubes and nanosheets. When the pH value was 10.5, the negatively charged Al^{3+} complex ions enabled the evolution of nanotubes through rolling from nanosheets, whereas the positively charged Mg^{2+} complex ions prohibited the nanosheets from rolling up and forming nanotubes. In terms of upconversion luminescence, the red emission is attributed to $^4\text{F}_{9/2} \rightarrow ^4\text{I}_{15/2}$ energy level transition, and the green emission belongs to the transitions from $^2\text{H}_{11/2}/^4\text{S}_{3/2}$ to $^4\text{I}_{15/2}$ energy levels. Additionally, the addition of Mg^{2+} in synthesis increased the red-to-green emission ratio of the $\text{Y}_2\text{O}_3:\text{Er}^{3+}, \text{Yb}^{3+}$.

The YAG as host lattice was discussed sequentially. Both $\text{YAG}:\text{Ce}^{3+}$ and $\text{YAG}:\text{Er}^{3+}, \text{Yb}^{3+}$ were synthesized using a modified polyol method and have great optical properties. With alternative doped rare earth elements, the optical performances are utterly different. In addition, a red shift of $\text{YAG}:\text{Ce}^{3+}$ in emission spectrum is observed after the hydrogen treatment. With different dopant of rare earth elements, alternative optical properties are obtained: upconversion and downconversion luminescence.

$\text{NaYF}_4:\text{Er}^{3+}, \text{Yb}^{3+}$ nanoparticles are the third nanomaterials introduced in this research using a typical thermolysis method. During the process, oleic acid are coated on the NPs, which leads to a well dispersible of NPs in nonpolar organic agent. Therefore, besides the most common application in bio-imaging, OA-coated $\text{NaYF}_4:\text{Er}^{3+}, \text{Yb}^{3+}$ NPs is a good potential additive employed in lubricant.

CHAPTER IV

MODIFICATION OF OPTICAL PERFORMANCE THROUGH SYNTHESIS

This chapter discusses about the modification of optical performance. It contains three sections: the first section is focused on using alternative dopants to modify the optical performance; the second is discussing the effects of different host lattice on optical performance; the last is about introducing defects into crystal lattice.

4.1. Alternative dopants

In order to control the optical behavior, using alternative RE dopants is one of the most feasible approaches. As the energy states of lanthanide elements are diversity, the absorption and emission performance of NPs can be changed and predicted. In our study, the alternative dopants were applied in the same host lattice, the YAG:Ce and YAG:Er,Yb. The optical performance are totally different: one has down-shifting, the other has upconversion performance.

Using the same synthetic method of YAG:Ce, we doped YAG with Er and Yb element to produce the upconversion YAG:Er,Yb NPs. The XRD patterns of YAG:Ce and YAG:Er,Yb are well indexed with phase of cubic yttrium aluminum oxide as well (Figure 33). Though the dopants were changed, the XRD patterns of host lattice were the same. For the optical property, the YAG:Er,Yb NPs were excited with 980 nm NIR laser, and emit the color at green and red regions (Figure 34). This is an anti-Stokes shift by absorbing two or more low energy photon and emitting one high energy photon.

Compared with broad emission peak of YAG:Ce, the emission peaks of YAG:Er,Yb are sharp and narrow .This is because of the 4f-4f emission transition in Er ions and 5d-4f transition in Ce ions.

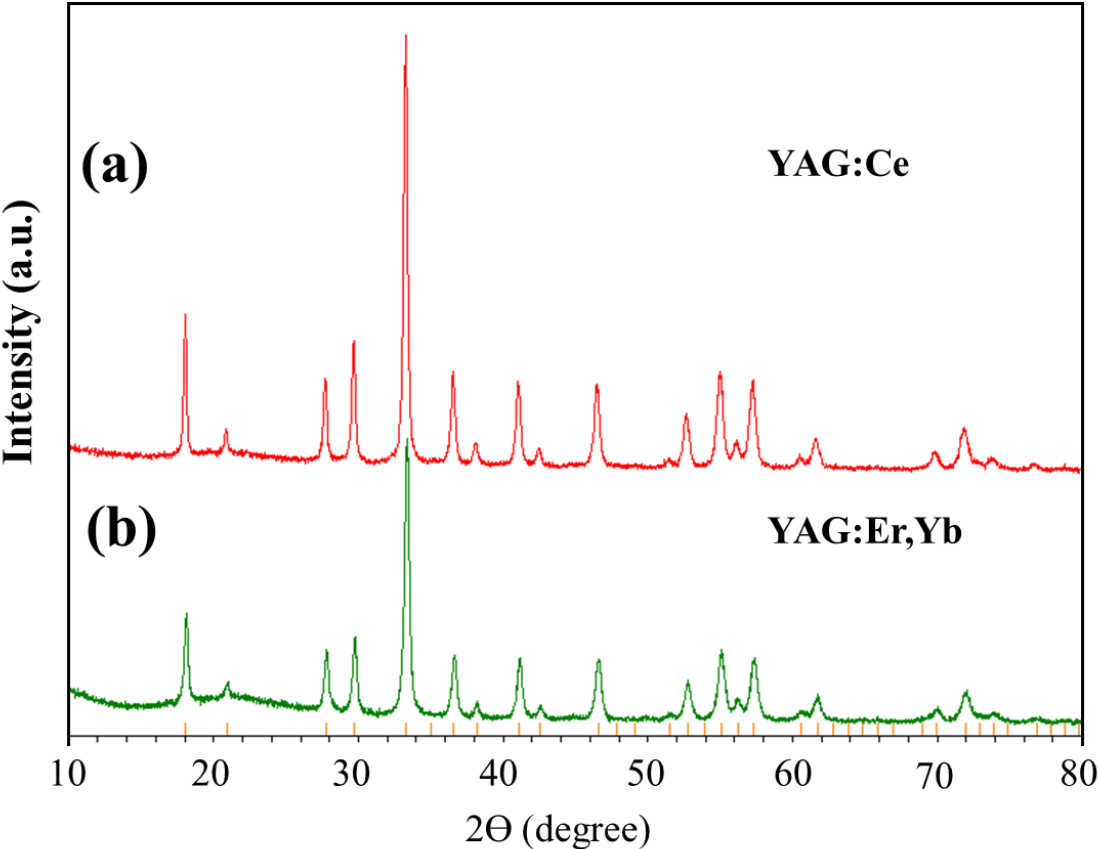


Figure 33. The XRD pattern of YAG:Ce and YAG:Er,Yb NPs

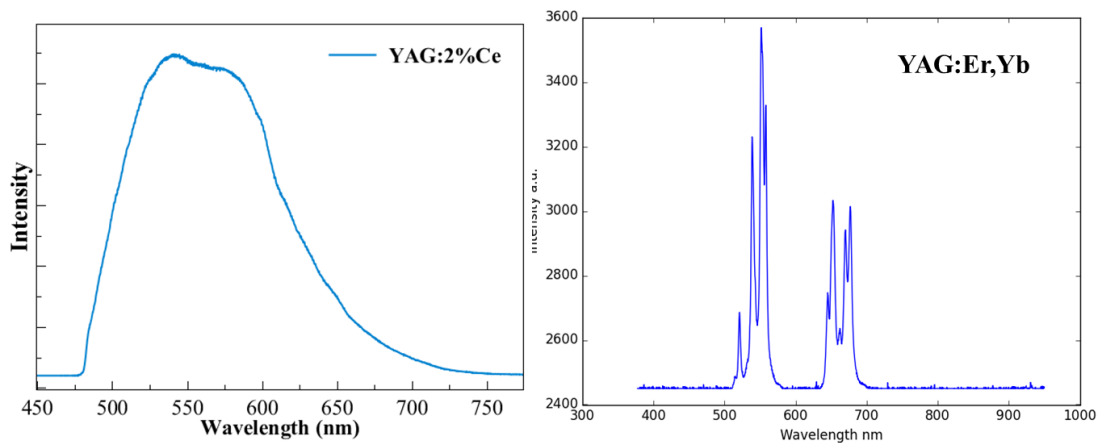


Figure 34. Emission spectra of YAG:Er,Yb NPs excited by 473 nm and 980 nm

The 4f-5d transition was applied in Ce^{3+} .¹⁴⁵⁻¹⁴⁹ The electrons at the 4f ground state were excited to the 5d state via 473 nm wavelength excitation, and relaxed to the lowest 5d band followed by transfer back to the 4f ground state ($^2\text{F}_{7/2}$ and $^2\text{F}_{5/2}$ states) shown in Figure 35. This is a down-shifting luminescence process. Not like the 5d-4f electron transition of Ce^{3+} , the 4f-4f transition was applied in Er^{3+} . The diagrams of energy level of Yb^{3+} and Er^{3+} ions¹⁵⁰ and the possible mechanism of upconversion luminescence are shown in Figure 36.^{27,151,152} The energy states are attributed to the spin-orbit interactions. The Yb^{3+} ions are excited to $^2\text{F}_{5/2}$ energy state, once they absorb a 980 nm photon. When the excited electron goes down to the $^4\text{I}_{15/2}$ state, the emission energy is transferred to the Er^{3+} ions. Er^{3+} ions are excited to $^4\text{F}_{7/2}$ and $^4\text{F}_{9/2}$ states, according to the mechanisms of excited state absorption (ESA) and energy transfer upconversion (ETU). The blue dash arrows represent the process of cross-relaxations. The excited states $^2\text{H}_{11/2}$, $^4\text{S}_{3/2}$, $^4\text{I}_{13/2}$ and $^4\text{F}_{9/2}$ are settled with nonradioactive de-

excitation and cross-relaxations. When the electrons drop from excited states to the ground state, the Er^{3+} ions are emitting the energy in red and green range.

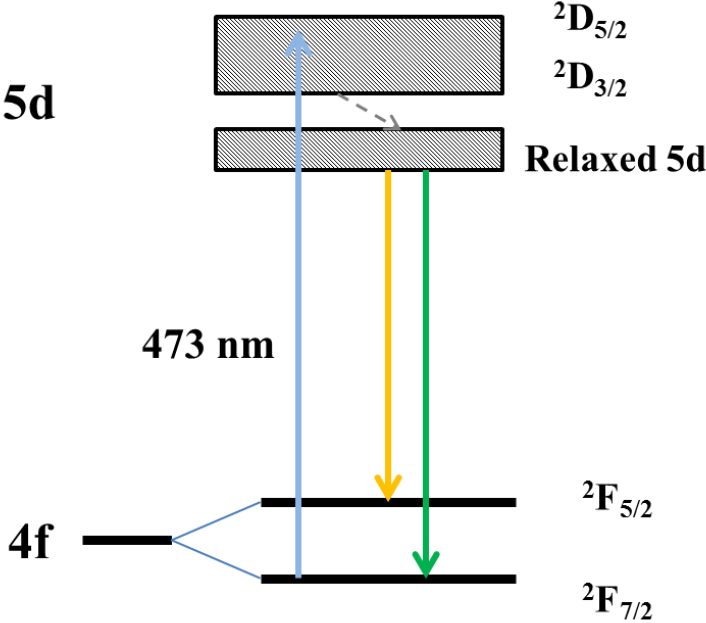


Figure 35. Energy diagram of Ce^{3+} in YAG:Ce

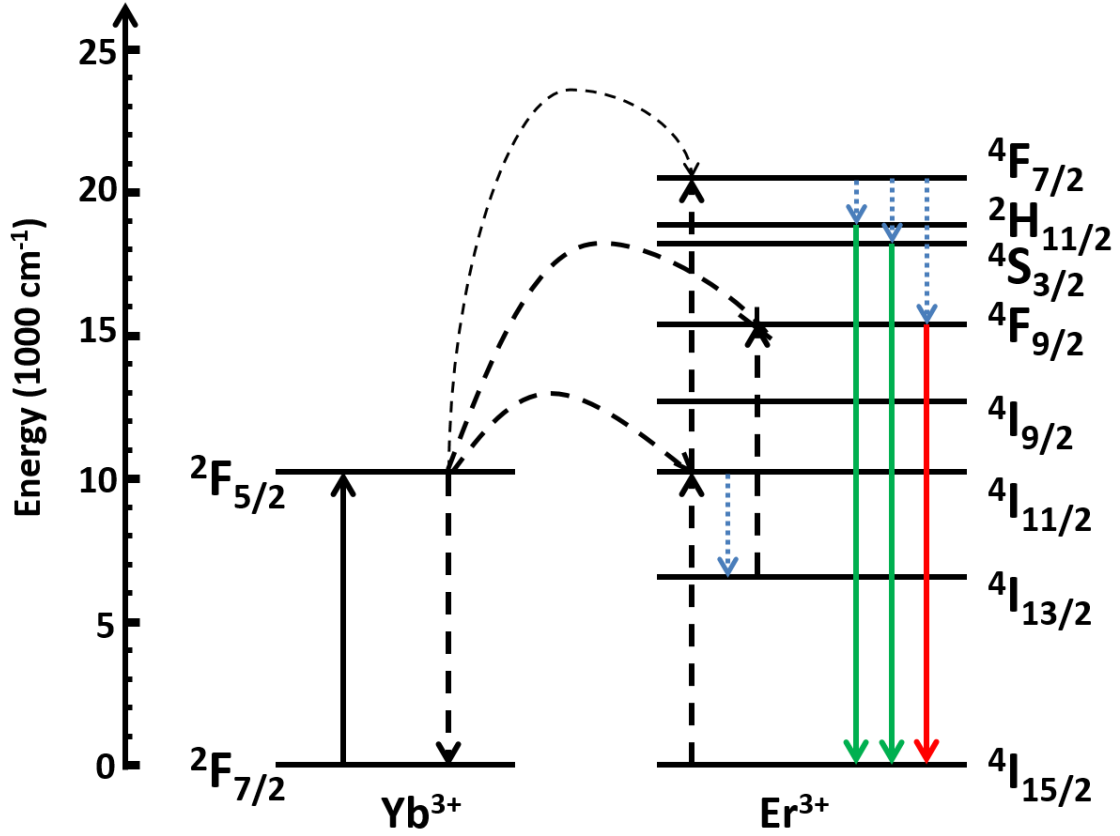


Figure 36. Energy level diagrams of Er³⁺ and Yb³⁺ ions, and proposed upconversion mechanisms^{27,151,152}

The emission from stark levels of $^4S_{3/2}$ to $^4I_{15/2}$ was observed based on the Raman measurement (HORIBA, iHR550) with grating of 2400 gr/mm and 532 nm laser excitation (Figure 37). Dammak *et al.* reported these emission peaks are attributed to the ions at three symmetry C_2 sites in yttria crystal¹⁵³. They calculated the $^4S_{3/2}$ level had two stark levels (U_1 and U_2) and $^4I_{15/2}$ had eight sublevels (Z_1 - Z_8). Table 5 shows our emission peaks compared with the report of Chandra *et al.*¹⁵⁴. Based on the table, it is clear to see these peaks were related to the crystal field splitting instead of spin-orbit interactions.

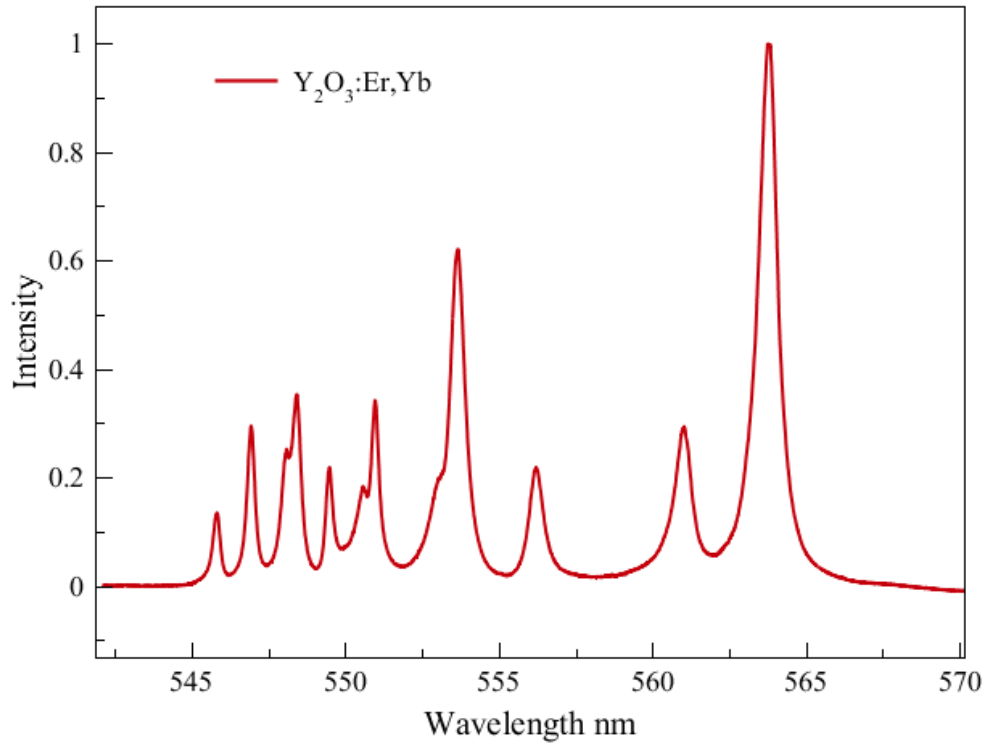


Figure 37. Emission spectrum of Y₂O₃:Er,Yb in order to observe the stark sub-levels.

Table 5. Comparison the energy transition of ⁴S_{3/2} sublevels for Y₂O₃:Er,Yb at room temperature.

Our Data (nm)	Relative Intensity	Compared Data (nm)	Compared Relative Intensity	Transition
554.8	0.13	545.71	0.11	U ₂ -Z ₁
546.92	0.29	546.83	0.23	U ₂ -Z ₂
548.1	0.25	547.96	0.18	U ₂ -Z ₃
548.38	0.35	548.32	0.27	U ₂ -Z ₄
549.35	0.22	549.38	0.18	U ₁ -Z ₂
550.58	0.18	550.49	0.15	U ₁ -Z ₃
550.96	0.34	550.87	0.27	U ₁ -Z ₄
553.63	0.62	553.55	0.47	U ₁ -Z ₅
556.19	0.21	556.15	0.19	U ₁ -Z ₆
561.01	0.29	560.96	0.29	U ₁ -Z ₇
563.77	0.99	563.73	0.99	U ₁ -Z ₈

4.2. Alternative host lattices

With alternative host lattices, the performance of RE-doped NPs can be modified as well, which is owing to the crystal split field. As the dopants are the same, the electron transition in energy states of dopant element are similar. However, with alternative host lattices, the dopants are affected by the site symmetry and ion-ligand distance. This will result in the different splits of energy sublevels and altered emission spectra. In this study, we used same dopants but alternative host lattices. They are $\text{YAG:Er}^{3+}, \text{Yb}^{3+}$. and $\text{Y}_2\text{O}_3:\text{Er}^{3+}, \text{Yb}^{3+}$.

The emission spectra were obtained by using the home-made confocal laser scanning microscope. With the alternative host lattice, the emission spectra were different, though both were excited by the same 980 nm laser. The upper spectrum represents the $\text{Y}_2\text{O}_3:\text{Er}^{3+}, \text{Yb}^{3+}$, and the lower one is $\text{YAG:Er}^{3+}, \text{Yb}^{3+}$ (Figure 38). This difference is driven by the crystal field. The circle marked peaks are attributed to the typical spin-orbit interaction. The differences in emission peaks were observed (marked in line). This is caused by the crystal field and the doping site of host lattice.

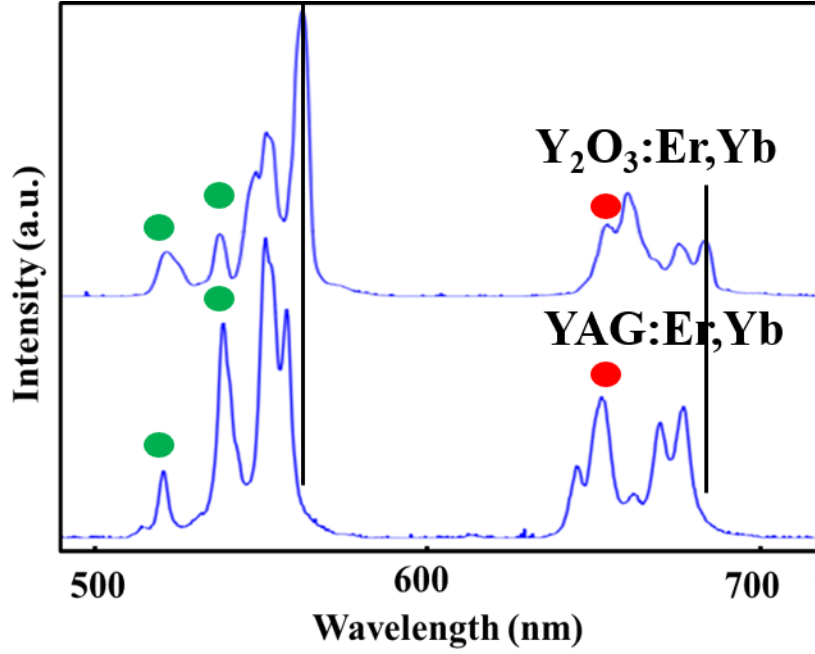


Figure 38. Emission spectra of $\text{Y}_2\text{O}_3:\text{Er}^{3+}, \text{Yb}^{3+}$ (upper), and $\text{YAG}:\text{Er}^{3+}, \text{Yb}^{3+}$ (lower).

Based on energy level of free Er^{3+} ions, two 548nm and 528nm green peaks were depended on the non-radiation transitions from ${}^2H_{11/2}$ and ${}^4S_{3/2,4}$ to ${}^4I_{15/2}$ ground states. Other peaks were based on Crystal field split. The Hamiltonian operator of crystal field part is defined as equation (6)^{155,156}

$$H_{CF} = \sum_{k,q,i} B_q^k C_q^{(k)}(i) \quad (6)$$

where B_q^k are Wybourne crystal-field parameters, which are related to site symmetry and ion-ligand distance. The $C_q^{(k)}$ are the spherical tensor operators. The Wybourne parameters are expressed as equation (7)

$$B_q^k = \sum_l \bar{B}_k(R_l) g_{k,q}(\theta_l, \phi_l) \quad (7)$$

where $\overline{B}_k(R_i)$ are denoted as intrinsic crystal field parameters which are related to a repulsive interaction with the open-shell electrons. The parameters $g_{k,q}(\theta_l, \phi_l)$ are referred as coordination factors. Therefore, B_q^k are dependence on the distance and orientation of the coordinated ligands.

The spherical tensor operators are dependence of the form as equation (8)

$$C_q^{(k)}(i) = \left(\frac{4\pi}{2k+1}\right)^{1/2} Y_{km}(\theta_i, \phi_i) \quad (8)$$

where $Y_{km}(\theta_i, \phi_i)$ are ordinary spherical harmonic parameters. Therefore, the host lattice does affect the crystal-field split greatly, as the doping site of rare earth elements have alternative symmetry and orientation of the coordinated ligands.

Based on the equations, we know the symmetry of doping sites and ligand distance play an important role in modifying the optical properties. Considering the dopants in the host lattices, we can observed the differences of symmetry and ligand distance between YAG:Er,Yb and Y₂O₃:Er,Yb, shown in Figure 39. In Y₂O₃ host lattice, the RE ion is doped in a non-centrosymmetric YO₆ site with 6 oxygen atoms at its neighbors. The distance between Y and O atoms is 2.266 and 2.368 Å. Compared with YAG lattice, RE ion is doped in a YO₈ site with 8 oxygen atoms at its neighbors. The distance is 2.433 and 2.303 Å. Therefore, the symmetry of the doping sites are different, which lead to the altered emission peaks observed in Figure 38.

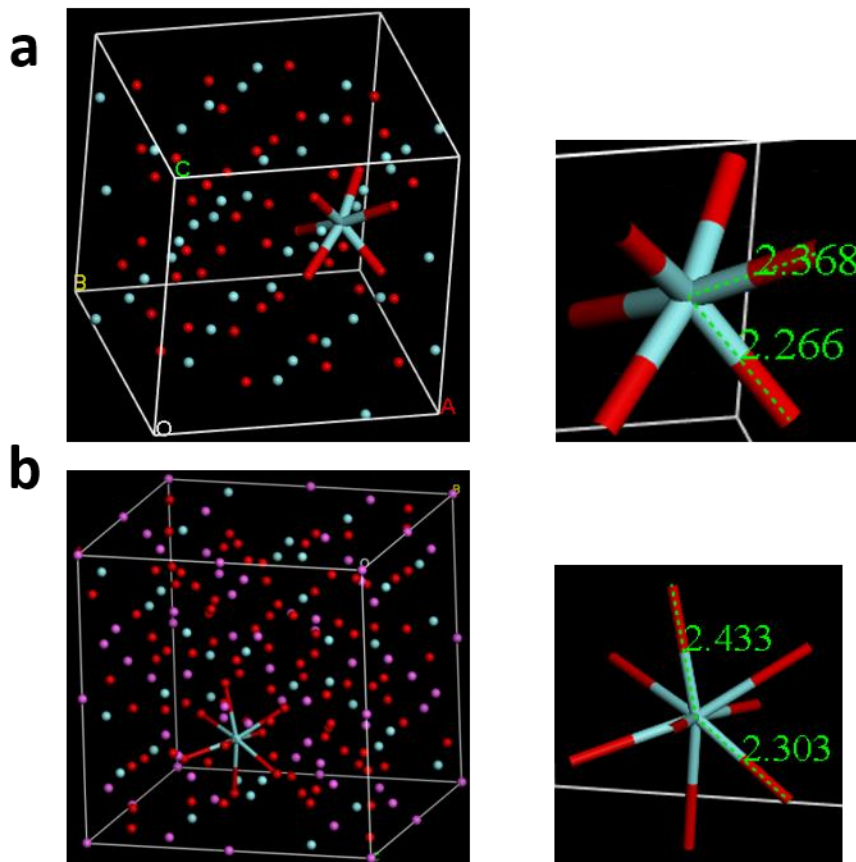


Figure 39. The crystal structures and the non-centrosymmetric doping sites of (a) Y_2O_3 and (b) YAG for RE ions. The crystallographic information file was obtained from Inorganic Crystal Structure Database.

4.3. Introducing defects

4.3.1. Upconversion performance of $Y_2O_3:Er,Yb$ by introducing metal ions

The upconversion (UC) emission spectra of $Y_2O_3:Er,Yb$ NPs were tested by using the home-made spectrometer. Figure 40 shows the UC emission spectra of Er^{3+} and Yb^{3+} doped $Y_2O_3:Er,Yb$ NPs which were tested at room temperature. With the excitation of the 980 nm laser, the emission spectra were located at red and green bands, which were around 520-570 nm and 630-670 nm. The red and green bands centered at 650 nm and 550 nm respectively, which were derived from the intra 4f configuration

transitions of Er^{3+} . The red emission was generated when the electron transported from $^4\text{F}_{9/2}$ state to $^4\text{I}_{15/2}$ state, and the green emission was got when it went from $^2\text{H}_{11/2}/^4\text{S}_{3/2}$ to $^4\text{I}_{15/2}$ state. However, the red to green ratio in the emission spectra has a clear change, which is attributed to the different concentration of Mg ions introduced during reaction. It could be the defects introduced into the host crystal lattice by adding the Mg^{2+} ions, which lead to the distortion of host lattice.

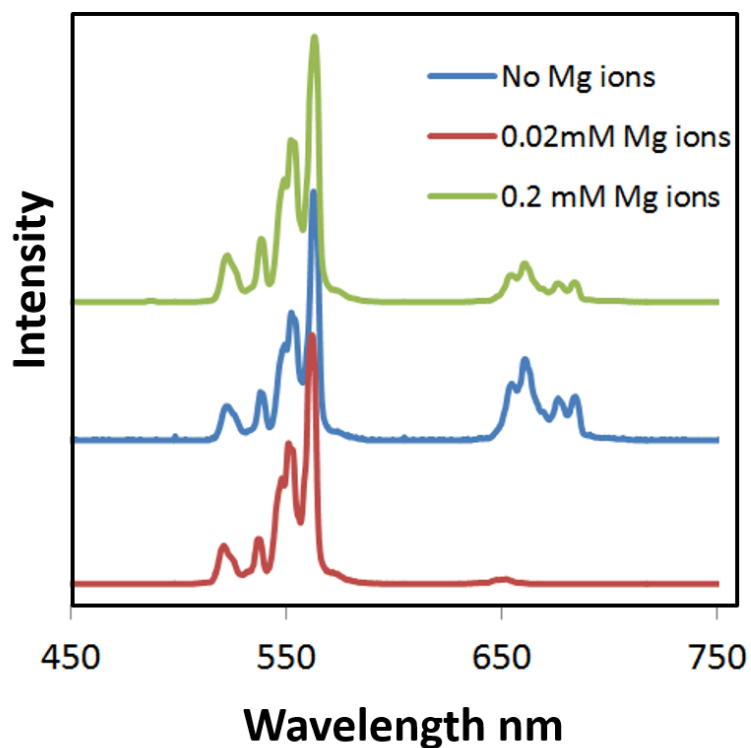


Figure 40. Upconversion emission spectra of $\text{Y}_2\text{O}_3:\text{Er},\text{Yb}$ under the excitation of a 980nm diode laser.

4.3.2. Down-shifting performance of YAG:Ce³⁺ by hydrogenation

In order to modify the optical properties of NPs, the most commonly used methods to introduce defect are annealing at different temperature¹⁵⁷ and doping with ions at altered concentration¹⁵⁸. In our study, we introduced metal ions during the synthesis of Y₂O₃:Er,Yb, the emission ratio of green to red was changed. No shift in emission spectra was observed, because the emission transition in Y₂O₃:Er,Yb is 4f-4f transition. The 4f orbit is protected by 5s and 5p electron orbits. Besides introducing metal ions, we used hydrogen treated YAG:Ce NPs. A red-shift was observed in the emission spectra, as 5d-4f emission transition has no outer electron shell protection. The change of green to red ratio and the red-shift should be caused by introducing the defects.

Based on the literature view, the band gap of TiO₂ was reduced from 3.3 eV to 2.18 eV by using hydrogenation.¹⁵⁹ Considering the effects of interstitial hydrogen (H) atom, we used CASTEP (Material studio) to calculate the band gap of YAG with and without interstitial H atom based on the first principle method. We found that the band gap was reduced from 4.5 eV to 2.5 eV after introducing the interstitial H atom (Figure 41). Therefore, we assume the hydrogenation would change the optical performance of YAG:Ce as well.

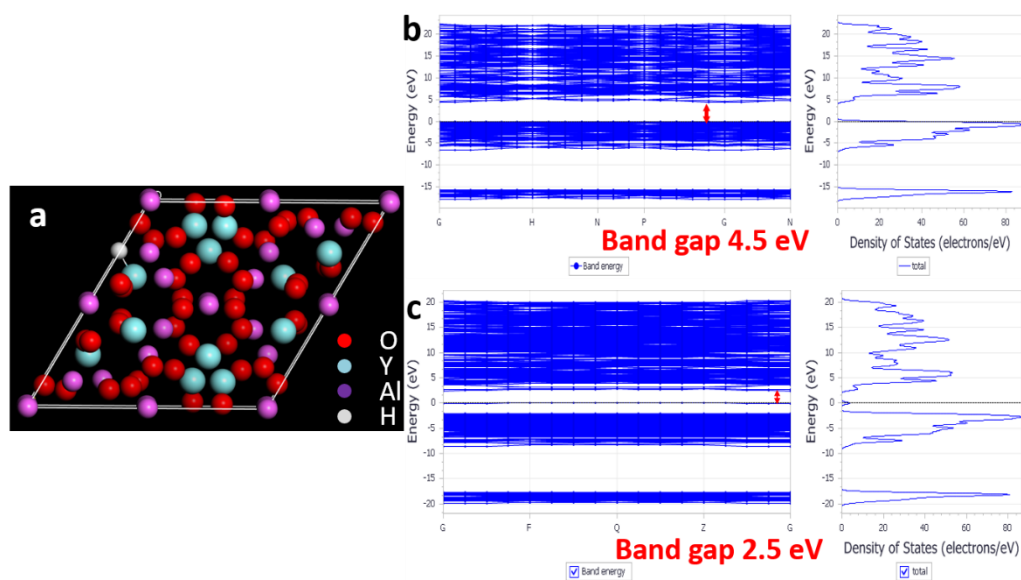


Figure 41. (a) The crystal model of YAG with interstitial H atom. The band structure and density of states of (b) YAG and (c) YAG with interstitial atom.

We did hydrogen treatment of YAG:Ce at 1000 °C and observed the emission spectra by using the home-made scanning confocal microscopy. Upon 473 nm laser diode excitation, a green-yellow region emission peak was observed (Figure 42). A Stokes shift, absorbing higher photon energy and emitting lower photon energy, was processed. It is clear to see that 2 mol% doped samples have a slight red-shift with hydrogenation. In addition, with longer hydrogen treatment, the red-shift became tiny further. For the 6 mol% doped samples, a clear red-shift was observed. However, there is no clear change with longer hydrogen treatment. Furthermore, the emission peak can be deconvoluted as a sum of two Gaussian curves (Figure 43). The center positions of Gaussian curves were shown in Table 6. For the 2 mol% NPs, Gaussian curve 1 center has a slight shift with hydrogenation, from 575 nm to 578 nm (1 hour treatment) and 580 nm (48 hours treatment); meanwhile, the Gaussian curve 2 centers almost keep the same

location. For the 2 mol% NPs, a 9 nm red-shift was observed for the Gaussian curve 1 from 578 nm to 587 nm, and a 5 nm red-shift was detected from 524 nm to 529 nm. Based on the Gaussian curve fitting of YAG:6%Ce, the curve 1 centered at 578 nm is attributed to the electrons of Ce^{3+} transfer to (${}^2\text{F}_{5/2}$), and curve 2 centered at 524 nm is corresponding to the transfer to (${}^2\text{F}_{7/2}$). The difference between curve 1 and curve 2 are listed in the Table 6, which is close to the conclusion that the gap between ${}^2\text{F}_{5/2}$ and ${}^2\text{F}_{7/2}$ is around 2000 cm^{-1} .^{160,161} In addition, the Gaussian curve fitting has no change between 1 hour and 48 hours hydrogen treatment.

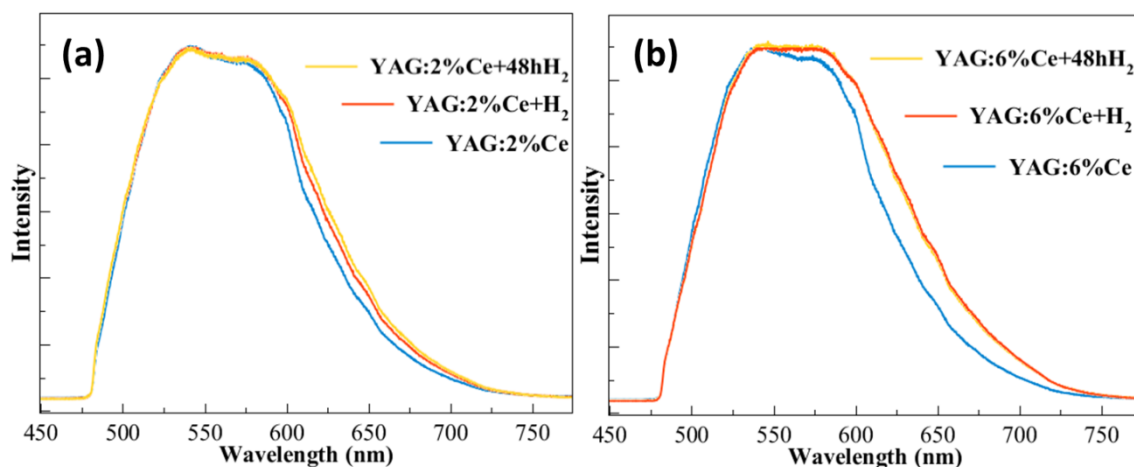


Figure 42. Photoluminescence spectra of (a) YAG:2% Ce^{3+} and (b) YAG:6% Ce^{3+} with and without hydrogen treatment

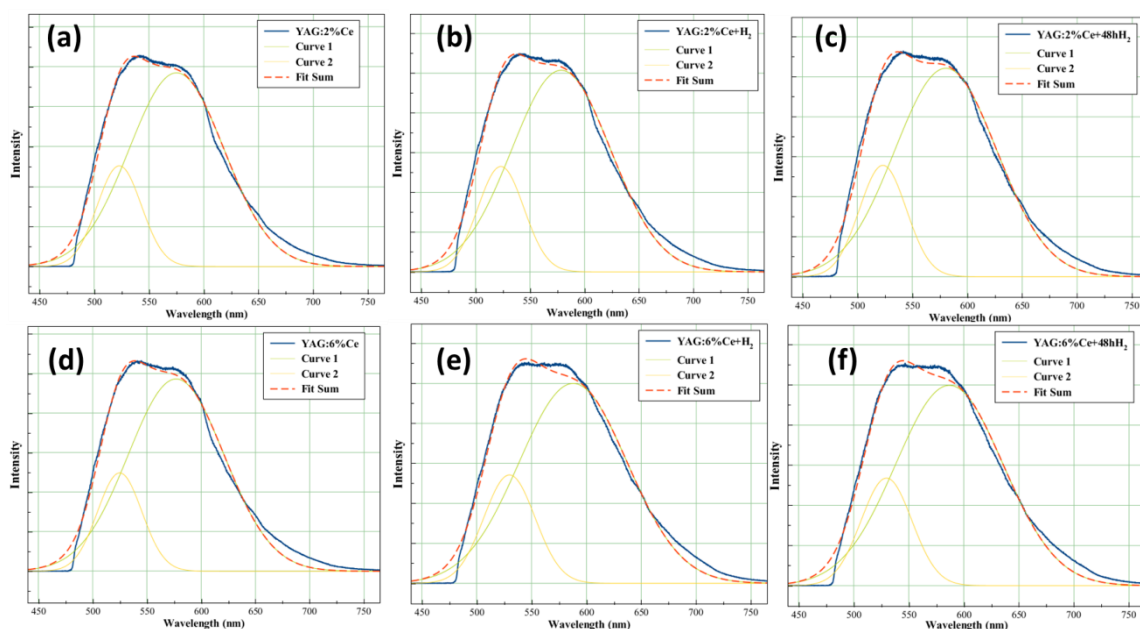


Figure 43. Gaussian curve fittings for emission spectra of (a) YAG:2%Ce, (b) YAG:2%Ce+H₂, (c) YAG:2%Ce+48hH₂, (d) YAG:6%Ce, (e) YAG:6%Ce+H₂, and (f) YAG:6%Ce+48hH₂ samples.

Table 6. Table of two Gaussian curve peak centers and their difference.

SAMPLES	GAUSSIAN FIT PEAK CENTER			DIFFERENCE
		(nm)	(cm ⁻¹)	(cm ⁻¹)
YAG:2%Ce	Curve 2	522	19157.08812	1765.78377
	Curve 1	575	17391.30435	
YAG:2%Ce+H ₂	Curve 2	523	19120.45889	1819.42083
	Curve 1	578	17301.03806	
YAG:2%Ce+48hH ₂	Curve 2	523	19120.45889	1879.07958
	Curve 1	580	17241.37931	
YAG:6%Ce	Curve 2	524	19083.96947	1782.93141
	Curve 1	578	17301.03806	
YAG:6%Ce+H ₂	Curve 2	529	18903.59168	1867.81655
	Curve 1	587	17035.77513	
YAG:6%Ce+48hH ₂	Curve 2	529	18903.59168	1867.81655
	Curve 1	587	17035.77513	

The red-shift could be caused by the nephelauxetic effects, which literally means the expansion of the charge cloud.^{162,163} By introducing the H atom into host lattice, the distance between Ce³⁺ and O²⁻ became shorter. The crystal field splitting (Dq) can be expressed as equation (9)¹⁶⁴

$$Dq = \frac{1}{6} Ze^2 \frac{r^4}{R^5} \quad (9)$$

where Dq related to the energy states separation, Z is the anion charge, e is the electron charge, R is the bond length and r is the radius of the d wavefunction. Once distance between Ce³⁺ and O²⁻ became shorter, the crystal field splitting of 5d was increasing (Figure 44). Therefore, a red-shift was obtained.

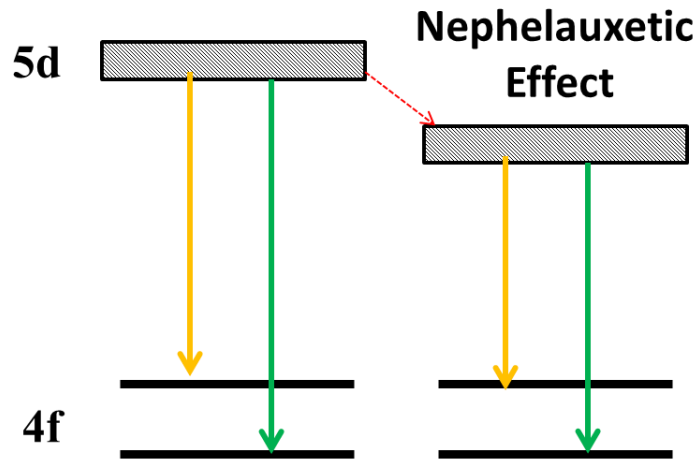


Figure 44. Nephelauxetic effect on Ce³⁺

4.4. Summary

In this chapter, the modification of emission performance of RE-doped NPs is discussed. Three potential methods and their mechanisms were discussed (Figure 45).

First, we used different rare earth elements to dope in the same YAG host lattice. Even

though the XRD patterns showed the same crystalline structures, the emission performance indicated variation due to the altered energy levels of lanthanide ions. Furthermore the discussion was about using different host lattice but the same dopants. Based on the effects of different symmetric sites and ligand distance, the emission performance can be modified by using alternative host lattices. In the last section, by introducing defects, we modified the optical performance of RE-doped NPs. We proposed three possible reasons, they are distortion of host lattices, nephelauxetic effect and changes of band gap.

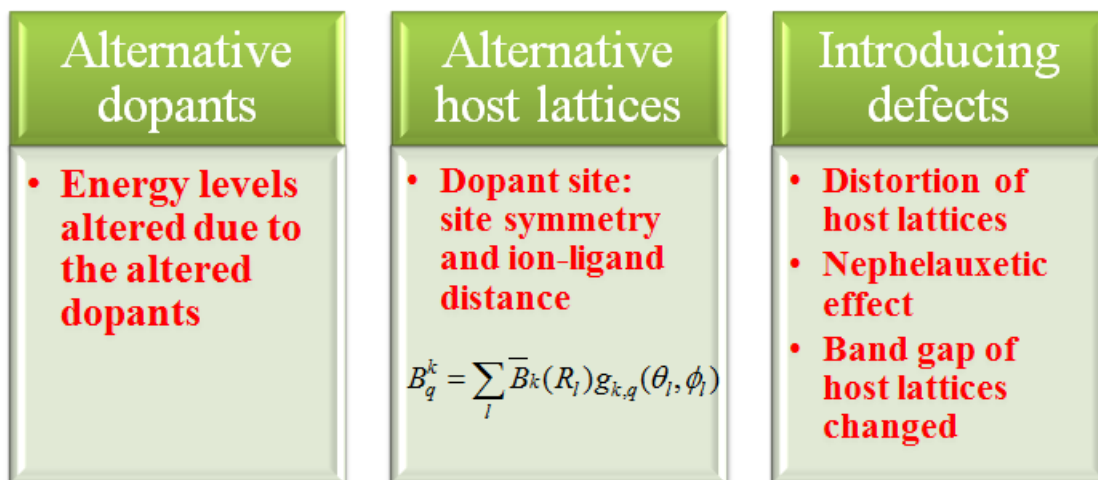


Figure 45. Three potential methods to modify the optical performance of RE-doped NPs and their mechanisms.

CHAPTER V

IN SITU* DETECTING NANOPARTICLES IN BIOLOGICAL SYSTEM

This chapter discusses the application of as-synthesized rare-earth-doped nanoparticles in biological systems. It includes three sections. The first and second sections discuss the effects of $\text{Y}_2\text{O}_3:\text{Er}^{3+}, \text{Yb}^{3+}$ UCNPs on insects: the fire ants and mealworm. The third imaging techniques will be compared in first section. The third section observes the absorption of $\text{Y}_2\text{O}_3:\text{Er}^{3+}, \text{Yb}^{3+}$ UCNPs in young cabbage.

5.1. Probing of yttria NPs in fire ants (*Solenopsis xyloni*)

In the present research, southern fire ants (*Solenopsis xyloni*, Formicidae) were selected due to their importance in agriculture. To date, there was no alternative to effectively eliminate them from critical areas. Imaging upconversion nanoparticles could be included as a method to understand fire ants by study their habits and interactions. This would help for future work to find effective ways to definitively control such nuisance.^{165,166} The primary goal of this experiment was to obtain high-contrast images

*Part of this chapter reproduced with permission from “Observation of yttrium oxide nanoparticles in cabbage (*Brassica oleracea*) through dual energy K-edge subtraction imaging” by Yunyun Chen, et al., *Journal of nanobiotechnology*, **2016**, 14:23 (© Chen et al. 2016); and “Observation of two-dimensional yttrium oxide nanoparticles in mealworm beetles (*Tenebrio molitor*)” by Yunyun Chen, et al., *J. Synchrotron Rad.*, **2016**, 23, 1197-1201, <http://dx.doi.org/10.1107/S1600577516009942> (Copyright © 2016, International Union of Crystallography); and “High resolution fluorescence bio-imaging upconversion nanoparticles in insects” by Masfer Alkahtani, Yunyun Chen et al., *Optics Express*, **2017**, 25, 1030-1039 (Copyright © 2017, Optical Society of America).

of $\text{Y}_2\text{O}_3:\text{Er}^{3+}, \text{Yb}^{3+}$ upconversion nanoparticles as bio-probe inside fire ants using economical and homemade optical system. From a colony of agriculturally damaging southern fire ants (*Solenopsis xyloni*) kept at room temperature (25 °C) and in a 12:12 h Light:Dark cycle, in the Entomology Laboratory, at California State University, Fresno, CA, individuals were extracted for experimentation. Isolated southern fire ants were placed in polystyrene boxes with sides covered with fluon to avoid their scape. In a first test, one group of southern fire ants was fed with a 10% honey-water + NPs solution at libitum, while a control group was fed only with 10% honey-water. Since fire ants are recognized carnivorous insects, while contained in polystyrene boxes with fluon covered sides, another group was fed with mealworms previously fed with 10% Honey-water + NPs and positively tested for internal presence of NPs¹⁶⁷, while a control group of southern fire ants was fed with mealworms fed with 10% honey-water only. Microtomography imaging failed to detect NPs inside the digestive track and the coelom of the tested individuals fed with NPs in the 10% Honey-water diet.

5.1.1. Two-dimensional confocal optical imaging

A Confocal setup was used for this experiment with 10x microscope NIR, NA=0.26 mitutoyo corrected objective (Figure 19). Figure 46 shows the X-Y scanning of ant by photon counter with a resolution of 1.6 μm in X and Y directions. Near infrared laser (980 nm) was used for excitation of upconversion NPs fed into the ants with laser intensity of $12\text{kW}\cdot\text{cm}^{-2}$ and spot size of 3.98 μm . Our biological samples in this experiment, fire ants, didn't show any damages or burning on their bodies after scanning with this specific laser power. Green illumination was used to compare

between background fluorescence out of the samples. It is clear that there is no background fluorescence by using the infrared laser excitation. Figure 47 shows the emission spectra of three fluorescence spots in Figure 46. Upconversion NPs are very bright and stable with long exposure time staying inside the ants. Figs. 5(a, inset) and 5(b, inset) presents a strong and clear upconversion luminescence (UCL) spectra of $Y_2O_3: Er^{+3}, Yb^{+3}$ UCNPs in which the emission bands reveal strong green luminescence emission and weak red emission spectra corresponding to the erbium (Er^{+3}) radiative transitions from ($^2H_{11/2}$, $^4S_{3/2}$, and $^4F_{9/2}$) excited states to $^4I_{15/2}$ ground state. Furthermore, the ratio of red to green is changed at different fluorescence spots. This could be attributed to the energy transferred from UCNPs to the tissue of ants through a nonradioactive dipole-dipole coupling. However, with the 2D imaging, it is difficult to distinguish the location of UCNPs-inside or outside the body of ants. In order to solve this issue, we rotate and scan the samples in 360° to generate a 3D tomographic imaging.

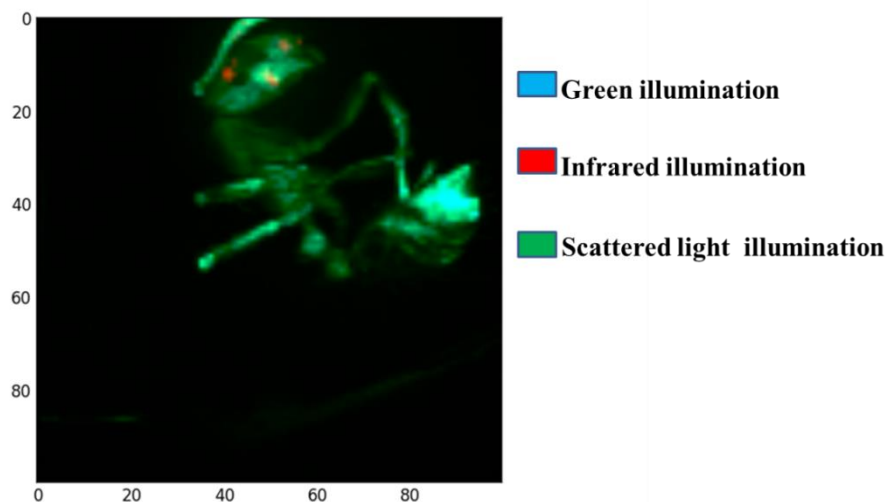


Figure 46. X-Y scanning of ant by photon counter

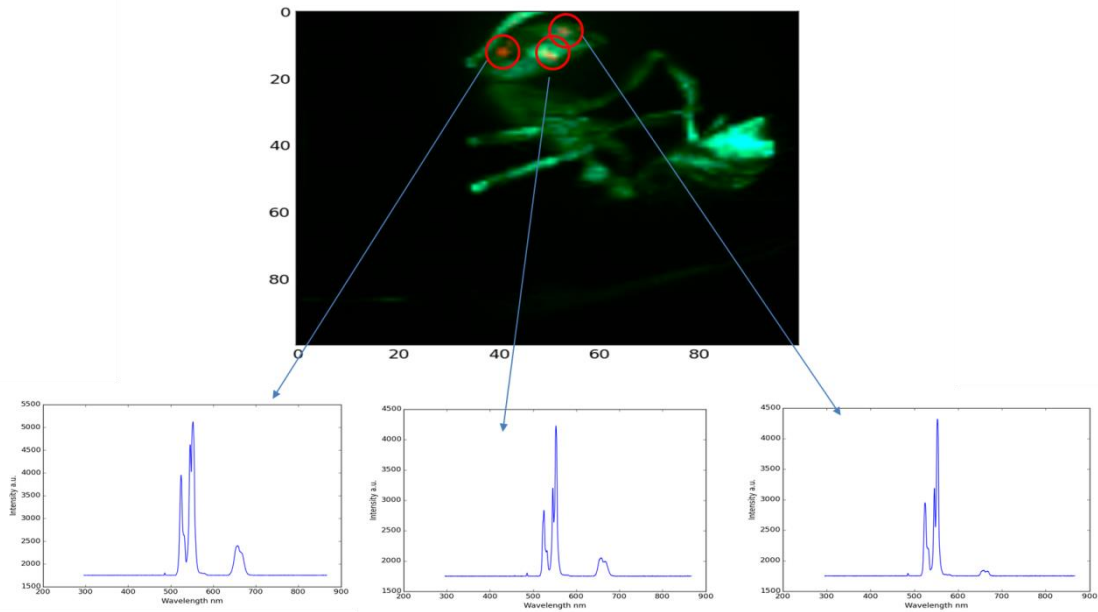


Figure 47. Emission spectra of fluorescence spots in ant

5.1.2. Visual Light Tomography

In order to reconstruct the 2D projection images into cross-section images, lightct and scikit-image packages of python were applied by using filtered back projection algorithm. This algorithm is a common used method for CT reconstruction employing Radon transform and Fourier slice theorem. The first step is to obtain the 2D projective imaging dataset with 360 degree rotation of specimen, followed by centering the 2D projection image datasets (Figure 48). This ant was injected with UCNPs at abdomen. The centered image datasets will be calculated with filtered back projection algorithm. The reconstructed 2D transverse image slices of the sample can be obtained. With the plugin function of volume view in ImageJ, the 2D transverse slices can be stacked into 3D (Figure 49).

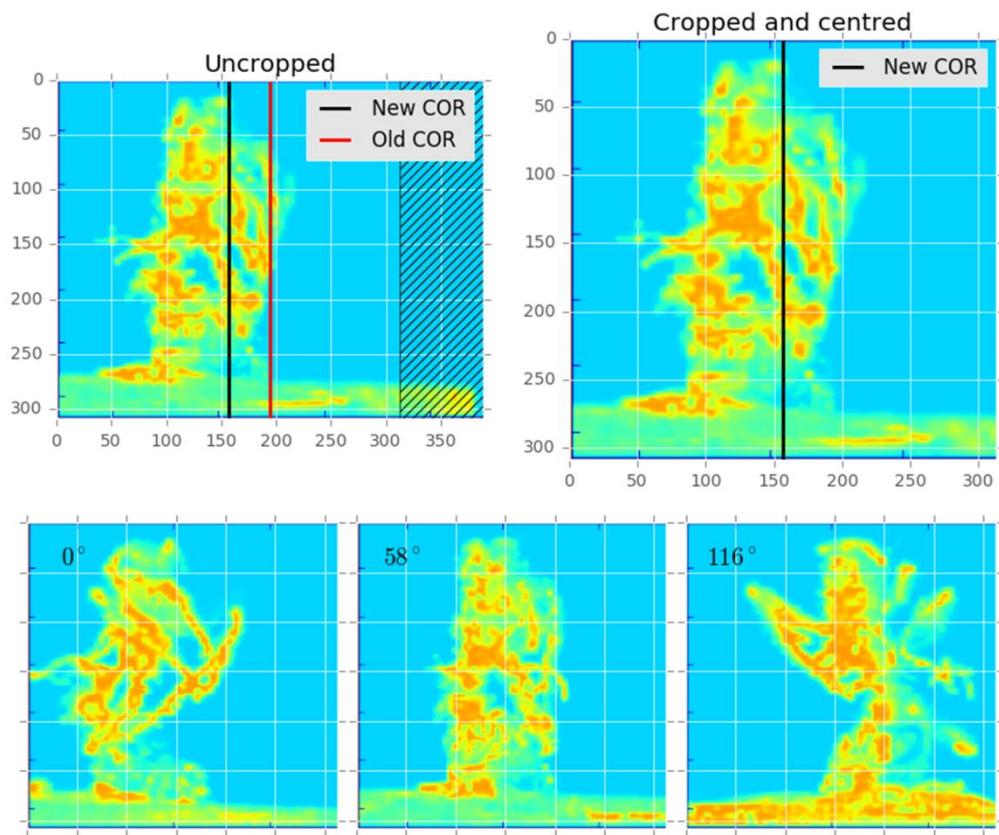


Figure 48. Centered projective image of ant sample excited by 532 nm.

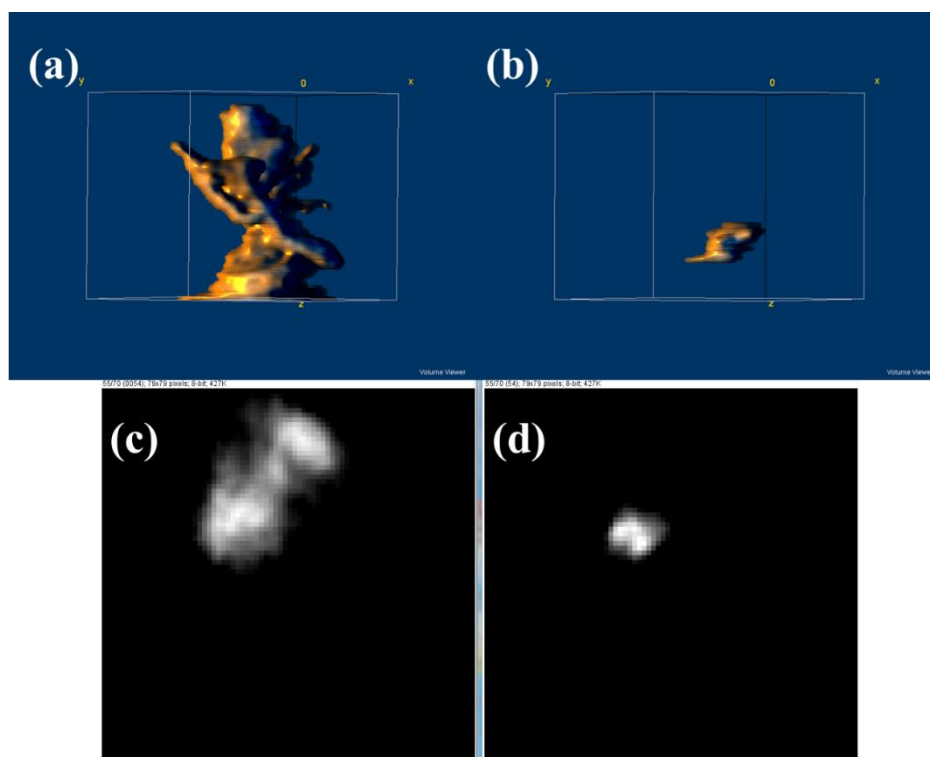


Figure 49. 3D visualization of ant excited by 532 nm laser and (b) 980 nm NIR laser.

However, the disadvantage is that the low transmission of emission light emitted by the UCNPs. In this research, we use ants as specimen, which is small so that the light can penetrate. Once the sample is large, such as mealworm, this visual light tomography is not that practical. Therefore, the X-ray tomography will be a great solution.

5.1.3. Synchrotron Micro-tomography with Dual-energy K-edge subtraction

In order to identify the localization and distribution of $Y_2O_3:Er^{+3},Yb^{+3}$ NPs, the K-edge subtraction technique (KES) is used. Details about this technique have been reported in our previous work^{167,168} and discussed in chapter 5.3.2. The yttrium K-edge is at 17 keV, meaning that it shows a significant increase in attenuation coefficient when moving the scan energy from 16.7 to 17.3 keV (Figure 50a,b). By subtracting the two

images (17.3 – 16.7 keV), the $\text{Y}_2\text{O}_3:\text{Er}^{3+}, \text{Yb}^{3+}$ NPs and their localization can be identified (Figure 50c).

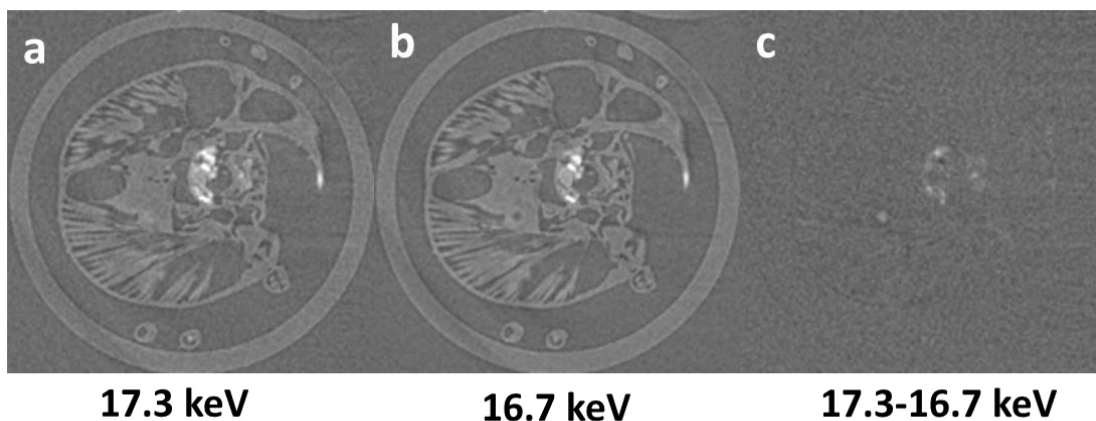


Figure 50. The slice obtained by scanning at (a) 17.3 keV and (b) 16.7 keV. (c) The subtracted slice to identify and localize the $\text{Y}_2\text{O}_3:\text{Er}^{3+}, \text{Yb}^{3+}$ NPs

The locations of the upconversion nanoparticles inside the fire ants' body were confirmed by performing three dimensional X-ray imaging. The distribution of lanthanide-doped yttrium ($\text{Y}_2\text{O}_3:\text{Er}^{3+}, \text{Yb}^{3+}$ nanoparticles) within buccal cavity and anterior end of the digestive tract of the ant were segmented and marked in red as shown in Figure 51. After achieving high contrast images of the UCNPs inside fire ants using an optical system, it was necessary to confirm that the nanoparticles are actually inside the body of the fire ants. Two fire ants from the same colony of southern fire ants were extracted and scanned using synchrotron radiation micro X-ray computed tomography (SR- μ XCT). Micro-tomography imaging failed to detect NPs inside the digestive track and the coelom of the tested individuals fed with NPs in the 10% Honey-water diet. However, NPs could be clearly seen within the buccal cavity (Figure 51). As previous research on social ants seems to suggest ¹⁶⁹hygiene and grooming behavior of fire ants

might help to isolate foreign objects from their food not allowing them to be ingested which might explain that no NPs were found in other regions of the digestive system, except for the mouth. If we had been able to find NPs inside the coelom or other parts of the body, we would have expected them to be encapsulated by hemocytes as previous experiences indicate^{167,170}.

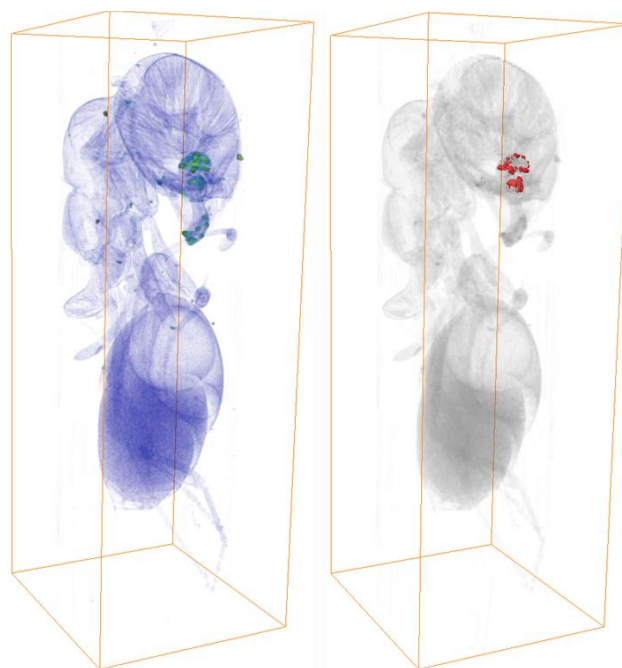


Figure 51. Three dimensional X-ray imaging of UCNPs inside fire ant. The box size of (c) is 1.15 x 1.09 x 3.08 mm

5.1.4. Comparison of three imaging techniques

Firstly, two-dimensional optical imaging is obtained using a home-made confocal scanning microscopy. The NIR excitation of UCNPs is used to avoid the background fluorescence. Secondly, `lightct` and `scikit-image` packages of python are applied to calculate and reconstruct the project images into cross-section images. The visual light tomography is applied to build the 3D visualization. Thirdly, synchrotron

micro-tomography combined with K-edge technique is employed to identify the target element. The advantages and disadvantages of three techniques are listed in Table 7. Using these imaging techniques, we will study the application of as-synthesized rare earth doped NPs in bio-imaging, which will be discussed in next chapter.

Table 7. The advantages and disadvantages of three techniques.

	Advantages	Disadvantages
Confocal optical imaging	<ul style="list-style-type: none"> a. NIR excitation; b. High contrast c. Fast 	<ul style="list-style-type: none"> a. UCNPs location not clear; b. No whole body images
Visual light tomography	<ul style="list-style-type: none"> a. NIR excitation; b. High contrast; c. Whole body image; d. Clear UCNPs location e. Fast 	<ul style="list-style-type: none"> Only available for small samples to observe the UCNPs within the body
Synchrotron tomography with K-edge subtraction	<ul style="list-style-type: none"> a. Deep penetration; b. Whole body image; c. Clear NPs location; d. Available for relatively large samples; e. Calculate the concentration of NPs 	<ul style="list-style-type: none"> a. Relatively long time; b. Shrink of the tissue

5.2. Mealworms (*Tenebrio Molitor*)

We have used mealworm beetles (*Tenebrio molitor*; Coleoptera: Tenebrionidae) as a model system in this work because of their relatively large size and ease of rearing and handling^{171 172 173}. Yttria NPs were mixed with distilled water followed by mixing with Honey Water (10% Honey and 90% distilled water). *Tenebrio molitor* adults (mealworms) (Coleoptera: Tenebrionidae) had been reared inside polystyrene boxes with no lids, containing a medium that consisted of crushed wheat and oats, to which a couple of slices (~4 mm thick) of a medium-sized apple were added every two weeks. The boxes containing the beetles were kept in a regular day/night regime (in Fresno, California) at a controlled temperature of 25 °C and 60% Relative humidity. Individuals intended for experiments were selected randomly from fully pigmented beetles (>48 h old). Once the adult mealworms were taken from the general rearing culture to be tested, they were left with no food for 5 days in a 10 X 15 X 15 polystyrene box, with no lid and walls covered with fluon (liquid Teflon). On the 6th day, a fourth of the group (reference sample) was fed with Honey water (10% honey) and then taken out and fixed with Kahle's fixative (which allows for a good fixation of the internal tissues and organs of the insect). The remaining mealworms inside the experimental box were then provided with Honey water (10% honey) + NPs *ad libitum*. One fourth of the group was taken after 1 hour of feeding, another fourth after 12 hours, and the remaining group after 24 h. Each insect was fixed with Kahle's fixative upon extraction from the polystyrene box.

With the same KES method, we build the 3D visualization of mealworm samples. The translocation of NPs within mealworms is evident by comparing the 3D visualization of the insects that that experienced each of the four different NP feeding times (0, 1, 12, and 24 hrs) (Figure 52). To better understand how the nanoparticles aggregate and move inside the insect, we studied 2D digital slices through the reconstructed 3D volume, with contrast inverted so that NPs are in the darker (more black) regions (Figure 53). The reference sample shows no NPs or other highly X-ray attenuating features. For mealworms that fed on NPs, the NPs can be observed moving from the mouthparts (head) to the abdomen (Figure 52). After 1 hr, we can clearly see that the NPs were mainly located passing the mouthparts inside the head and into the foregut (Figure 52 and Figure 53a). Figure 53b shows that the NPs were swallowed into the buccal cavity (black mark) and flowed into the pharynx (red). The transverse slice shows the NPs located at the pharynx (Figure 53c red). After passing the pharynx, the NPs moved to the oesophagus (Figure 53d purple).

After 12 hrs, even though the NPs can be seen at the head (mealworms were feeding *Ad libitum*), they are additionally moving through the digestive system and can be seen in the thorax and entering the abdomen (Figure 52). Figure 53e presents the 12 h fed sample with NPs accumulated in the thoracic region. The NPs were passing through but accumulated along the walls of the pharynx and the oesophagus. Passing the oesophagus, the NPs went into the crop, as marked by the yellow circles in Figure 53f&g. The buccal cavity, pharynx, oesophagus and crop are all part of the foregut, which is ectodermal in origin¹⁷⁴, and they do not allow exchange of nutrients through

their walls into the coelom (the main body cavity surrounding and containing the digestive tract and other organs). This is the reason the NPs were observed passing through or accumulating inside the digestive tract, but not moving into the coelom in the head. However after the NPs migrated into the midgut—where most digestion and absorption of nutrients takes place in insects—some NPs entered the coelom through the midgut wall (Figure 53h blue).

After 24 hrs, the NPs have continued moving through the digestive system and are located in the abdomen of the mealworm (Figure 52). Figure 53i shows the NPs accumulated along part of the midgut and in the proctodeum (hindgut or terminal portion of the insect digestive system) in the 24 h fed mealworm. The blue circles in transverse slices shows the NPs localized in the midgut (Figure 53j&k). With the exchanging of the nutrients allowed in the midgut, NPs were absorbed, accumulated and encapsulated inside the coelom (Figure 53j&k white). Figure 53l shows the NPs inside the anterior intestine, which is part of the hindgut. The hindgut is also ectodermal in origin and does not allow nutrient exchange. All solid materials that migrated to the proctodeum would be eventually excreted through the anus.

In addition to NPs inside the mealworm beetles, we also found NPs adhering to their outside surface. We attribute this to mealworm grooming-during and after eating, they use their legs to “clean” the mouthparts, the head and the body, thus spreading NP’s over their exterior surface. NPs adhering to the outside surface of the mealworm body are marked with green markers in Figure 53.

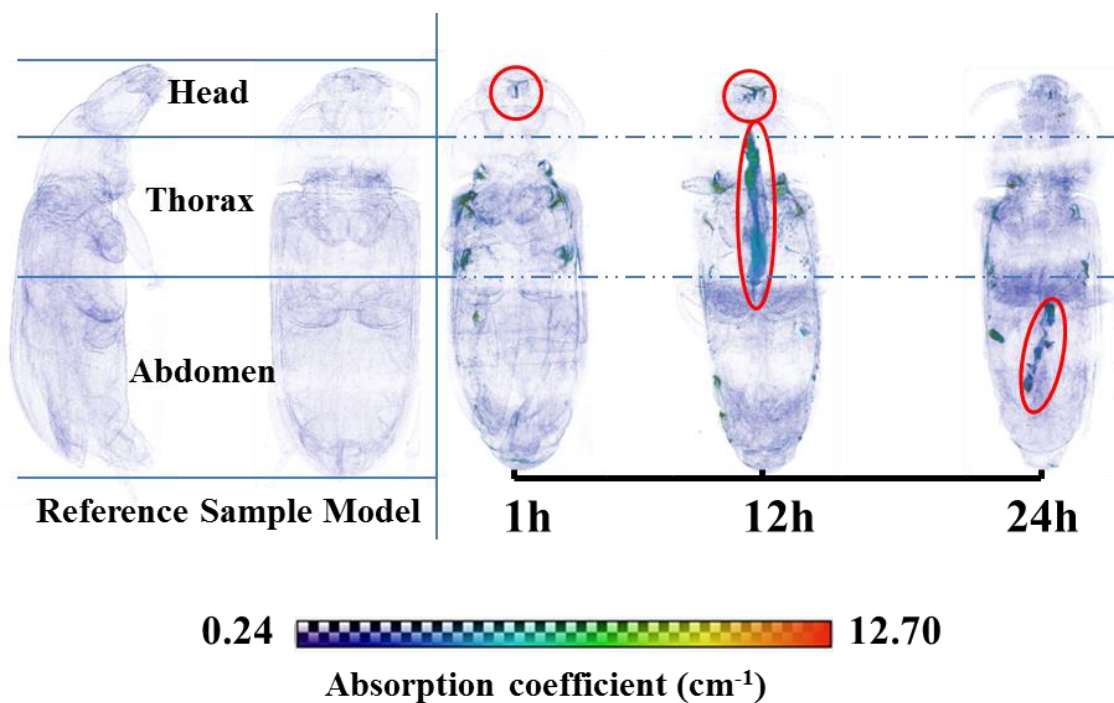


Figure 52. The translocation of NPs within mealworms with extended feeding time. 3D Visualization of samples, using the (above/below/difference) data. The most concentrated distribution of NPs inside the mealworms is labeled with red circles. Regions of apparently high NP concentration that are not circled are on the outside surface of the mealworm, spread by their grooming actions.

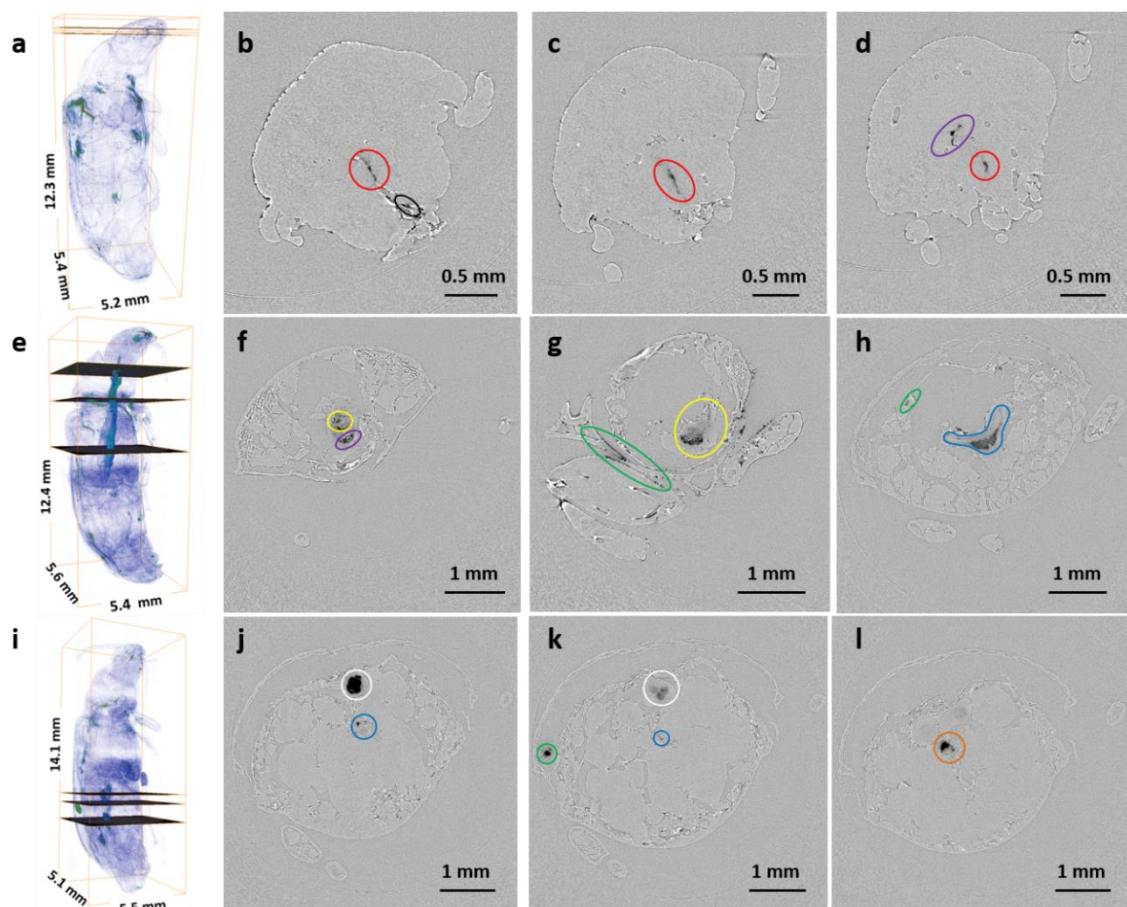


Figure 53. The localization of NPs inside the digestive system of the mealworms. (a), (e), and (i) show 3D visualizations and indicate the locations of three slices which are displayed to the right of those panels. (a) head segment of 1 h fed mealworm sample, (e) thorax segment of 12 h fed mealworm sample, (i) abdomen segment of 24 h fed mealworm sample. The dark (nearly black) regions within the colored circles are identified as NPs; other dark areas result from the shift of biological tissue between the two X-ray scans. Colored circles correspond to: Black: Buccal cavity; Red: Pharynx; Purple: Oesophagus; Yellow: Crop; Green: on Surface; Blue: Midgut; White: Encapsulated NPs inside Coelom; Orange: Anterior Intestine.

We identify and visualize the accumulation of NPs in specific organs in 3D in

Figure 54. When NPs have moved inside the coelom, a hemocyte-mediated reaction from the hemolymph encapsulates the particles, a defense response system that we have reported earlier in other insects¹⁷⁵. Once the NPs are encapsulated in the coelom, they

are not excreted through the anus, and the probability of NPs accumulation and subsequent translocation to higher trophic animals increases.

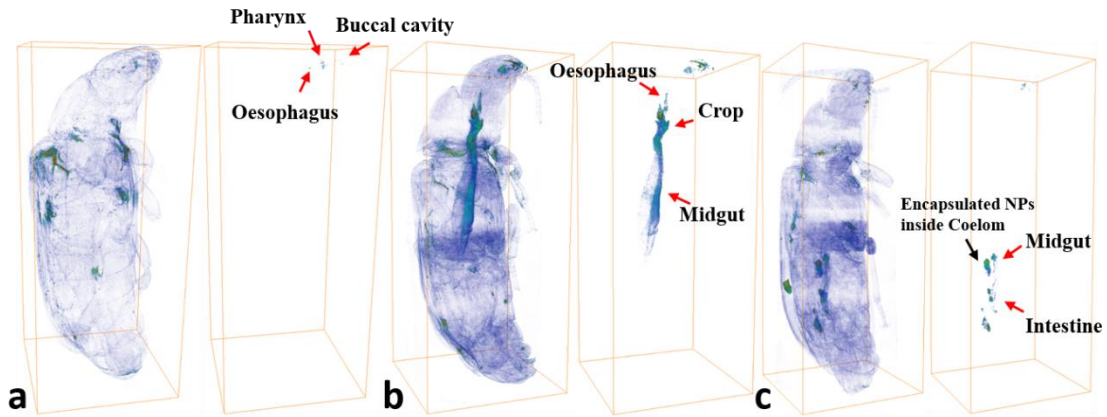


Figure 54. The distribution of NPs within mealworms organs. The accumulated NPs inside the (a) 1 h, (b) 12 h and (c) 24 h fed mealworm.

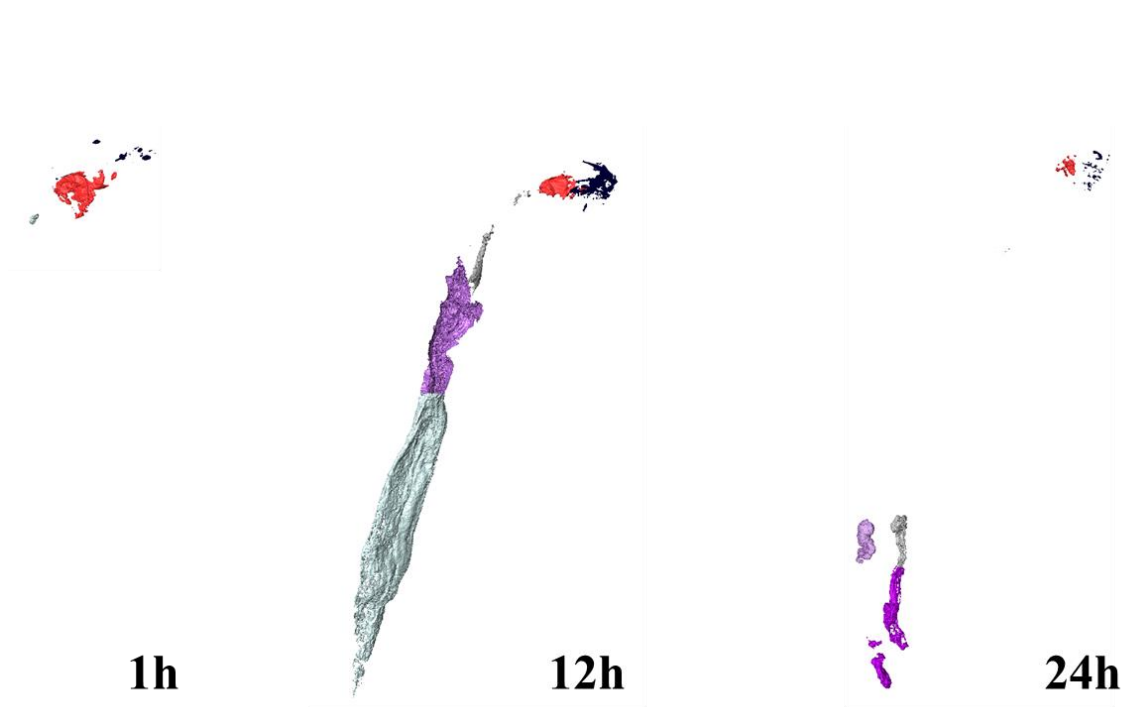


Figure 55. The surface views of accumulated NPs at different parts in mealworms. Each color represents a different organs corresponding to Figure 53.

5.3. Probing of yttria NPs in cabbage

Plants are essential components of ecosystems and they not only provide organic molecules for energy but they can also filter air and water, removing certain contaminants¹⁷⁶. Definitely, plants play a very important role in uptake and transport of ENPs in the environment¹⁷⁷. Nanoparticles are known to interact with plants and some of those interaction have been studied to understand their potential health and environmental impact, including quantum dots¹⁷⁸, zinc oxide¹⁷⁹, cerium oxide¹⁸⁰, iron oxide¹⁸¹, carbon nanotubes¹⁸², among others^{183,184}. The uptake of various ENPs by different plants was summarized in Table 8. Nanoparticles are known to stimulate morphological and physiological changes in several edible plants¹⁸⁵. Hawthorne *et al.* noted that the mass of Zucchini's male flowers were reduced by exposed to CeO₂ NPs¹⁸⁰. Quah *et al.* observed the browner roots and less healthy leaves of soybean treated by AgNPs, but less effects on wheat treated under same condition¹⁸⁴. Qi *et al.* reported that the photosynthesis in tomato leaves could be improved by treated with TiO₂ NPs at appropriate concentration¹⁸⁶.

Table 8. The uptake of different ENPs by plants

ENPs	Plants	Uptake	Ref.
NaYF ₄ :Yb,Er	Pumpkin seedlings (<i>Cucurbita maxima</i>)	Root/stem/leaf	89
CdSe/ZnS QDs	A. Thaliana plant	Root	178

Table 8. Continued

ENPs	Plants	Uptake	Ref.
ZnO	Maize (<i>Zea mays L.</i>)	Root	179
CeO ₂	Zucchini (<i>Cucurbita pepo L.</i>)	Root/stem/leaf/flower	180
Fe ₃ O ₄	Pumpkin (<i>Cucurbita maxima</i>)	Root/stem/leaf	181
C ₇₀	Rice (<i>Oryza sativa L.</i>)	Root/stem/leaf	182
AuNPs	Rice (<i>Oryza sativa</i>)	Root/shoot	183
	Radish (<i>Raphanus sativus</i>)	Root	
	Pumpkin (<i>Cucurbita maxima</i>)	Root	
	Ryegrass (<i>Lolium perenne L.</i>)	Root/shoot	
AgNPs	Soybean (<i>Glycine max</i>)	Root/shoot	184
	Wheat (<i>Triticum aestivum</i>)	Root/shoot	

The uptake, translocation and bioaccumulation of yttria NPs in edible cabbage (Brassicaceae, *Brassica oleracea*) have not been addressed until this study. This plant species was chosen and tested as part of a closed hydroponic system designed to study nanoparticles movement and distribution in a Substrate-Plant-Pest system as a model of a simple and controlled environment. The final test “substrate” used was plain distilled water (to avoid NPs to attach or react with other substrate elements), in which the tested NPs were mixed.

In order to observe the translocation and distribution of ENPs in plants, transmission electron microscopy (TEM) has been one of the most commonly used

techniques to identify the localization at cellular scale in two-dimensions (2D), because it can be used to observe all kinds of ENPs^{187,188}. On the other hand, ENPs with special properties, such as upconversion NPs and quantum dots with a particular band gap can be studied with a confocal microscope with alternative excitation wavelengths to trace the ENPs^{89,189}. Several synchrotron radiation imaging techniques exploiting high energy X-ray have become widely used in plant science, which can measure both spatial and chemical information simultaneously, like micro X-ray fluorescence and computed tomography¹⁹⁰⁻¹⁹².

5.3.1. Cabbage culture and exposure to nanoparticles

Cabbage plants were reared in a Hydroponic system. Seeds of cabbage were placed in 38mm compressed (100% peat) plugs and placed in a hydroponic mix containing water to which a 2-1-2 (NPK) solution (118 mL per 20 gallons of water) was added every week. Once plants had 4 true leaves, they were extracted from the main culture system, cleaned and placed into two groups. One group was placed in a glass jar (1 pint) containing distilled water and yttria NPs (10 plants per jar), the other was placed in only distilled water (10 plants per jar; as control). The 0.120 g NPs were added to distilled water in a small Nalgene container, mixed with a mini vortexer, and then added to the distilled water up to 0.38 L in the final testing glass jar. All jars had an air pump in them which were running 24/7 (Figure 56). The distilled water inside the glass jars containing NPs were kept in movement with the air pump working 24/7. NPs did not form conglomerates in the hydroponic testing system. The “substrate” used was plain distilled water (to avoid NPs to attach or react with other substrate elements), in which

the tested NPs were mixed. Even though both groups showed clear sign of stress after 10 days, they were maintained in this system for a total of 22 days. About 30% of the plants tested (with and without NPs) were wilted, the plants that were in better shape were collected, cleaned thoroughly with distilled water, dried and fixed with Kahle's, a fixing agent that provides sharp and clear preservation of nuclear structure of plant or animal tissues. Once received for imaging, plants were extracted from the container and let dried before placing them in the Synchrotron X-ray micro-tomography equipment.



Figure 56. Hydroponic system for cabbage exposure to yttria NPs

5.3.2. Identifying nanoparticles in cabbage

The μ -XCT was carried out at Beamline 8.3.2 at the Advanced Light Source, Lawrence Berkley National Laboratory. From scanning energies of 16.5 to 17.2 keV, below and above yttrium K-edge, the X-ray attenuation coefficient sharply increases by a factor of 5. The slices collected above and below the K-edge were set with same brightness

and contrast settings to fairly compare with each other (Figure 57). The grayscale values of reconstructed slices represent the absorption coefficient; therefore, the bright regions in subtracted slice denote the localization of yttria NPs (Figure 57c arrowed). Other elements appear dark in subtracted slice marked with a red “▲” (Figure 57f). These are inorganic elements which support the growth of cabbage. Some biological structures suffered radiation damage during scanning, resulting in a small amount of shrinkage. The bright regions circled in Figure 57c were caused by such shrinkage, resulting in a registration mismatch between the images above and below the edge. To identify and map the distribution of yttria NPs, an image segmentation protocol was employed that could highlight regions with yttria without finding these regions corresponding to sample shrinkage.

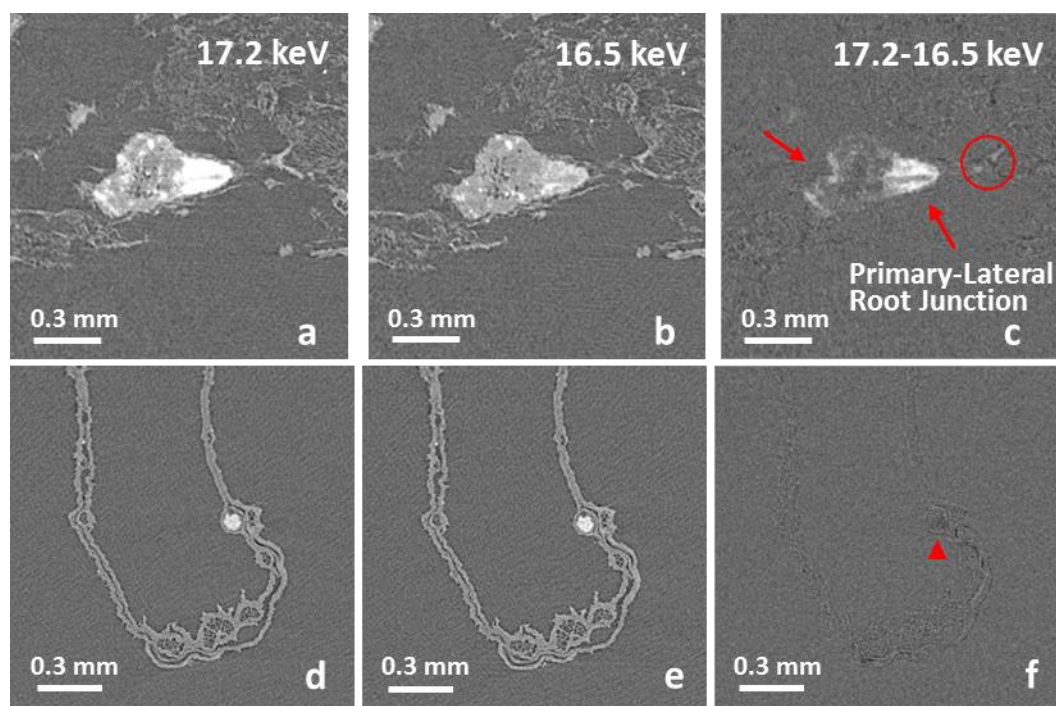


Figure 57. Transverse reconstructed slices at the junction between primary root and lateral root scanned at (a) 17.2 keV, (b) 16.5 keV, and (c) subtracted slice. (d–e) The slices for leaf section

The image segmentation was carried out by Avizo software to identify and display the distribution of NPs in 3D visualization. Figure 58 takes a root section image as an example to show the procedure and changes of segmentation. Figure 58a&b were the transverse slices scanning at 17.2 and 16.5 keV. Though the dual-energy slice datasets were scanned at the same anatomic location, the slight shrinkage and shift of the biological structure could take place during the hard X-ray radiation. Image registration was firstly employed to compensate for such shift and obtain the better quality of subtracted slices. Figure 58c&d are the subtracted slices obtained without and with image registration, respectively. The 17.2 keV reconstructed datasets were thresholded with the pixel value 3.8 corresponding to the pixel values of two reconstructed datasets of roots (marked “X” in Figure 59), with count of 17.2 keV datasets more than that of 16.5 keV (Threshold A). The subtracted datasets were thresholded with 3 according to the Figure 58e, as the pixel values less than 3 (light and deep blue labels) could be caused by the organic plant body or the noise (Threshold C). All pixel values above the threshold were labeled as 1, with candidate NPs; whereas non-labeled areas were set as 0. The shift due to the sample motion or shrink during scanning can be identified by the regions of increased darkness adjacent to regions of increased brightness (Figure 58d circled). The darkness regions (pixel value less than 0) will be selected and dilated in 3D with 26 adjacent voxels. The dilation regions were labeled as 1 (Threshold D). Figure 58f was derived by arithmetic with Threshold A, C and D as Table 9 shows. Figure 58g is the dilation of Figure 58f with 26 adjacent voxels in 3D. Figure 58h was obtained by removing the pixel value over 3 in Figure 58g (Table 9). The final segment was derived via subtracting the non-yttria regions

which were generated by the shifting of high-Z elements (Figure 58i). The arithmetic was with Threshold B, E and Figure 58h (Table 9).

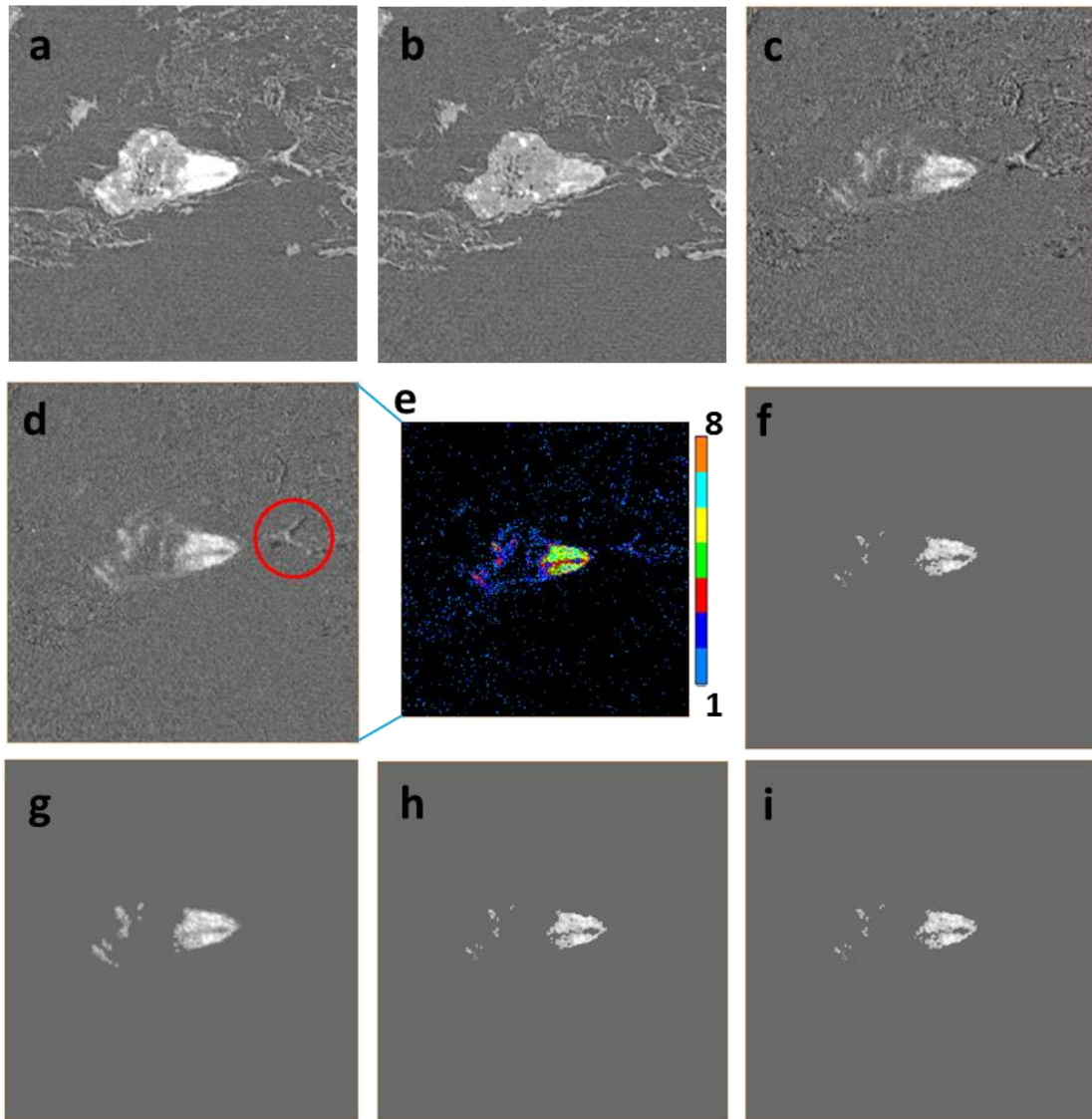


Figure 58. The process of image segmentation. (a). Reconstructed image obtained 17.2 keV. (b). Reconstructed image at 16.5 keV. (c). The subtracted slice from (a) and (b). (d). Subtracted slice with an image registration function. (e). Colors label the intensity of pixel value of (d). (f-i) Image segmentation based on the threshold of (a, b). Detailed data of images (f-i) is listed in Table 9.

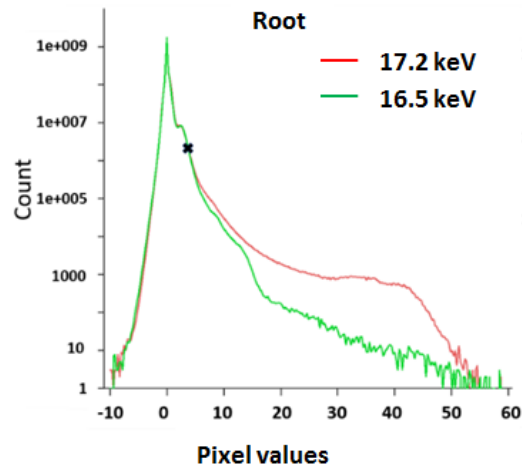


Figure 59. Histograms of image pixel value (absorption coefficient) for root.

Table 9. The characterizations for the sub-Figure 58.

	Characterizations
Figure 58a	17.2 keV; Threshold A : pixel value no less than 3.8; Threshold B : no less than 12
Figure 58b	16.5 keV; Threshold C :no less than 3; Threshold D : dilation for less than 0; Threshold E : between 3 and 4
Figure 58c	17.2-16.5 keV without registration
Figure 58d	17.2-16.5 keV with image registration
Figure 58e	Labeled color map due to pixel value
Figure 58f	Threshold A * C - D
Figure 58g	Dilation of Figure 58f
Figure 58h	Figure 58g * Threshold C
Figure 58i	Figure 58h – (Threshold B * E)

5.3.3. Three-dimensional distribution of nanoparticles in cabbage

By using K-edge subtracted image technique with Monochromatic X-ray tomography, the translocation and distribution of NPs in the cabbage root is clear (Figure 60). Figure 60a&b were constructed by 17.2 keV and 16.5 keV reconstructed slice datasets, respectively. Their color maps were based on the transverse slice pixel values/absorption coefficients over the range from 0.2 to 17.8 cm^{-1} . An obvious difference between 17.2 and 16.5 keV visualization in absorption coefficient of yttria NPs was observed. The distribution of yttria NPs in root was segmented and colored in red (c). A large amount of NPs were found aggregated at left bottom of the root. Since yttria NPs were not water-soluble, the water that contained them was kept in constant movement with an air pump working 24/7. However, it seems that the dense roots formed a web-like structure that made the suspended NPs to accumulate and aggregate among the roots. Uptake of NPs by the root has been observed at primary and lateral root junction as well according to the transverse slice. Figure 57a is one transverse slice localized at the arrow in Figure 60c (blue arrow) showing the junction between primary root and lateral root. We found that the yttria NPs were absorbed by the lateral roots, and particulates began to accumulate along the outer epidermis of primary roots with limited entrance into the vascular tissue (xylem and phloem) of the primary root. It might happen that endodermal cell walls were blocking the entrance of aggregated yttria NPs into vascular tissue¹⁷⁹. This is shown in the upper section of the 3D visualization (Figure 60c) where no yttria NPs were observed above the root system.

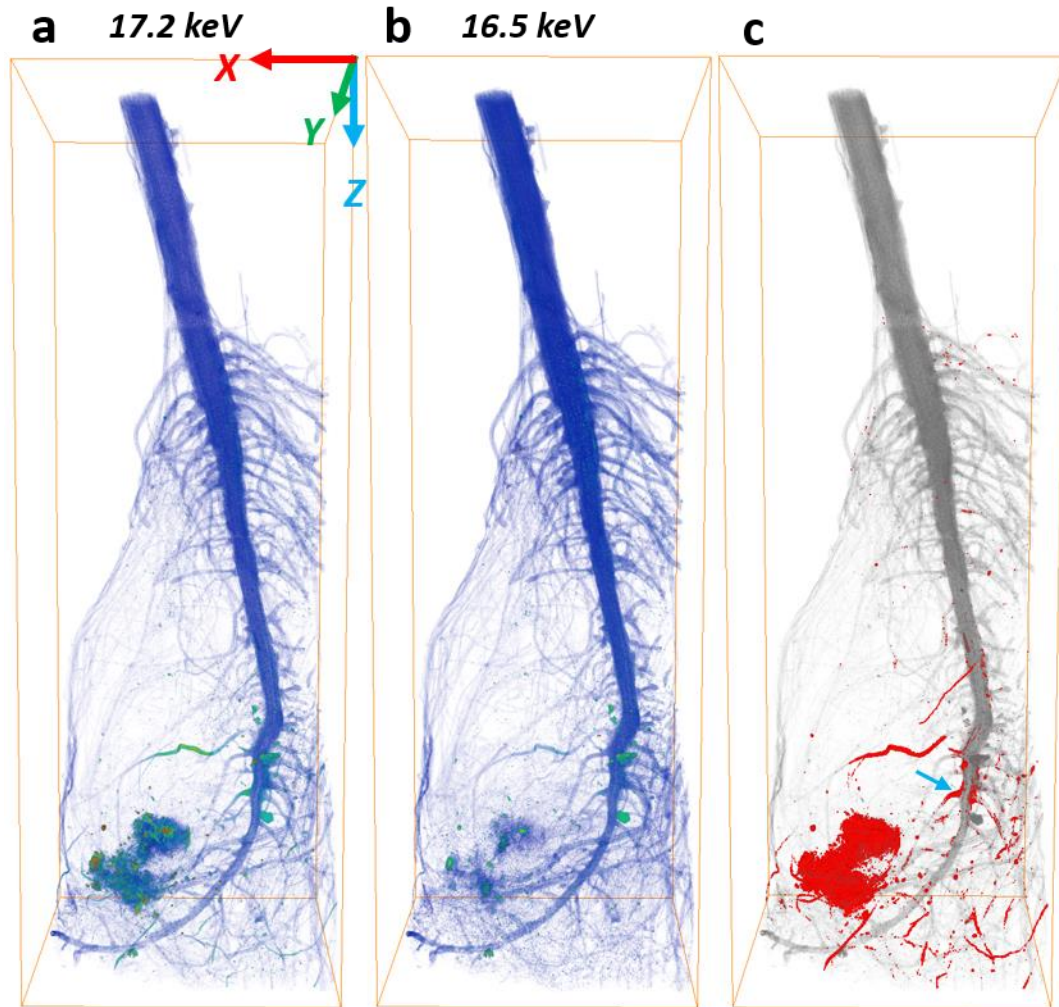


Figure 60. The 3D visualization for a wide view of root built by (a) 17.2 keV transverse reconstructed slice datasets and (b) 16.5 keV datasets. (c) Distribution of yttria NPs (red) in root. The grey visualization was built by 17.2 keV; the red one was built by the subtracted datasets. The bounding box size is $6.77 \times 5.10 \times 19.40$ mm

Besides the full view of the translocation in the cabbage root system, the distribution of yttria NPs at the micro-scale within a lateral root was detected and investigated (Figure 61). Figure 61a shows the localization of the micro-scale lateral root visualization. The 3D visualization of micro-scale was built by the segmented transverse reconstructed slices, and the red regions were localized yttria NPs (Figure 61b&c). It is

clear that roots are able to uptake the yttria NPs in ground tissue (GT), which appear to accumulate in the root with limited entrance of yttria NPs into vascular tissue (VT) being transported through the Xylem. Xylem vessels are small with diameters usually smaller than 1 μm in vegetables like Cabbage plants to over 100 μm in vessels found in trunks of large trees¹⁹³. Vessels allow nutrients contained in water to be distributed throughout the plant. For NPs, however, if they aggregate, the blockage is expected, that is what we have observed in this study. Long term studies might show that yttria NPs might provide more negative than positive effects on plant growth and development as found with other NPs (i.e. AuNPs, AgNPs)¹⁸⁵.

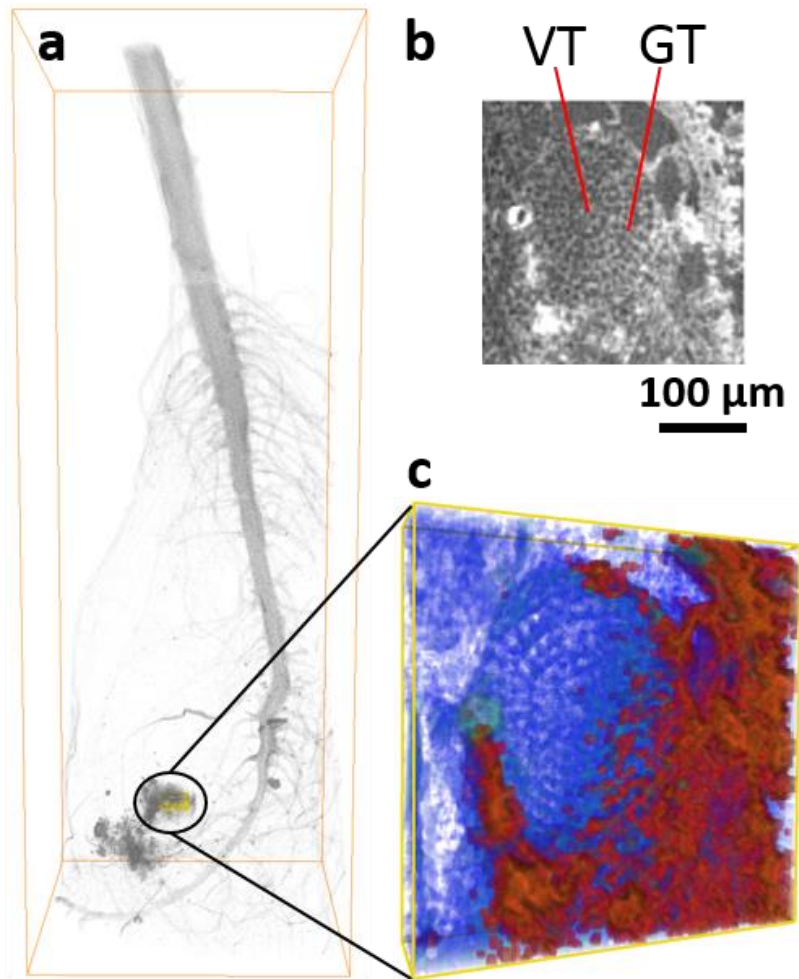


Figure 61. The micro-scale of root segmentation localized at yttria NPs aggregated regions. (a) The selected yellow region in 17.2 keV visualization. (b) The top transverse slice of yellow frame region. (c) Magnified view of yellow frame. The vascular tissue (VT) and ground tissue (GT) are shown in (b). The red regions in (c) show the distribution of yttria NPs. The yellow frame size is 0.58 x 0.58 x 0.13 mm

5.3.4. Quantification of Nanoparticles

Using K-edge subtraction image technique with dual-energy X-ray scanning, the concentration of target NPs can be calculated. This method has been discussed elsewhere¹⁹⁴⁻¹⁹⁶. The reconstruction of monochromatic X-ray gives a value of absorption coefficient, which is attributed by two objects: the target NPs and the body of

sample. The measured absorption coefficient μ of each pixel (x,y) in reconstructed images can be expressed as equation (10):

$$\mu(x, y) = \frac{\mu}{\rho_{NPs}} \rho_{NPs}(x, y) + \frac{\mu}{\rho_{body}} \rho_{body}(x, y) \quad (10)$$

where $\frac{\mu}{\rho_{NPs}}$ and $\frac{\mu}{\rho_{body}}$ are the mass absorption coefficients of target nanoparticles and

body of sample, respectively. ρ_{NPs} and ρ_{body} are the concentration. Therefore, for the

reconstructed datasets scanned at high and low energy can be expressed as equations

(11-12):

$$\mu_H(x, y) = \frac{\mu}{\rho_{NPs}}(E_H) \rho_{NPs}(x, y) + \frac{\mu}{\rho_{body}}(E_H) \rho_{body}(x, y) \quad (11)$$

$$\mu_L(x, y) = \frac{\mu}{\rho_{NPs}}(E_L) \rho_{NPs}(x, y) + \frac{\mu}{\rho_{body}}(E_L) \rho_{body}(x, y) \quad (12)$$

where E_H and E_L are the scanned energies above and below K-edge energy. Because E_H and E_L are close to the K-edge energy, the mass absorption coefficient of body, such as carbon element, are unchanged much at two scanned energies. Therefore, the difference

between $\frac{\mu(E_H)}{\rho_{body}} \rho_{body}(x, y)$ and $\frac{\mu(E_L)}{\rho_{body}} \rho_{body}(x, y)$ can be ignored. By using equation (11)

minus equation (12), the absorption coefficient in subtraction image can be can be

simplified to the following form as equation (13):

$$\Delta\mu(x, y) = \frac{\mu}{\rho_{NPs}}(E_H) \rho_{NPs}(x, y) - \frac{\mu}{\rho_{NPs}}(E_L) \rho_{NPs}(x, y) \quad (13)$$

The concentration of target nonparties (ρ_{NPs}) can be formulated as equation (14):

$$\rho_{NPs}(x, y) = \frac{\Delta\mu(x, y)}{\frac{\mu}{\rho_{NPs}}(E_H) - \frac{\mu}{\rho_{NPs}}(E_L)} \quad (14)$$

where $\Delta\mu$ is the difference in absorption coefficient obtained by subtraction between two energies. The value for $\Delta\mu$ is obtained from the voxel value of subtracted datasets, and the mass absorption coefficient is from Argonne National Laboratory (Compute X-ray Absorption).

The volume rendering enable the 3D visualization for the concentration map of yttria, shown in Figure 62b. By using this formula, the calculated concentration is based on the voxel level. The minimum concentration was 44.12 mg/cc and the maximum was 551.47 mg/cc (to display the mapping colorful, the maximum set as 132.35 mg/cc). The grey visualization (setting 30% transparent) of root shows the distribution and localization of yttria NPs. Using Avizo software with image segmentation and label-analysis, the total voxel volume of root is measured as 5.41604e+07 voxels. Figure 62a shows the full volume of the root section. As shown the concentration of nanoparticles at root was estimated in the range from 0.82 $\mu\text{g/L}$ to 10.18 $\mu\text{g/L}$.

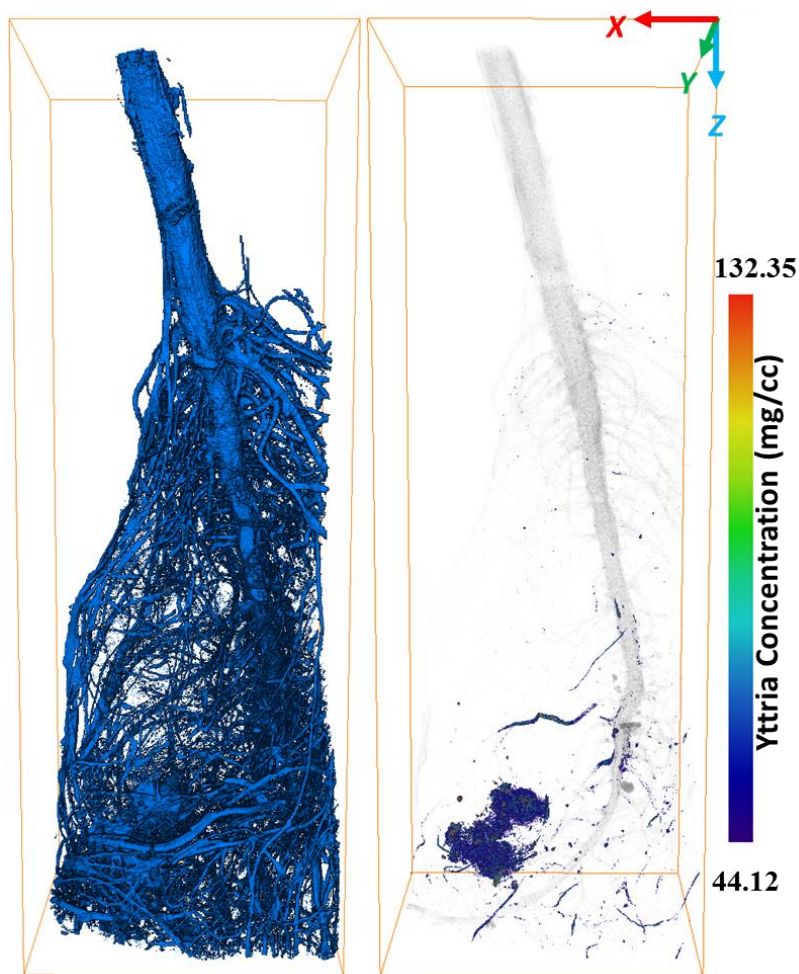


Figure 62. (a) The full volume visualization of plant root. (b) Concentration map of yttria NPs in root (on the voxel level)

For the cabbage shoot, no yttria NPs were observed (Figure 63), which means that no yttria NPs transported from roots to shoots. As we found no yttria NPs entering vascular tissues of primary root, the yttria NPs accumulated making it difficult to be transported by xylem from the root to the rest of the plant. Despite no clear evidence of yttria translocation, other elements were observed in the shoots. In general, the higher the atomic number (Z), the higher the absorption coefficient for a given X-ray energy. It is clearly to

see some high-Z (compared with carbon) elements distributed in both roots and shoots. Crops require many mineral elements for their growth, such as calcium, magnesium, zinc, copper and iron ^{197,198}. These high-Z elements could be the mineral elements absorbed by cabbage before the cabbage root exposed in the hydroponic system containing yttria NPs.

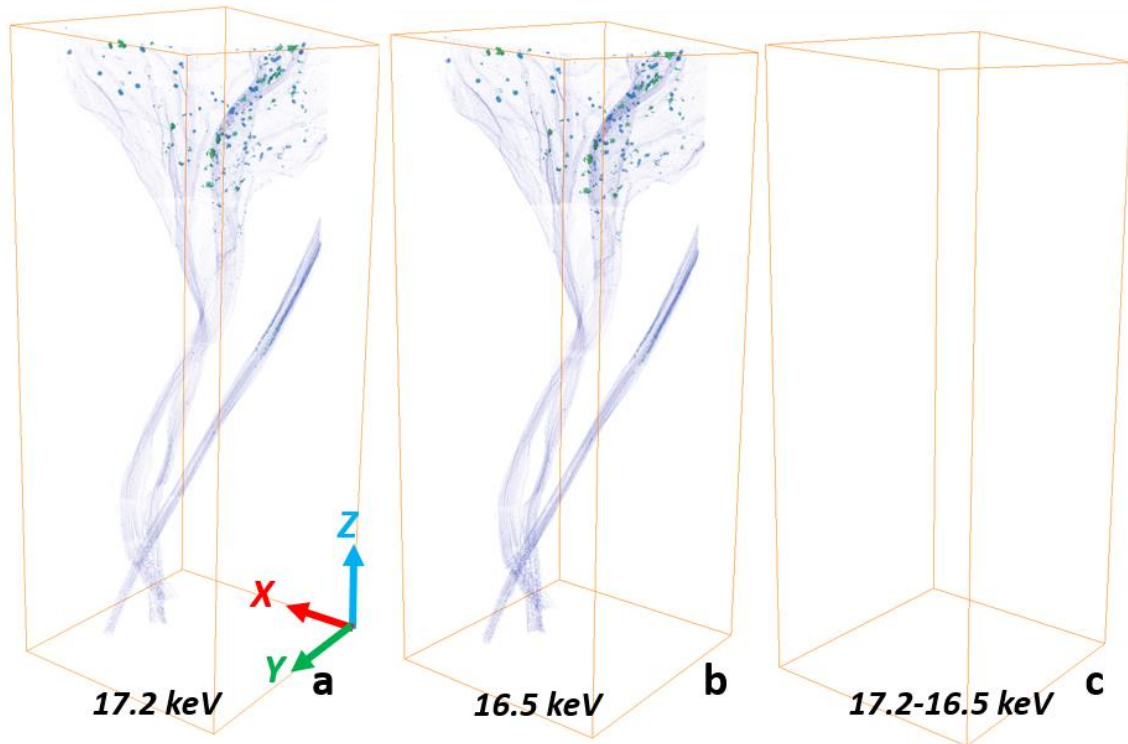


Figure 63. The 3D visualization of shoot section for cabbage built by (a) 17.2 keV transverse reconstructed slice datasets and (b) 16.5 keV datasets. (c) Distribution of yttria NPs in shoot. The bounding box size is $7.65 \times 7.29 \times 19.40$ mm

What are the possible uptake mechanisms based on the observation? As shown above, we observed that some yttria NPs were uptaken by the roots of cabbage plant (Figure 57a-c and Figure 60). The cell wall is considered as a tight and significant sieve which blocks the migration of NPs ¹⁹⁹. The typical pore sizes of a cell wall are in the range of 2-20 nm ²⁰⁰. In our case, the yttria NPs sizes are larger than the pore sizes,

therefore, the passage for NPs through the pores of cell walls should be difficult. On the contrary, the larger NPs were found to be taken up by roots or shoots that are in correlation with previous reports^{181,201,202}. It is not that clear which route NPs can penetrate the cell wall for all these cases. Shen *et al.* reported that an endocytosis-like structure was observed in *Arabidopsis thaliana* leaf cells²⁰³. Therefore, the yttria NPs could penetrate the cell wall and be taken up by the roots. In addition, the dissolution rates of rare earth oxides are too low to be relevant²⁰⁴. Even though some yttria NPs penetrated into the ground tissues, the yttrium ions were not established. This could be the reason the yttria NPs only observed in ground tissue and blocked at primary-lateral-root junction.

5.3.5. Limitations in KES

Although a KES method can identify the localization of target NPs, if the concentration of root-to-shoot-transported yttria NPs was too low, the target NPs could not be detected. Furthermore, the KES method is based on the difference in attenuation coefficient of yttrium element over K-edge. This method is able to identify the yttrium-based NPs but it cannot distinguish the biotransformation of yttria.

5.4. Summary

In this chapter, in situ detection of NPs on in biological system is discussed. For the first time, we could observe NPs in those systems. First, we use three different imaging techniques to observe the NPs inside the fire ants. We compare the advantages

and disadvantages of three techniques. Additionally, we detect the distribution and localization of NPs inside ants.

Second, we used dual-energy K-edge subtraction to track two-dimensional yttrium oxide (Y_2O_3) nanoparticles (NPs) in mealworms. We clearly identified the Y_2O_3 nanoparticle accumulation locations as they passed through the mealworm digestive system, and importantly, we also found that NPs passed into and accumulated in the coelom. Accumulation of NPs at coelom could result in their translocation to higher trophic level animals and potentially lead to toxicity and biomagnification.

Third, we use same method to investigate the interaction of yttria NPs with edible cabbage. By using the KES technique, the μ -XCT can not only detect the chemical and spatial information in 3D, but also analyze the concentration of target NPs. The uptake, accumulation, and distribution mapping of yttria NPs in both micro scale and relatively full view of cabbage roots and stem were investigated. We found that yttria NPs were absorbed and accumulated in the root but not readily transferred to the cabbage stem. Compared with yttria NPs, other minerals were observed along the xylem in both cabbage roots and stem. To the best of our knowledge, few reports have studied the impact of yttria NPs on cabbage plants. In addition, by using μ -XCT with KES technique, the distribution and concentration mapping of nanoparticles in full view of plant root have not been previously reported.

CHAPTER VI

PROBING OF NANOPARTICLES IN ENGINEERING SYSTEM*

This chapter explores three imaging techniques about as-synthesized nanoparticles in engineering systems. It contains two sections: the first is focused on probing of NPs in grease; and the second is about the luminescent performance of assembled white light emitting diode (WLED) using YAG:Ce powder coated on a blue chip.

6.1. Grease

In today's worldwide market, lubricants are manufactured 40 million metric tons per year.⁹⁵ Most common lubricants are in liquid and solid. Lubricating greases are thixotropic gels dispersed a thickener in a liquid lubricant²⁰⁵. Inorganic additives in grease-based lubricants have played important roles in reducing frictional loss and preventing wear of mechanical systems^{206,207}. To date, there is lack of understanding about the behavior and performance of thickeners and additive particles in fluids, and more so in grease due to lack of efficient method to directly detect them. The existing literature has been focused on simulation and theoretical analysis, but most studies have not been experimentally verified²⁰⁸. A synchrotron-based micro X-ray CT (μ -XCT) offers high

*Part of this chapter reproduced with permission from "Direct observation of lubricant additives using tomography techniques" by Yunyun Chen, et al., *Applied Physics Letters*, **2016**, 109, 041603 (Copyright © 2016, AIP Publishing LLC).

resolution two-dimensional (2D) and 3D images at the micron scale^{85,86}. In addition, the μ -XCT scan can be utilized for a wide range of materials by adjusting the energy of the monochromatic X-ray.^{86,87} Although it is most common in medical applications, it has become a new method for detecting defects in industrial and electronic components in recent years. The high resolution of CT is capable of imaging cracks within industrial components, and defects within microelectromechanical systems (MEMS) and integrated circuits.

Iron oxide is commonly found in lubricating systems due to oxidation, tribo-oxidation, and wear of steels²⁰⁹⁻²¹¹. Being able to track iron oxide would enable us to understand mechanisms in lubrication and wear of steels as well as the effects of wear debris. The objective of current research aims to detect the behavior of additives and thickeners in grease.

6.1.1. Special fixture designing

The iron (II, III) oxide (Fe_3O_4 , 99.99%) were purchased from Sigma-Aldrich and used as additives without further purification. The grease, NCS-30, was provided by Jet-Lube (Houston, TX). In order to investigate the behavior of additives in grease, two groups of samples were studied using K-edge tomography. The first group was a commercial thread compound that has been used as industrial standard NCS-30, as a reference. The NCS-30 reference compound is commercial available, nonconductive, nonmetallic, and contain carbon based fibers and additives. This compound is blended with calcium complex (calcium soap thickener) based grease. The second group is the reference compound added with iron oxide (Fe_3O_4) as additive at 2.3 %wt. The samples were

deposited between the inner conical pillar and outer conical tube (Figure 64). The greases were deposited in the gap between two tubes. The shear force was applied by rotating the outer conical tube.

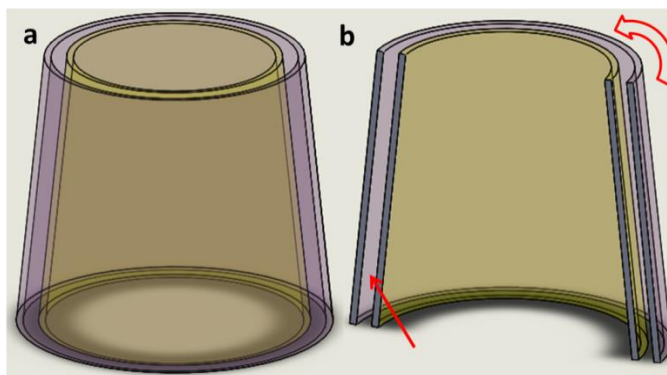


Figure 64. The rotating holder for shearing grease. (a) Dimetric view and (b) Section view of rotating holder.

6.1.2. Identification of thickeners and additives

The dual-energy computed tomography is an effective imaging technique to confirm the chemical identity of different species. This is due to the change of mass attenuation coefficient of different species radiated at dual energies, above and below the K-edge of the additive element. As Figure 65 shows, the mass attenuation coefficient of iron element in additive Fe_3O_4 particles has an intense raise (more than 5 times), once the scanning energies were moved from 6.9 keV to 7.2 keV, below and above the iron K-edge (7.112 keV, red line in Figure 65). Other elements, such as the carbon and calcium in NCS-30, have a decrease in mass attenuation coefficient over the same energy range (green and blue line). Moreover, once the element has a higher atomic number (Z), it does have a higher the attenuation coefficient. It is clearly to see that Calcium with high- Z has a higher attenuation coefficient. Therefore, the thickener and

additive in the grease can be distinguished. The pixel intensity values of the reconstructed datasets represent the absorption coefficient information of elements scanned by synchrotron X-ray.

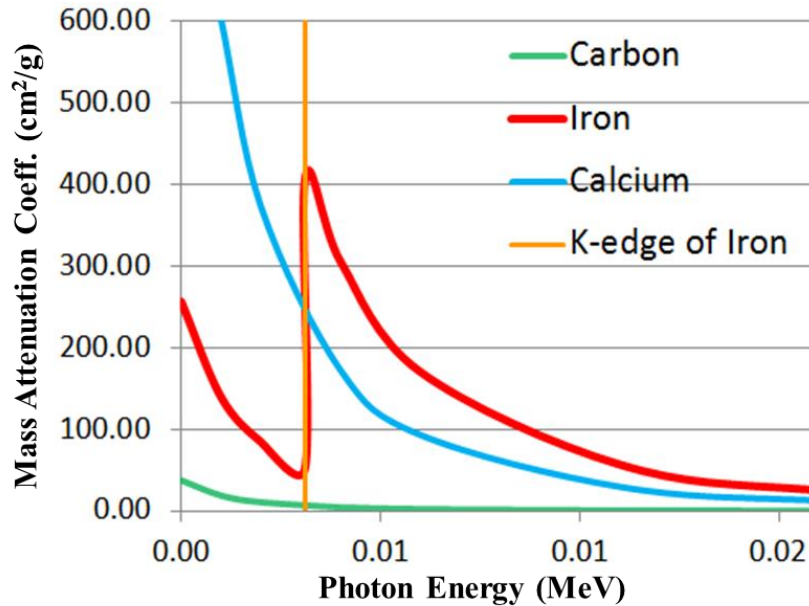


Figure 65. Graph of mass attenuation coefficient for carbon, calcium and iron. The value is derived from National Institute of Standards and Technology database (NIST X-ray Attenuation Databases).

Both groups have two reconstructed datasets obtained by imaging at 7.2 and 6.9 keV, and their absorption value distribution is shown in Figure 66. The solid line represents the commercial NCS-30 grease with Fe_3O_4 additive, and the dash line is representative of the grease without Fe_3O_4 additive. It is clearly shown that the pixel value in the images of the sample with additives is greater for both energies. We attribute this to the higher density of the group 2 sample. For the same chemical agent, the higher the concentration/density, the greater pixel intensity value/absorption coefficient²¹²⁻²¹⁴. This

will be discussed in detail in next section. Furthermore, comparing the above (red) and below (green) iron K-edge images, the pixel value distribution for the grease without Fe_3O_4 additive (dash line) has little change; whereas for the grease with Fe_3O_4 additive (solid line) there is evident difference, demonstrating the existence of Fe_3O_4 in grease. Figure 66b&c shows that 3D visualization of the grease without and with Fe_3O_4 additives using Avizo software stacking 2D reconstructed slices.

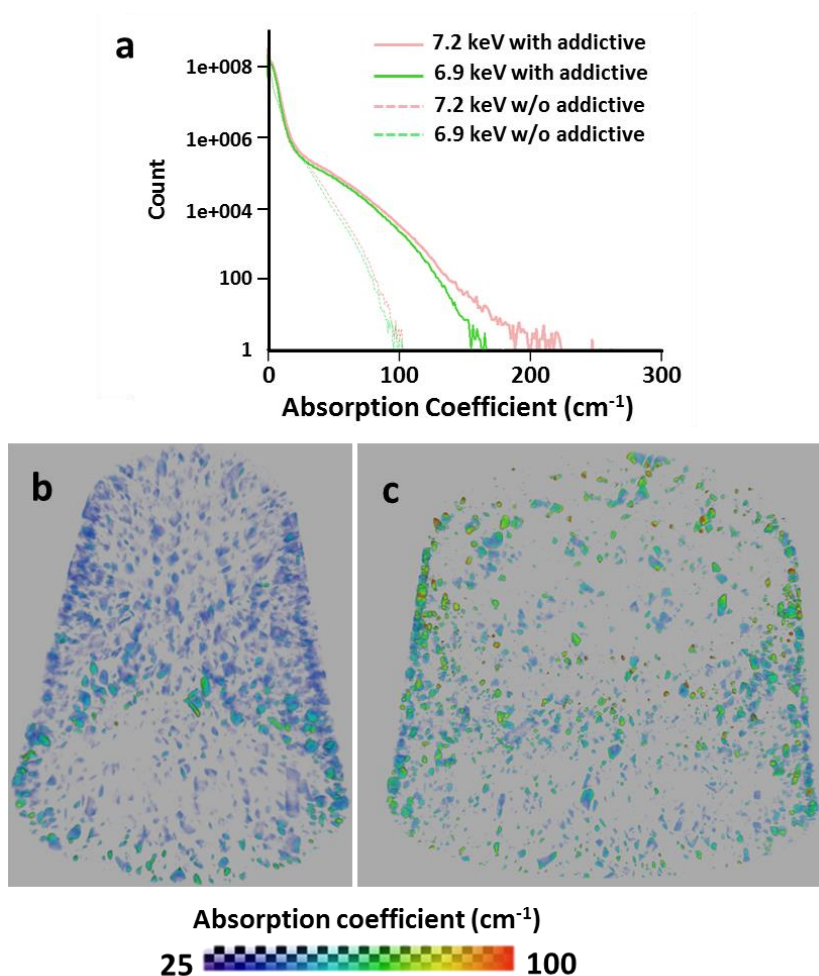


Figure 66. (a) The pixel value distribution of reconstructed datasets. The 3D visualization of grease without Fe_3O_4 additives (b) and with Fe_3O_4 additives (c). The height of both 3D models is 3.892 mm.

Based on 3D visualization, we found that the thickeners formed a film within the gap of sliding tubes. The film thickness can be estimated via pixel intensity. Figs. 4a and 4b are 2D slide obtained from the grease without and with Fe_3O_4 additives, respectively. As mentioned earlier, the higher the pixel intensity values in 2D reconstructed slices, the higher density of the film. . This is seen here in 2D transverse slices (Figure 67a&b) and 3D visualization (Figure 67c&d). As the gap became narrower due to sliding, the calcium thickener was compressed further and had a higher density.

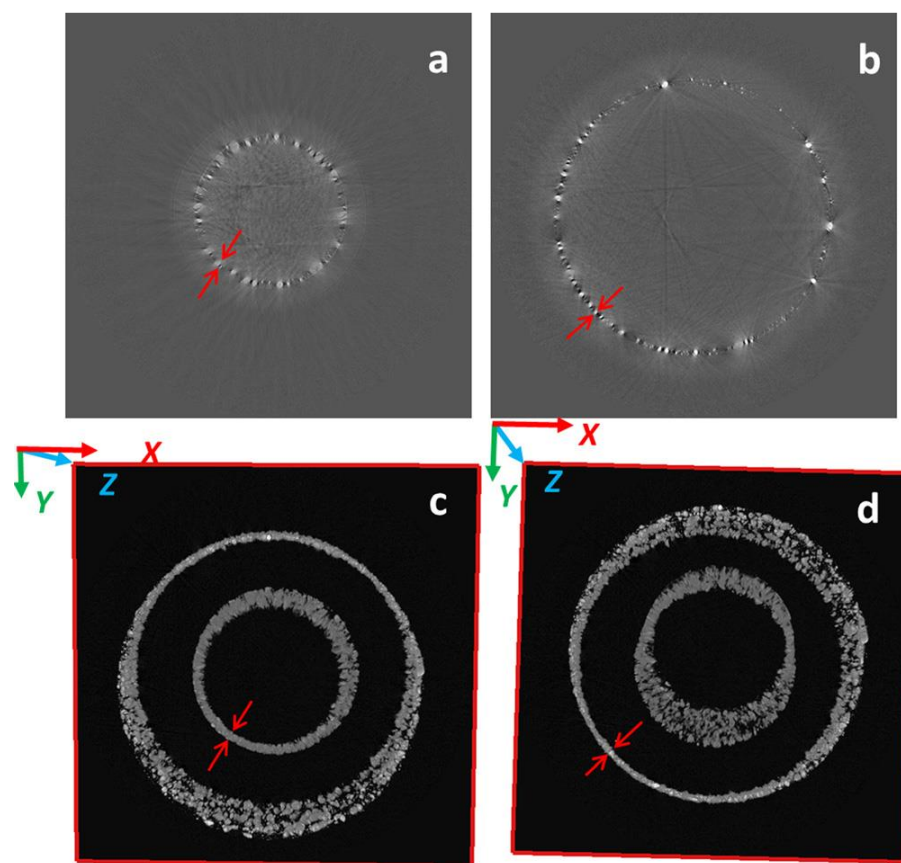


Figure 67. The 2D transverse slices of greases (a) without and (b) with Fe_3O_4 additives. The 3D visualization of samples (c) without and (d) with Fe_3O_4 additives. The slice with red frame in (c-d) is transverse 2D slice. The transverse slice size of (a-d) is 8.4000x8.400 mm.

6.1.3. Localization and distribution of particle additives

Based on the information of pixel, the image segmentation was conducted by using Avizo software to identify and present the distribution of additives. In order to avoid the non-Fe₃O₄ additive, the 7.2 keV with Fe₃O₄ additive dataset (group 2) was thresholded with pixel value 100. The 6.9 keV dataset of group 2 was thresholded with pixel value less than 60. The pixel value over 100 areas in high energy dataset and less than 50 areas in low energy dataset were segmented and labeled for Fe₃O₄ additive. The distribution of Fe₃O₄ additive in NCS-30 grease was shown in red regions (Figure 68a). As discussed earlier, the NCS-30 contains a base grease that is superior to metal adhesion. Our results in Figure 68a clearly show that some Fe₃O₄ particles are attached to the calcium complex particles (original additives) in the reference compound. Some are attached to the tube surface. The red colored particles (Fe₃O₄ added particles), aggregated mostly at the lower part in the Figure 68a are attached to the grey ones (calcium complex) throughout. The distribution of Fe₃O₄ additives adhering on single calcium complex particles is shown in the Figure 68b, the enlarge view of Figure 68a. It is clear to observe the Fe₃O₄ additives adhering at the edge of calcium complex particles. Furthermore, the Fe₃O₄ additives are located at specific edge of the calcium complex particles. This specific location could be corresponding to the shear direction. Besides adhering on the thickeners, some Fe₃O₄ additives are located on the surface of tubes as well.

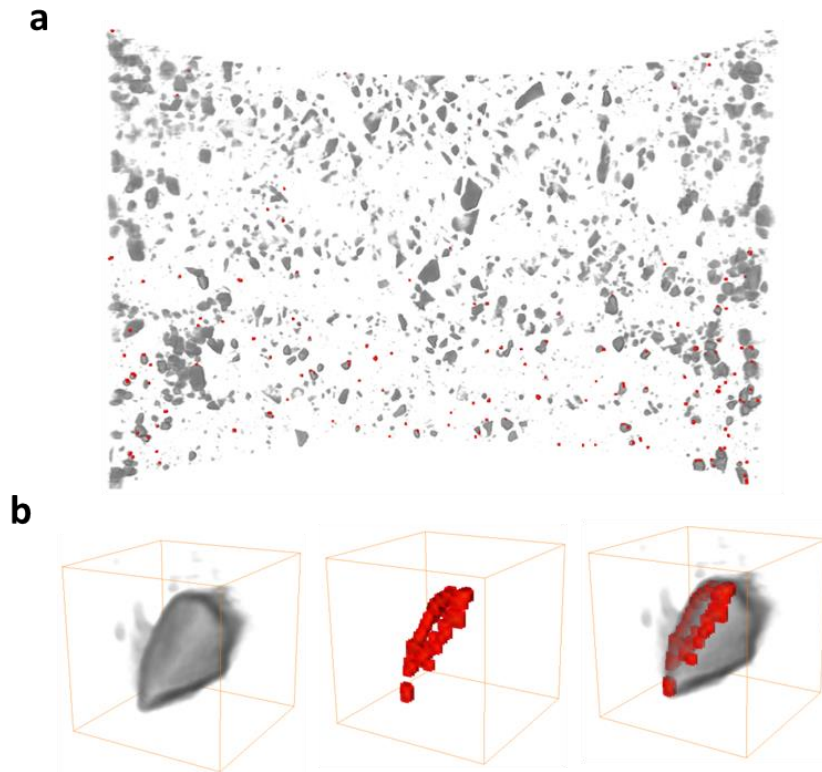


Figure 68. (a) The distribution of Fe_3O_4 additive shown in red regions. (b) The enlarge view of single calcium complex thickener (grey) and Fe_3O_4 additives (red). The box size is $98.89 \times 98.89 \times 98.89 \mu\text{m}$.

There is a potential error using this method. Because the grease is a solid-to-semifluid product, it flows during energy-ray scanning. In our experiments, there were two datasets obtained using two different X-ray energy radiations. Therefore, the images do not have exactly the same anatomic location. The small amount of shift causes a small error in the concentration or amount of the particles detected. As a result, some Fe_3O_4 particles were treated as a thickener. The concentration or volume is reduced. Regardless, the location of the Fe_3O_4 particles remain to be accurate and can be precisely detected.

6.1.4. Limitations of luminescence imaging in dispersion study

The OA-coated UCNPs were dispersed well in mineral oil. In order to study the dispersion of UCNPs in mineral oil, we used the home-made confocal laser scanning microscope. Because of the fluorescence resonance energy transfer (FRET) or energy re-absorption, the emission energy of UCNPs transferred to mineral oil. FRET is a process of non-radiation energy transfer in the form of phonons or lattice vibrations from energy donor to acceptor²¹⁵⁻²¹⁷. Energy re-absorption is a radiation process in the form of photons. The way to transfer energy from UCNPs to mineral oil greatly depends on the distance between UCNPs and mineral oil. If the distance is less than 100 Å, the preferred procedure is FRET, which transfers energy in the form of phonons or lattice vibrations. Otherwise, the alternative is re-absorption, which transfers energy as photons. Meanwhile, the emission band of energy donor overlaps the absorption band of energy acceptor, resulting in the energy transfer. In our case, the FRET or energy re-absorption occurred between UCNPs and mineral oil, leading to the luminescence quenching phenomenon.

6.2. White light emitting diode application of YAG:Ce

White light emitting diode (WLED) can be generated bi-chromaticism of blue and yellow²¹⁸, or tri-chromaticism of red, green and blue²¹⁹. Though YAG:Ce has good thermal stability and high photoluminescence quantum yield, it is lack of red components in emission spectrum resulting in the inefficiency in warm WLEDs.²²⁰ Hydrogen-treated TiO₂ nanocrystals have been reported to improve the photocatalytic

activities, photoconversion efficiency and capacitance of TiO₂, as hydrogen introduced the defects into the crystal.²²¹⁻²²³ Hydrogenation is a general strategy to improve the performance of TiO₂. In this research, the hydrogenation has been firstly used to induce the defects into the host lattice of YAG, which leads to a red-shift in the emission spectrum of YAG:Ce. To the best of our knowledge, hydrogen-treated YAG:Ce has not been previously studied. Furthermore, with the different coating concentration of YAG:Ce powder and alternative operating voltages, the luminescent colors of WLED were changed as well.

The as-synthesized YAG:Ce³⁺ powder was mixed with epoxy and coated on the InGaN-based royal blue chips. Figure 69 shows the distribution map of coated YAG:Ce on royal blue chips, which was carried out by home-made scanning confocal microscopy. As the powder does not disperse uniformly, the emission spectra of assembled WLED are different. Once the ratio of YAG:Ce powder to epoxy resin is small, the ratio of yellow to blue in spectra is decreasing. Two spots, coated with more powder (marked with circle) and less powder (marked with triangle), were selected. The luminescent color was changed with different ratio of YAG:Ce powder to epoxy resin, which display CIE (x and y) coordinates (Figure 70). With the different ratio, the color coordinates can shift from blue to yellow region. Meanwhile, with the hydrogen treatment, the output color of WLED can be changed.

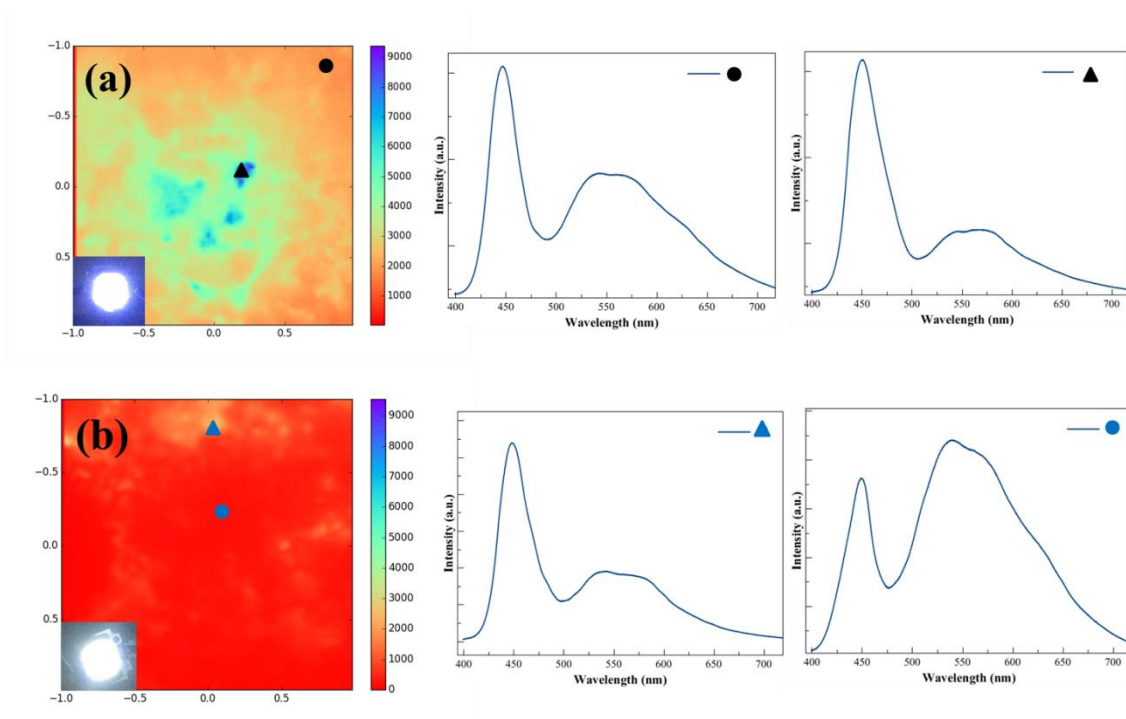


Figure 69. Distribution Map and emission spectra of coated (a) YAG:6%Ce+H₂ and (b) YAG:6%Ce.

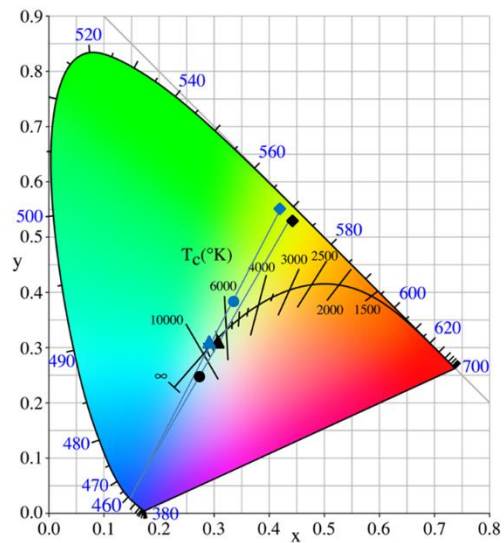


Figure 70. CIE color coordinates of YAG:Ce powder coated on the blue chips with different ratio of powder to epoxy resin. The blue markers represent the sample YAG:6%Ce and black markers are for YAG:6%Ce+H₂. Diamond: pure powder; Circle and triangle: coated powder on blues chips corresponding to Figure 69.

The spot (circle marker) in Figure 69a was selected to observe the color in CIE coordinate at different operating voltages (Figure 71). With the higher operating voltage, the luminescent intensity of WLED was increased (Figure 71a). With the increasing of the voltage, the output WLED moved towards cold light to warm white (Figure 71b).

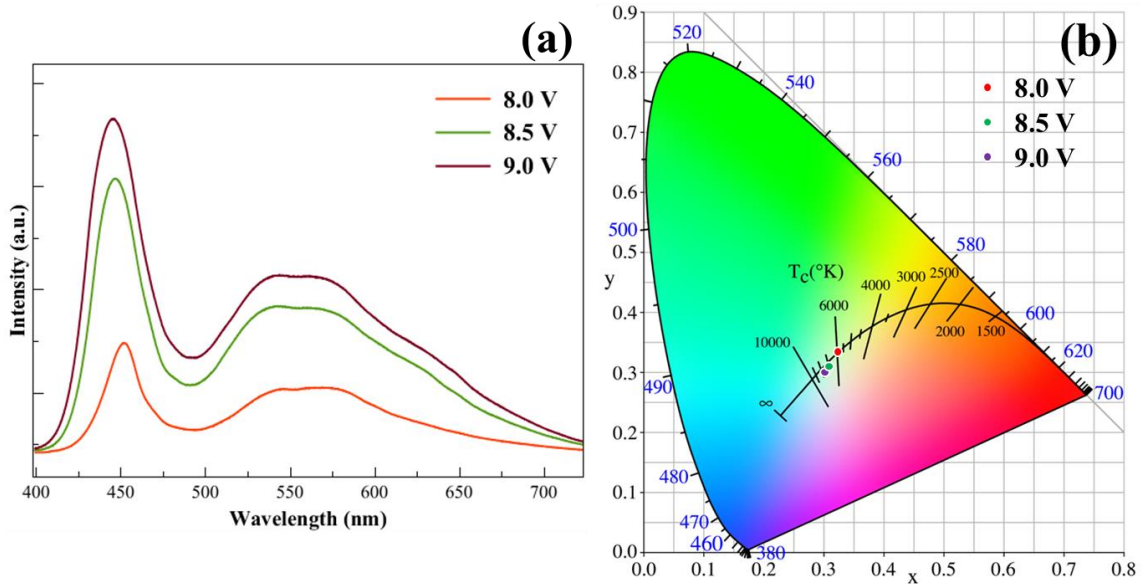


Figure 71. (a) White luminescent spectra of YAG:6%Ce+H₂ powder coated on blue chip with different operating voltages (circle marker in Figure 69). (b) CIE coordinates of WLED at different operating voltages.

6.3. Summary

In this chapter, the probing of NPs on in engineering system is discussed. First, we observe the distribution of inorganic additives in a grease lubricant using synchrotron-based dual-energy μ -XCT for the first time. We find that due to sliding, Fe₃O₄ particles were adhered to the edge of calcium complex thickeners and the grease formed a film. A thinner film thickness due to sliding shows higher density. This is

interesting because based on our results, we could establish a relationship between a shear force and film thickness *in situ*.

Second, we assemble the WLED device by coating YAG:Ce powder mixed with epoxy resin on the blue chips. By using hydrogen treatment, the luminescent color of YAG:Ce is changed, which lead to the color of assembled WLED is altered as well. Meanwhile, with changing the ratio of powder to epoxy resin and the operating voltages, the color in CIE coordinate can be shifted.

CHAPTER VII

CONCLUSIONS AND FUTURE RECOMMENDATIONS

7.1. Conclusions

This research investigated optical performance of rare earth (RE) doped nanoparticles (NPs) and their applications on environment, white LED, and lubricant. Optical and tomographic imaging was used to study the effects of RE-doped NPs on biological and engineering system.

The followings are the highlights of main outcomes and discoveries:

1. A novel approach was developed to control the morphology of erbium and ytterbium co-doped yttrium oxide ($\text{Y}_2\text{O}_3:\text{Er}^{3+}, \text{Yb}^{3+}$) NPs by introducing metal ions during hydrothermal reaction. It was found that the negatively charged aluminum complex ions enabled the evolution of nanotubes through rolling from nanosheets. The positively charged calcium complex ions prohibited the rolling of nanosheets.
2. Hydrogenation was firstly used to treat the cerium doped aluminum yttrium oxide ($\text{YAG}:\text{Ce}^{3+}$). A red-shift was observed in the emission spectrum. Taking advantage of this red-shift in white LED (light-emitting diode) can be potential to make warm luminescence.
3. Oleic acid coated sodium yttrium fluoride ($\text{OA-NaYF}_4:\text{Er}^{3+}, \text{Yb}^{3+}$) NPs were firstly applied in the mineral oil. They would be a potential excellent additives, as they can dispersed well in the nonpolar organic agent. In

addition, synchrotron dual-energy X-ray micro-tomography was used to identify the three components of lubricating grease.

4. Three approaches and mechanisms in modifying optical performance of RE-doped nanoparticles (NPs) were discussed. They are using alternative host lattice, alternative dopants and introducing defects. By using alternative dopants, the optical performance is attributed to the energy level of doped rare earth elements. For alternative host lattice, the optical behavior is decided by the symmetry and ligand distance of doping sites. Hydrogenation and introducing metal ions during reaction were employed to introducing defects. The optical performance was modified due to the host lattice distortion, nephelauxetic effects or gap changing.
5. The effects of RE-doped NPs on environment was investigated. The uptake pathway, accumulation and distribution of NPs in the producer and primary consumer, the plants and insects, were studied using dual-energy X-ray micro-tomography combined with K-edge subtraction method. It was found that NPs size and morphology affected the translocation in biological tissue.

7.2. Future recommendations

The following recommendations are for the future work:

1. Based on our current research, the RE-doped NPs can be accumulated in organisms. The next step is to apply the RE-Doped NPs in a simple food chain to study the bio-magnification.

2. The morphology of noble metals can be modified by introducing DNA during synthesis. This method can be applied to RE-doped NPs, as the optical performance could be modified. In addition, the DNA-mediated RE-doped NPs would be water-solution. With the excellent optical properties, they can be a good tool used in DNA diagnosing and drug delivery.

REFERENCES

- 1 Humphries, M. *Rare earth elements: the global supply chain*. (DIANE Publishing, 2010).
- 2 Zhu, C., Yang, Y., Liang, X., Yuan, S. & Chen, G. *Journal of Luminescence* **126**, 707-710 (2007).
- 3 Zhao, X., He, S. & Tan, M. C. *Journal of Materials Chemistry C* **4**, 8349-8372 (2016).
- 4 Fischer, S., Bronstein, N. D., Swabeck, J. K., Chan, E. M. & Alivisatos, A. P. *Nano Letters* **16**, 7241-7247 (2016).
- 5 Alombert-Goget, G. *et al. SPIE Newsroom* **22** (2011).
- 6 Zhou, J., Teng, Y., Zhou, S. & Qiu, J. *International Journal of Applied Glass Science* **3**, 299-308 (2012).
- 7 Piper, W. W., DeLuca, J. A. & Ham, F. S. *Journal of Luminescence* **8**, 344-348 (1974).
- 8 Sommerdijk, J. L., Bril, A. & de Jager, A. W. *Journal of Luminescence* **8**, 341-343 (1974).
- 9 Van Sark, W. *Thin solid films* **516**, 6808-6812 (2008).
- 10 Michalet, X. *et al. science* **307**, 538-544 (2005).
- 11 Jaiswal, J. K., Goldman, E. R., Mattoussi, H. & Simon, S. M. *Nature methods* **1**, 73-78 (2004).
- 12 Ding, X. & Wang, Y. *Physical Chemistry Chemical Physics* **19**, 2449-2458 (2017).
- 13 Huang, C.-H., Liu, W.-R., Chan, T.-S. & Lai, Y.-T. *Dalton Transactions* **43**, 7917-7923 (2014).
- 14 Richards, B. S. *Solar Energy Materials and Solar Cells* **90**, 1189-1207 (2006).
- 15 Meijer, J.-M., Aarts, L., van der Ende, B. M., Vlugt, T. J. H. & Meijerink, A. *Physical Review B* **81**, 035107 (2010).

- 16 Chen, G. Y., Qju, H. L., Prasad, P. N. & Chen, X. Y. *Chemical Reviews* **114**, 5161-5214 (2014).
- 17 Waynant, R. W. *Lasers in medicine*. (CRC Press, 2013).
- 18 Rombach-Riegraf, V. *et al. Biochem Bioph Res Co* **430**, 260-264 (2013).
- 19 Pust, P. *et al. Nat Mater* **13**, 891-896 (2014).
- 20 Ronda, C. R., Jüstel, T. & Nikol, H. *Journal of Alloys and Compounds* **275**, 669-676 (1998).
- 21 Al-waisawy, S., Jadwisienczak, W. M., Wright, J. T., Pendrill, D. & Rahman, F. *Journal of Luminescence* **169, Part A**, 196-203 (2016).
- 22 Inoue, K., Hirosaki, N., Xie, R.-J. & Takeda, T. *The Journal of Physical Chemistry C* **113**, 9392-9397 (2009).
- 23 Liu, Y., Tu, D., Zhu, H. & Chen, X. *Chemical Society Reviews* **42**, 6924-6958 (2013).
- 24 Wang, F., Banerjee, D., Liu, Y., Chen, X. & Liu, X. *The Analyst* **135**, 1839-1854 (2010).
- 25 Chen, Y. & Liang, H. *Journal of Photochemistry and Photobiology B: Biology* **135**, 23-32 (2014).
- 26 Li, D., Dong, X., Yu, W., Wang, J. & Liu, G. *J Nanopart Res* **15**, 1-10 (2013).
- 27 Ma, C. G. *et al.* Energy level schemes of f^N electronic configurations for the di-, tri-, and tetravalent lanthanides and actinides in a free state. *Journal of Luminescence* **170**, 369-374 (2016).
- 28 Smith, A. M., Mancini, M. C. & Nie, S. M. *Nat Nanotechnol* **4**, 710-711 (2009).
- 29 Liu, Q. *et al. J Am Chem Soc* **133**, 17122-17125 (2011).
- 30 Li, Z. Q., Zhang, Y. & Jiang, S. *Adv Mater* **20**, 4765 (2008).
- 31 Su, L. T. *et al. Adv Mater* **25**, 1603-1607 (2013).
- 32 Yan, C., Dadvand, A., Rosei, F. & Perepichka, D. F. *J Am Chem Soc* **132**, 8868 (2010).
- 33 Bai, G., Tsang, M.-K. & Hao, J. *Advanced Functional Materials* **26**, 6330-6350 (2016).

- 34 Dong, B. *et al.* *RSC Advances* **2**, 3897-3905 (2012).
- 35 Huang, J. *et al.* *CrystEngComm* **17**, 7079-7085 (2015).
- 36 Zhou, B., Tao, L., Tsang, Y. H., Jin, W. & Pun, E. Y.-B. *Optics express* **20**, 3803-3813 (2012).
- 37 Yadav, R. & Rai, S. *Journal of Luminescence* **190**, 171-178 (2017).
- 38 Nunes, L. A. O., Souza, A. S., Carlos, L. D. & Malta, O. L. *Optical Materials* **63**, 42-45 (2017).
- 39 Dousti, M. R. & Amjad, R. J. *NANOP* **10**, 046010-046010 (2016).
- 40 Bedyal, A., Kumar, V., Ntwaeaborwa, O. & Swart, H. *Materials Research Express* **1**, 015006 (2014).
- 41 Yang, F., Liu, Y., Tian, X., Dong, G. & Yu, Q. *Journal of Solid State Chemistry* **225**, 19-23 (2015).
- 42 Kumar, B. V. *et al.* *Journal of Applied Physics* **108**, 044906 (2010).
- 43 Loiko, P. *et al.* *Journal of Luminescence* **179**, 64-73 (2016).
- 44 Terra, I. *et al.* *Journal of Applied Physics* **113**, 073105 (2013).
- 45 Ghosh, P., Kar, A. & Patra, A. *Nanoscale* **2**, 1196-1202 (2010).
- 46 Caldiño, U. *et al.* *Journal of Luminescence* **167**, 327-332 (2015).
- 47 Dodson, C. M., Kurvits, J. A., Li, D., Jiang, M. & Zia, R. *Opt. Mater. Express* **4**, 2441-2450 (2014).
- 48 Dereń, P. J. & Lemański, K. *Journal of Luminescence* **154**, 62-67 (2014).
- 49 Yu, D., Huang, X., Ye, S., Zhang, Q. & Wang, J. *AIP Advances* **1**, 042161 (2011).
- 50 Manzani, D. *et al.* *Opt. Mater. Express* **1**, 1515-1526 (2011).
- 51 Balaji, S., Sontakke, A. D., Sen, R. & Kalyandurg, A. *Opt. Mater. Express* **1**, 138-150 (2011).
- 52 Chai, G., Dong, G., Qiu, J., Zhang, Q. & Yang, Z. **3**, 1598 (2013).
- 53 Zhang, X. *et al.* *CrystEngComm* **14**, 8357-8360 (2012).

- 54 Manzani, D. *et al. Opt. Mater. Express* **1**, 1515-1526 (2011).
- 55 Sreenivasan, V. K., Zvyagin, A. V. & Goldys, E. M. *Journal of Physics: Condensed Matter* **25**, 194101 (2013).
- 56 Huang, H. *et al. RSC Advances* **7**, 16777-16786 (2017).
- 57 Shestakov, M. *et al. Optics express* **19**, 15955-15964 (2011).
- 58 Xia, Z. & Meijerink, A. *Chemical Society Reviews* **46**, 275-299 (2017).
- 59 Shinde, N., Dhoble, N. S., Gedam, S. C. & Dhoble, S. J. *Luminescence* **30**, 898-903 (2015).
- 60 Pan, Z. *et al. NANOP* **6**, 063508-063501-063508-063511 (2012).
- 61 Auzel, F. *Chemical Reviews* **104**, 139-173 (2004).
- 62 Wegh, R. T., Donker, H., Oskam, K. D. & Meijerink, A. *Science* **283**, 663-666 (1999).
- 63 Wegh, R. T., Donker, H., Oskam, K. D. & Meijerink, A. *Journal of Luminescence* **82**, 93-104 (1999).
- 64 Huang, X., Han, S., Huang, W. & Liu, X. *Chem Soc Rev* **42**, 173-201 (2013).
- 65 DaCosta, M. V., Doughan, S., Han, Y. & Krull, U. J. *Analytica Chimica Acta* **832**, 1-33 (2014).
- 66 María, G.-B. & Julia, P.-P. *Methods and Applications in Fluorescence* **3**, 042002 (2015).
- 67 Chan, E. M. *Chemical Society Reviews* **44**, 1653-1679 (2015).
- 68 Mahata, M. K., Hofsäss, H. C. & Vetter, U. in *Luminescence-An Outlook on the Phenomena and their Applications* (InTech, 2016).
- 69 Chivian, J. S., Case, W. & Eden, D. *Applied Physics Letters* **35**, 124-125 (1979).
- 70 Murphy, G. E. & Jensen, G. J. *Biotechniques* **43**, 413-415 (2007).
- 71 Holbrook, R. D., Murphy, K. E., Morrow, J. B. & Cole, K. D. *Nat Nano* **3**, 352-355 (2008).
- 72 Xia, A. *et al. Biomaterials* **32**, 7200-7208 (2011).

- 73 Sun, Y. *et al. Biomaterials* **32**, 2999-3007 (2011).
- 74 Zhang, K. *et al. Sci. Rep.* **5**, 8766 (2015).
- 75 Walton, L. A. *et al. Sci. Rep.* **5**, 10074 (2015).
- 76 Pysz, M. A., Gambhir, S. S. & Willmann, J. K. *Clinical Radiology* **65**, 500-516 (2010).
- 77 Baker, M. *Nature* **463**, 977-980 (2010).
- 78 Thorp-Greenwood, F. L. & Coogan, M. P. *Dalton Transactions* **40**, 6129-6143 (2011).
- 79 Chen, H. *et al. Biosensors and Bioelectronics* **48**, 19-25 (2013).
- 80 Kherlopian, A. R. *et al. BMC Syst Biol* **2**, 74 (2008).
- 81 Cnudde, V. & Boone, M. N. *Earth-Science Reviews* **123**, 1-17 (2013).
- 82 Midgley, S. & Schleich, N. *Journal of Synchrotron Radiation* **22**, 807-818 (2015).
- 83 He, M. *et al. Advanced Functional Materials* **21**, 4470-4477 (2011).
- 84 Ferrucci, M., Leach, R. K., Giusca, C., Carmignato, S. & Dewulf, W. *Measurement Science and Technology* **26**, 092003 (2015).
- 85 Chen, Y. *et al. Journal of Nanobiotechnology* **14**, 1 (2016).
- 86 Zhu, Y. *et al. Nanomedicine : nanotechnology, biology, and medicine* **10**, 515-524 (2014).
- 87 Cnudde, V. & Boone, M. N. *Earth-Science Reviews* **123**, 1-17 (2013).
- 88 Khan, A. G., Kuek, C., Chaudhry, T. M., Khoo, C. S. & Hayes, W. J. *Chemosphere* **41**, 197-207 (2000).
- 89 Nordmann, J., Buczka, S., Voss, B., Haase, M. & Mummenhoff, K. *J Mater Chem B* **3**, 144-150 (2015).
- 90 Smith, T. & Guild, J. *Transactions of the optical society* **33**, 73 (1931).
- 91 Shen, L., Liu, X., Chen, B., Pun, E. Y. B. & Lin, H. *Journal of Physics D: Applied Physics* **45**, 115301 (2012).

- 92 Wang, S.-F. *et al. Scientific reports* **5**, 12849 (2015).
- 93 Ashdown, I. E. in *Proc. SPIE*. **4776** 51-60 (2002).
- 94 Sanchez, C., Chen, Y., Parkinson, D. Y. & Liang, H. *Tribology International* **111**, 66-72 (2017).
- 95 Stoltenberg, R. M. & Woolley, A. T. *Biomedical Microdevices* **6**, 105-111 (2004).
- 96 Dai, W., Kheireddin, B., Gao, H. & Liang, H. *Tribology International* **102**, 88-98 (2016).
- 97 Roman, C., Valencia, C. & Franco, J. *Tribology Letters* **63**, 1-12 (2016).
- 98 Chen, Y., Choi, H. & Liang, H. *Journal of Nanoscience and Nanotechnology* **17**, 1870-1876 (2017).
- 99 Yang, H. & Kim, Y.-S. *Journal of Luminescence* **128**, 1570-1576 (2008).
- 100 Chen, G., Qiu, H., Prasad, P. N. & Chen, X. *Chemical Reviews* **114**, 5161-5214 (2014).
- 101 Kundu, S., Wang, K. & Liang, H. *The Journal of Physical Chemistry C* **113**, 18570 (2009).
- 102 He, X., Zhou, Y. & Liang, H. *Journal of Materials Chemistry C* **1**, 6829 (2013).
- 103 Chiu, C.-W., González, J. M., Harlow, M., Vinson, S. B. & liang, H. *Electrochimica Acta* **68**, 81 (2012).
- 104 Ling, D., Hackett, M. J. & Hyeon, T. *Nano Today* **9**, 457-477 (2014).
- 105 Kundu, S. & Nithiyantham, U. *Rsc Advances* **3**, 25278 (2013).
- 106 Kundu, S., Mukadam, M. D., Yusuf, S. M. & Jayachandran, M. *Crystengcomm* **15**, 482 (2013).
- 107 Li, N. & Yanagisawa, K. *Journal of Solid State Chemistry* **181**, 1738 (2008).
- 108 Sahraneshin, A. *et al. CrystEngComm* **14**, 6085 (2012).
- 109 Qi, K. *et al. CrystEngComm* **15**, 6729 (2013).
- 110 Li, N., Yanagisawa, K. & Kumada, N. *Cryst Growth Des* **9**, 978 (2009).

- 111 Zong, L. *et al.* *J Nanopart Res* **16**, 1 (2014).
- 112 Andelman, T., Gordonov, S., Busto, G., Moghe, P. V. & Riman, R. E. *Nanoscale research letters* **5**, 263 (2010).
- 113 Das, G. K. & Tan, T. T. Y. *J Phys Chem C* **112**, 11211 (2008).
- 114 Wang, L. *et al.* *Mater Res Bull* **61**, 89 (2015).
- 115 Srinivasan, R., Yogamalar, N. R., Elanchezhiyan, J., Joseyphus, R. J. & Bose, A. C. *Journal of Alloys and Compounds* **496**, 472-477 (2010).
- 116 Li, R. B. *et al.* *Acs Nano* **8**, 1771-1783 (2014).
- 117 Wu, G. *et al.* *J Am Chem Soc* **135**, 18276-18279 (2013).
- 118 Towata, A. *et al.* *J Mater Sci* **43**, 1214 (2008).
- 119 Chen, Z. *et al.* *J Am Chem Soc* **130**, 3023-3029 (2008).
- 120 Zhao, Q. *et al.* *CrystEngComm* **15**, 4844 (2013).
- 121 Zheng, Y. *et al.* *CrystEngComm* **12**, 585 (2010).
- 122 Tanner, P. A. & Fu, L. *Chemical Physics Letters* **470**, 75 (2009).
- 123 Wu, X., Tao, Y., Gao, F., Dong, L. & Hu, Z. *Journal of Crystal Growth* **277**, 643 (2005).
- 124 Joo, J., Chow, B. Y., Prakash, M., Boyden, E. S. & Jacobson, J. M. *Nature materials* **10**, 596 (2011).
- 125 Zhu, S. *et al.* *Ceramics International* **39**, 9637 (2013).
- 126 Brown, R. *et al.* *J Mater Sci* **48**, 4908 (2013).
- 127 Dar, M. I., Arora, N., Singh, N. P., Sampath, S. & Shivashankar, S. A. *New J Chem* **38**, 4783 (2014).
- 128 Mewis, J. & J. Wagner, N. *J. Non-Newtonian Fluid Mech.* **157**, 147-150 (2009).
- 129 Aveyard, R. R., Brinks, B. P. & Clint, J. H. *Adv. Colloid Interface Sci.* **100**, 503-546 (2003).
- 130 Ladd, A. J. C. *J. Fluid Mech.* **271**, 311-319 (1994).

- 131 Martys, N. S. *J. Rheol.* **49**, 401-424 (2005).
- 132 Pozrikidis, C. *Eur. J. Mech. B/Fluids* **24**, 125-136 (2005).
- 133 Shapley, N. C., Armstrong, R. C. & Brown, R. A. *J. Rheol.* **48**, 255-279 (2004).
- 134 Wierenga, A., Philipse, A. P. & Lekkerkerker, H. N. W. *Langmuir* **14**, 55-65 (1998).
- 135 Fadlalla, H. *et al. Mater Res Bull* **43**, 3457-3462 (2008).
- 136 Bachmann, V., Ronda, C. & Meijerink, A. *Chemistry of Materials* **21**, 2077-2084 (2009).
- 137 Palmero, P. *et al. Mater Res Bull* **48**, 2589-2597 (2013).
- 138 Ivaturi, A. *et al. Journal of applied physics* **114**, 013505 (2013).
- 139 Chatterjee, D. K., Rufaihah, A. J. & Zhang, Y. *Biomaterials* **29**, 937-943 (2008).
- 140 Achatz, D. E., Meier, R. J., Fischer, L. H. & Wolfbeis, O. S. *Angewandte Chemie International Edition* **50**, 260-263 (2011).
- 141 Kang, X. *et al. The Journal of Physical Chemistry C* **115**, 15801-15811 (2011).
- 142 Zhang, X. *et al. Advanced Functional Materials* **23**, 4067-4078 (2013).
- 143 Shan, S.-N., Wang, X.-Y. & Jia, N.-Q. *Nanoscale Research Letters* **6**, 539-539 (2011).
- 144 Feng, W., Sun, L. D., Zhang, Y. W. & Yan, C. H. *Small* **5**, 2057-2060 (2009).
- 145 Gong, M., Xiang, W., Huang, J., Yin, C. & Liang, X. *RSC Advances* **5**, 75781-75786 (2015).
- 146 Fang, Z. *et al. Journal of Materials Chemistry C* **2**, 2204-2211 (2014).
- 147 Ueda, J., Dorenbos, P., Bos, A. J., Meijerink, A. & Tanabe, S. *The Journal of Physical Chemistry C* **119**, 25003-25008 (2015).
- 148 Mhin, S. *et al. Nanoscale research letters* **4**, 888 (2009).
- 149 Guan, R., Cao, L., You, Y. & Cao, Y. *Journal of Nanomaterials* **2015**, 3 (2015).
- 150 Liu, G. & Jacquier, B. *Spectroscopic properties of rare earths in optical materials*. Vol. 83 Ch. 1, 1-94 (Springer, 2006).

- 151 Song, Y. *et al.* *RSC Advances* **2**, 4777-4781 (2012).
- 152 Kobayashi, H., Fujii, K., Nunokawa, T., Odawara, O. & Wada, H. *Japanese Journal of Applied Physics* **53**, 05FK04 (2014).
- 153 Dammak, M., Maalej, R., Kamoun, M. & Deschanvres, J. L. *physica status solidi (b)* **239**, 193-202 (2003).
- 154 Chandra, S., Deepak, F. L., Gruber, J. B. & Sardar, D. K. *The Journal of Physical Chemistry C* **114**, 874-880 (2009).
- 155 Newman, D. J. & Ng, B. *Crystal field handbook*. (Cambridge University Press, 2007).
- 156 Liu, G. *Chemical Society Reviews* **44**, 1635-1652 (2015).
- 157 Rai, P. *et al.* *Ceramics International* **38**, 235-242 (2012).
- 158 Fadlalla, H. M. H. & Tang, C. *Journal of Crystal Growth* **311**, 3737-3741 (2009).
- 159 Chen, X., Liu, L., Yu, P. Y. & Mao, S. S. *Science* **331**, 746-750 (2011).
- 160 Yang, L. *et al.* *Journal of Physics D: Applied Physics* **49**, 325303 (2016).
- 161 Blasse, G. & Grabmaier, B. *Luminescent materials*. (Springer Science & Business Media, 2012).
- 162 Li, G., Tian, Y., Zhao, Y. & Lin, J. *Chemical Society Reviews* **44**, 8688-8713 (2015).
- 163 Wang, J., Han, T., Lang, T., Tu, M. & Peng, L. *Optical Engineering* **54**, 117106-117106 (2015).
- 164 Rack, P. D. & Holloway, P. H. *Materials Science and Engineering: R: Reports* **21**, 171-219 (1998).
- 165 Tahira Gul, H., Saeed, S., Zafar, F., Khan, A. & Manzoor, S. *Potential of Nanotechnology in Agriculture and Crop Protection: A Review*. Vol. 1 (2014).
- 166 Mukhopadhyay, S. S. *Nanotechnology, science and applications* **7**, 63 (2014).
- 167 Chen, Y., C. Sanchez, Y. Yue, J.M. González, D.Y. Parkinson & H. Liang. *Journal of Synchrotron Radiation* **23**, 1197-1201 (2016).
- 168 Chen, Y. *et al.* *J Nanobiotechnology* **14**, 23 (2016).

- 169 Diez, L., Urbain, L., Lejeune, P. & Detrain, C. *Behavioural processes* **116**, 80-86 (2015).
- 170 Rocha, A. *et al.* *J Nanobiotechnology* **9**, 5 (2011).
- 171 Panagiotakopulu, E. *Journal of Archaeological Science* **28**, 1235-1246 (2001).
- 172 Ramos-Elorduy, J., Gonzalez, E. A., Hernandez, A. R. & Pino, J. M. *J Econ Entomol* **95**, 214-220 (2002).
- 173 Finke, M. & Winn, D. *J Wildlife Rehabil* **27**, 14-27 (2004).
- 174 Snodgrass, R. E. *Principles of insect morphology*. 1-667 (New York, McGraw-Hill, 1935., 1935).
- 175 Rocha, A. *et al.* *J Nanobiotechnol* **9**, doi:10.1186/1477-3155-1189-1185 (2011).
- 176 Wolverton, B. C., Mcdonald, R. C. & Watkins, E. A. *Econ Bot* **38**, 224-228 (1984).
- 177 Ma, X. M., Geiser-Lee, J., Deng, Y. & Kolmakov, A. *Sci Total Environ* **408**, 3053-3061 (2010).
- 178 Navarro, D. A., Bisson, M. A. & Aga, D. S. *J Hazard Mater* **211**, 427-435 (2012).
- 179 Lv, J. T. *et al.* *Environ-Sci Nano* **2**, 68-77 (2015).
- 180 Hawthorne, J. *et al.* *Environ Sci Technol* **48**, 13102-13109 (2014).
- 181 Zhu, H., Han, J., Xiao, J. Q. & Jin, Y. *J Environ Monitor* **10**, 713-717 (2008).
- 182 Lin, S. J. *et al.* *Small* **5**, 1128-1132 (2009).
- 183 Zhu, Z. J. *et al.* *Environ Sci Technol* **46**, 12391-12398 (2012).
- 184 Quah, B., Musante, C., White, J. C. & Ma, X. *J Nanopart Res* **17**, 1-13 (2015).
- 185 Siddiqui, M. H., Al-Whaibi, M. H., Firoz, M. & Al-Khaishany, M. Y. in *Nanotechnology and Plant Sciences* 19-35 (Springer, 2015).
- 186 Qi, M., Liu, Y. & Li, T. *Biological trace element research* **156**, 323-328 (2013).
- 187 Zhang, D. Q. *et al.* *Ecol Eng* **70**, 114-123 (2014).

- 188 Palomo-Siguero, M., Lopez-Heras, M. I., Camara, C. & Madrid, Y. *J Anal Atom Spectrom* **30**, 1237-1244 (2015).
- 189 Wang, J. *et al. Environ Sci Technol* **48**, 6754-6762 (2014).
- 190 Lombi, E., Scheckel, K. G. & Kempson, I. M. *Environ Exp Bot* **72**, 3-17 (2011).
- 191 Tappero, R. *et al. New Phytol* **175**, 641-654 (2007).
- 192 Zhu, Y. *et al. Nanomed-Nanotechnol* **10**, 515-524 (2014).
- 193 Zach, A. *et al. Flora* **205**, 506-512 (2010).
- 194 Dilmanian, F. A. *et al. Phys Med Biol* **42**, 371-387 (1997).
- 195 Cooper, D. M. L. *et al. Phys Med Biol* **57**, 5777-5786 (2012).
- 196 Kruger, R. A. *et al. Radiology* **125**, 243-245 (1977).
- 197 White, P. J. & Greenwood, D. J. *Soil Conditions and Plant Growth*, 160-194 (2013).
- 198 White, P. J. & Broadley, M. R. *New Phytol* **182**, 49-84 (2009).
- 199 Birbaum, K. *et al. Environ Sci Technol* **44**, 8718-8723 (2010).
- 200 Rico, C. M., Majumdar, S., Duarte-Gardea, M., Peralta-Videa, J. R. & Gardea-Torresdey, J. L. *J Agr Food Chem* **59**, 3485-3498 (2011).
- 201 Corredor, E. *et al. BMC Plant Biology* **9**, 1-11 (2009).
- 202 Majumdar, S. *et al. J Hazard Mater* **278**, 279-287 (2014).
- 203 Shen, C.-X., Zhang, Q.-F., Li, J., Bi, F.-C. & Yao, N. *American Journal of Botany* **97**, 1602-1609 (2010).
- 204 Takaya, M. *et al. Industrial health* **44**, 639-644 (2006).
- 205 Donahue, C. J. *Journal of Chemical Education* **83**, 862 (2006).
- 206 Mohan, N., Sharma, M. & Singh, R. in *International Conference of Advance Research and Innovation*. 400-404.
- 207 Sharma, A. K., Tiwari, A. K. & Dixit, A. R. *Materials and Manufacturing Processes* **30**, 813-828 (2015).

- 208 Spear, J. C., Ewers, B. W. & Batteas, J. D. *Nano Today* **10**, 301-314 (2015).
- 209 Schnabel, S., Marklund, P. & Larsson, R. *Proceedings of the Institution of Mechanical Engineers, Part J: Journal of Engineering Tribology* **228**, 1063-1070 (2014).
- 210 Jiusheng, B., Zhencai, Z., Yan, Y. & Shujin, L. *Industrial Lubrication and Tribology* **61**, 228-231 (2009).
- 211 Zhou, G. *et al. Wear* **301**, 753-757 (2013).
- 212 Kratochvil, T. *et al. J Anal Atom Spectrom* **29**, 1806-1812 (2014).
- 213 Petrucci, F. & Senofonte, O. *Analytical Methods* **7**, 5269-5274 (2015).
- 214 Manohar, N., Reynoso, F. J., Diagaradjane, P., Krishnan, S. & Cho, S. H. *Scientific Reports* **6**, 22079 (2016).
- 215 Yuan, L., Lin, W., Zheng, K. & Zhu, S. *Accounts of Chemical Research* **46**, 1462-1473 (2013).
- 216 Wang, Y., Hu, R., Lin, G., Roy, I. & Yong, K.-T. *ACS Applied Materials & Interfaces* **5**, 2786-2799 (2013).
- 217 Wegner, K. D. *et al. ACS Applied Materials & Interfaces* **5**, 2881-2892 (2013).
- 218 Xie, R.-J., Hirosaki, N., Sakuma, K., Yamamoto, Y. & Mitomo, M. *Applied physics letters* **84**, 5404-5406 (2004).
- 219 Hirosaki, N. *et al. Applied Physics Letters* **86**, 211905 (2005).
- 220 Zhu, H. *et al. Nature communications* **5**, 4312 (2014).
- 221 Cushing, S. K. *et al. ACS Catalysis* **7**, 1742-1748 (2017).
- 222 Vázquez - Galván, J. *et al. ChemSusChem* **10**, 2089-2098 (2017).
- 223 Wang, G. *et al. Nano letters* **11**, 3026-3033 (2011).